3D non-linear finite element modelling of an onshore wind turbine foundation

J.R. Moraal

Technische Universiteit Delft

TU Delft

3D non-linear finite element modelling of an onshore wind turbine foundation

by

J.R. Moraal

to obtain the degree of Master of Science
at the Delft University of Technology,
to be defended publicly on Thursday Februari 28, 2019 at 15:30.

Student number:	4006267	
Project duration:	April 1, 2018 – Februari 28, 2019	
Thesis committee:	Prof. dr. ir. J. G. Rots,	TU Delft, chair
	Dr. ir. M. A. N. Hendriks,	TU Delft
	Dr. ir. W. Broere,	TU Delft
	Ir. F. de Haas,	Royal HaskoningDHV, supervisor

An electronic version of this thesis is available at `http://repository.tudelft.nl/`.

TU Delft

Royal HaskoningDHV
Enhancing Society Together

Abstract

Currently wind turbines are a popular source of renewable energy. Royal HaskoningDHV designs foundations for these turbines. Design optimization of these foundations becomes more and more important due to the growing demand for renewable energy, the development of increasingly large wind turbines and intensification of competition. Design improvements can reduce construction costs, and also reduce the carbon footprint of the tower foundation.

Today these foundations are designed using the Eurocode in combination with the results from linear analysis of a 2D model. Expectations are that this yields a conservative model. A 3D non-linear model is expected to provide a more detailed insight into the actual structural behaviour of such a foundation. Specifically, the distribution of concrete and reinforcement stresses and strains can be found, and used to determine whether, and where, reinforcement can be reduced or should be increased.

To obtain a non-linear 3D model, first a linear 3D model is developed, starting from the existing 2D model. Subsequently the results of the two linear models are compared. Once the linear 3D model is deemed to function satisfactorily, it is further developed to incorporate non-linear material properties and reinforcement, taking into account observations made in the linear analysis.

Simplifications made for the 2D model cease to hold. Besides minor details, the pedestal, that was left out of the scope for the 2D model, is introduced in the 3D model. Additionally, the connection between the foundation piles and the structure are placed at the underside, instead of at mid-height. Results of the 2D and 3D linear models are generally similar. However, small differences were observed. In general, these differences can be attributed to these two main modelling differences. Modelling in 3D opened up more possibilities for detailing of the supporting foundation piles. However the effects on the results for different support cases was minor.

After comparing the linear analysis results, the next step is a non-linear model. The non-linear 3D model includes several non-linear aspects. Reinforcement was incorporated. Non-linear constitutive models were studied and chosen for concrete in tension and compression as well as for the reinforcement steel. Connections between different parts of the structure, such as the anchor cage, were also modelled non-linearly.

The results of the non-linear analysis seems to provide an improved insight into the structural behaviour of the foundation structure. More detailed information about concrete strains, reinforcement stresses, crack progression and displacements can be shown, and used to verify, or disprove, assumptions based on the 2D linear analysis. However, problems with non-convergence occur before the expected failure load without a satisfactory structural explanation. Therefore the model does not provide a plausible structural failure load. Because no ultimate load was found it is difficult to determine whether, and if so, how much the applied reinforcement can be reduced. Nevertheless, the model could be used in a more qualitative way to show and describe where stress concentrations will occur and how the structure will deform.

Internal splitting cracks are seen outside of the centre of the structure where only limited reinforcement is present. These splitting cracks may be a cause of model instability. Design alterations can be made to increase the load for which non-convergence occurs. An increased the ultimate load is found when splitting reinforcement is elongated, or when the amount of applied prestressing load on the anchor cage is altered. Even applying a simply modified constitutive concrete model, to represent steel fibre reinforcement, appears beneficial. However, these alterations may only improved the behaviour of the model, while still no actual failure mode is found. It cannot be said without a doubt that these modifications will improve the structural behaviour of the actual structure.

Further research may lead to a solution for the model instability and consequently enabling its use to optimize the reinforcement design.

Acknowledgements

Firstly, I would like to thank my assessment committee members: Jan Rots, Max Hendriks and Wout Broere for their valuable feedback and input.

Furthermore, I want to express my gratitude to my supervisor: Felix de Haas and all the other people at Royal HaskoningDHV for the expert information they provided and their helpful suggestions.

And last but not least, I would like to thank my family and friends for their continuous support. Especially: Martin, Sonja, Josefien and Martijn for generously acting as my sounding board.

Contents

1 Introduction

1.1. Background

Although awareness about global warming and depletion of resources is increasing in our society, governments are still finding it difficult to meet goals set in the Copenhagen accord or, more recent, the Paris Agreement, and a turnaround in general. Global warming is, to a great extent, caused by the emission of greenhouse gases which are a by-product of classical energy production processes that involve fossil fuels. To reduce these emissions, but still satisfy the ever increasing energy demand, renewable energy sources are an absolute necessity.

Amongst others, onshore wind farms with increasingly large turbines are a very suitable source of renewable energy. Wind energy, because of its clean, safe and sustainable nature, is now playing an important role as a source of power. However the production of the construction materials, primarily steel and concrete, still has a considerable carbon footprint. Additionally a lot of wind turbines are required to answer the current and expected energy demand.

There are many aspects of a wind turbine that can be developed and improved upon to achieve a higher energy output, but in general they become larger. This is of course the most interesting from a structural engineering point of view because as the size of the turbine and tower increase, the forces exacted on the structure do so as well, which leads to higher forces and moments in the concrete foundation structure.

Currently Royal HaskoningDHV(RHDHV) designs these foundation structures satisfactory using a 2D finite element model combined with classical reinforcement design methods. But due to the rising demand, growing competition, and the increasing foundation size the importance of structural optimization of such structures becomes more and more meaningful.

To potentially optimize material use and decrease costs, a better understanding concerning the transfer of forces to, and the stress distribution within the structure is required. Because elements like reinforcement and the transfer of forces from the tower to the foundation can be incorporated into a three-dimensional model more readily, such a model might be used to acquire the required understanding to improve the foundation design.

Once a better understanding of transfer of forces in three dimensions has been reached, this can, for instance, in turn be used to study the influence of replacing conventionally reinforced concrete by steel fibre reinforced concrete.

1.2. Objective and scope

The objective of this thesis is to develop a 3D finite element model to be able to study the effects of loading on the structure and determine the possibilities for design optimization to reduce the use of construction materials. To achieve this, firstly a linear 3D model will have to be developed in which all design model options are considered. Subsequently this model will have to be validated by comparison to the linear 2D finite element model that is currently in use. After this reinforcement and non-linear material properties will be incorporated in the model. The results, from the non-linear analyses performed using this model, will be interpreted. Lastly potential design alterations like reduction of the reinforcement used or even the outer dimensions of the foundation can be studied as well as SFRC as a partial alternative to rebar reinforced concrete.

1.3. Thesis outline

In chapter 2 the research context and the design process currently applied by RHDHV are treated. Subsequently in chapter 3 the research questions are posed. chapter 4 describes a general wind turbine design and introduces the reference project. After this in chapter 5 the model choices for the linear analysis and resultant model design are considered. Additionally the new model is compared to the old one. chapter 6 is dedicated to the results of the linear analyses and the comparison of the old and new models. chapter 7 focusses on the model choices that are connected to the non-linear analyses as well as the general reinforcement design and its translation to a finite element mode. The results of the non-linear analyses are treated in chapter 8. In chapter 9 some remarks are made about the reinforcement optimization possibilities. The thesis is concluded by chapter 10 with conclusions, and recommendations.

2

Research context

To transfer the loads from the turbine, via the tower, to the ground a foundation construction has to be used. There are several different types of foundations that are used for wind turbines. The type of foundation used depends on the geotechnical conditions on site. The foundation provides stability to the tower. This is translated to a stiffness requirement, and the design needs to satisfy both structural strength requirements as well as adequate fatigue behaviour. The normal operating and extreme load conditions that are exerted by the turbine are taken into account for the design of the turbine foundation. The most straightforward foundation design is the spread footing design which is essentially a gravity foundation that relies upon soil overburden and concrete to provide sufficient weight to resist overturning of the foundation at extreme wind loads. This type of design is applicable in a broad range of sub-grade strengths from soils to rock. RHDHV has designed foundations of this type for wind turbines in Finland. Pile foundations are often found in regions where competent soil or rock is found at much greater depths. Piles in combination with a concrete foundation structure transmit loads from the turbine to the sub-grade via a combination of friction and end bearing and resist lateral loads through lateral earth pressure on the pile. For this type of foundation the dimensions of the concrete foundation structure are usually based on the foundation pile layout required for resisting the overturning moment produced by the turbine. Such a structure is typically of a circular shape to account for the variable directional nature of the design loadings. Increasingly the trend is towards larger more efficient turbines with individual capacities of 3 MW and greater and hub heights exceeding 100 m now being the norm. This trend leads to a demand of foundation structures of increasing size.

2.1. Current design process

As RHDHV has already provided foundation designs for multiple projects there already is a design process. The design process is split up into two stages: the preliminary stage and the final stage.

2.1.1. Preliminary design stage

Logically the design of the foundation structure is dependent on the turbine. For every turbine the manufacturer formulates the vertical, horizontal and bending moment loads to be resisted. The extreme and operational loads are provided, as well as a fatigue load. Additionally other loads like the dead weight of the concrete, the soil load on top of the structure, and the force exacted by ground water pressure are determined.

Based on these loads a preliminary structural design for the construction is made. The pile forces are determined with a linear analysis. These pile forces are subsequently used as input for the geotechnical analysis carried out according to Eurocode NEN-EN 1997-1: 2004, which is used to define the foundation pile dimensions and consequently the applicable pile stiffness.

2.1.2. Final design stage

The foundation pile data is then in turn used to do a linear analysis with a 2D FEM model with the software package Diana. The distributed moments and shear forces caused by the different load cases (combinations) are checked using this model. Thereupon the calculated moments and forces are used to find an indication of the amount of reinforcement required according to Eurocode NEN-EN 1992-1.

The operational loads that are determined in the preliminary design stage are used for calculation of the rotation stiffness, which in turn is used to check the foundation pile design. The governing amount of required reinforcement in the foundation pile may be on either the pile in tension or in compression. In the final design stage the software package MNKappa is used to make calculations to find the stiffness ratios between piles in tension and compression. Subsequently the moment distribution over each of these piles is determined. These calculations are used to produce the Geotechnical report. Structural calculations are done to check the foundation structure design, and these are reported in the structural report. Besides structural calculation, the formwork- and reinforcement drawings are made in the final design stage as well.

The design workflow chart in Figure 2.1 illustrates this process in detail.

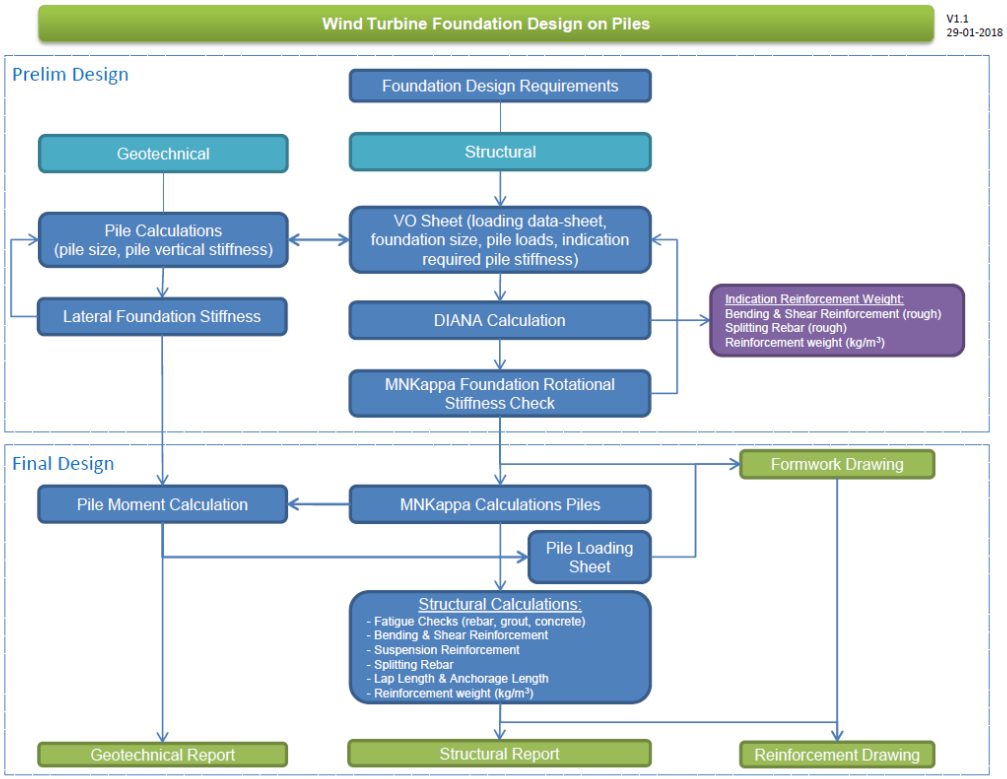

Figure 2.1: Current workflow for the foundation design process

2.2. Model output

The 2D model yields distributed moments and shear forces as output. An example of distributed moments is shown in Figure 2.2a. Figure 2.2b shows how the shear forces may be distributed. In chapter 6 the meaning of such results will be explained.

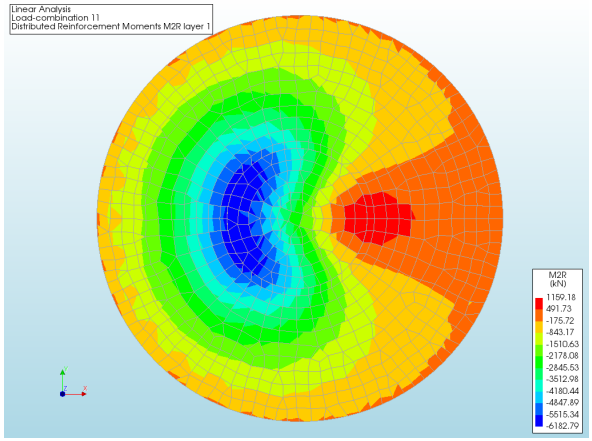

(a) Top view 2D model moments output

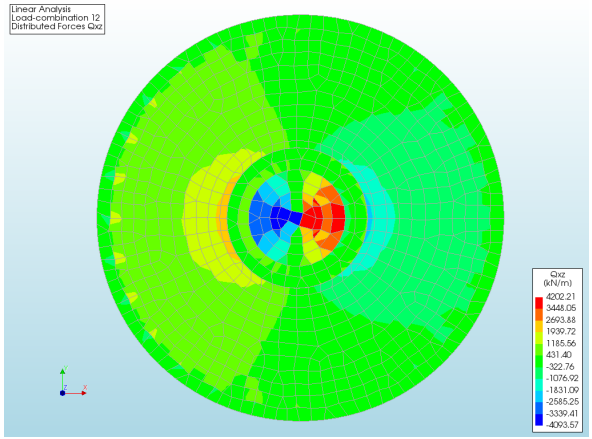

(b) Top view 2D model shear forces output

Figure 2.2: Examples of output from an analysis using the 2D model

For a 3D model the primary output will be stresses, which in combination with inserting the reinforcement in the model, will make it much clearer what the influence of the reinforcement is and where design improvements can be made.

2.3. Reference project

To verify the results of the 3D model, and determine the obtained improvements a reference project has been chosen. In addition, the reference project is important because the goal is to make a model that can be parametrized, so it is pragmatic to directly use correct links to the design dimensions and loading. It would even be superfluous to generate new imaginary data for this project. The reference project used is a foundation design made for BAM Infra:

> BAM Infra has been awarded the task by NUON Windpark Wieringermeer B.V. to build 50 wind turbine foundations in the north eastern part of the province Noord-Holland in the Netherlands in the area Wieringermeer. This report contains the structural design for the wind turbine foundations for a Nordex N117/3600 TS120 IEC2A wind turbine. This report describes the structural analysis for a piled circular tapered foundation, with a diameter of 16.7m for a wind turbine with a hub height of 120m. The thickness of the foundation is 2.385m in the centre and 1.385 m on the outside edge.

This is one of the most recently completed wind turbine foundation projects engineered by RHDHV. For this project the complete analysis was done using the 2D plate element model. Initially it is to be expected that the results from calculations done with a 3D model will be similar, although it is to be expected that several assumptions made during development of the 2D model are conservative leading to slightly higher shear forces and moments in de 2D model.

2.4. Steel fibre reinforced concrete

Steel fibre reinforced concrete (SFRC) is a type of concrete in which steel fibres are mixed in to take up the tensile stresses. This yields different material properties. Both the peak load and the ductility can be increased using the right amount and type of fibres[10]. Tensile strength can be increased using larger fibre volumes and small fibre volumes can already increase the deformation capacity in uni-axial tension. And although the addition of fibres hardly influences the compressive strength, overall the flexural load-bearing capacity can be increased using the right amount of fibres with well tuned characteristics. Additionally the incorporation of steel fibres can enhance the energy absorption capacity and the strain capacity[6]. This leads to increased stiffness and improved dynamic behaviour.

Although in ordinary cases the processing of SFRC is more complex than that of ordinary concrete, one key advantage of the use of SFRC is that it can be easier to apply in the case of a wind turbine foundation, as it reduces the amount of complex steel reinforcement sections to be installed. A possible cause for reduced quality of concrete in wind turbine foundations is the fact that concrete is hard to apply in between the reinforcement bars because of the high concentration of reinforcement, especially in the centre. The use of hybrid reinforcement will decrease the amount of main (bar) reinforcement required, thus possibly improving the quality of the finished product. If the use of SFRC increases the deformation resistance of the structure, it can even be possible to reduce the required height of the foundation.

2.5. Finite element software

The finite element software that will be used for this research will be DIANA FEA. DIANA is suitable for linear, non-linear and modified elasticity calculations. It also has built in fibre reinforced material models and ready built possibilities with reinforcement bars. Additionally there is a good coupling with a python based parametrizable script which is very usable for setting up a model that can be used to optimize designs and which can be reused for multiple different cases.

3

Research

3.1. Problem definition

As the trend of building turbines of increasing size continues, the potential gains that are obtainable due to more detailed knowledge of the exact structural behaviour of the foundation structure increase as well. Therefore enhanced analysis capabilities are sure to be beneficial for optimization of construction material use and thus reduction of carbon footprint and lowered costs. Currently a 2D FEM plate model is used to find the foundation pile forces and the distributed moments used for the calculation of the necessary reinforcement. However because information about stresses is only available in specific points and complex reinforcement designs can not be incorporated in a plate model verification of the reinforcement design, and consequently potential optimization, is difficult. Another important limitation of a 2D model without reinforcement is the fact that the non-linear behaviour associated with reinforced concrete, such as cracking and redistribution of forces, can't be determined. Even when only checking the design linearly the 2D model has its shortcomings. In this 2D model assumptions are made about the distribution of forces over the height of the construction while this is in fact unknown. These assumptions are presumed to be conservative, but this needs verification. Additionally the effects of aspects of the foundation design like prestressing the anchor cage and the inclusion of the anchor- cage or ring itself may be favourable for the stiffness of the foundation but they are now still unknown. Additionally the 2D model is largely unable to find previously unexpected failure modes, while it makes sense that not every possible way of failing is predicted based on engineering experience, even though extensive knowledge is present at RHDHV.

3.2. Goal

The goal of this research project is to develop a 3D model of a wind turbine foundation that includes non-linearity to calculate stresses and strains in order to check and optimize the applied reinforcement design.

As RHDHV already has a 2D linear model in use this will be the starting point. This is schematically shown in Figure 3.1.

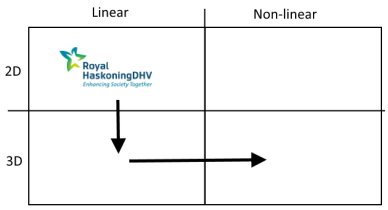

Figure 3.1: Schematization of the overall process towards the goal

3.3. Research questions

For this research two separate, albeit connected, research questions can be posed:

- What considerations influence the development of a non-linear 3D model, improving on an existing linear 2D model, and what are their implications?

- Is it possible to obtain a better understanding of the distribution of stresses and strains in a wind turbine foundation using a 3D non-linear model compared to a linear 2D one, and does this lead to more detailed insight into the possible failure modes?

These questions translate the goal of this project into a more general summarization to be answered in the final chapter of this report.

3.4. Method

To reach te goal of this research and answer the research questions, the model has to be developed. For the model a Python based script is written to generate a model in Diana. As described first a 3D linear model will be set up and compared to the existing 2D linear model for validation, after which the 3D linear model will be refined into a model suited for non-linear analysis by incorporating the reinforcement and introducing non-linear material properties. The development of the models is an iterative process in which faults that show up in the analysis results will be solved in the model. For the non-linear model this also means that erroneous behaviour or failure modes that are out of scope will be fixed. To improve understanding and save time theoretical principles, like material models, and practical model considerations, like interfaces, were tested on a smaller, simpler, beam model. This process has been schematized in Figure 3.2.

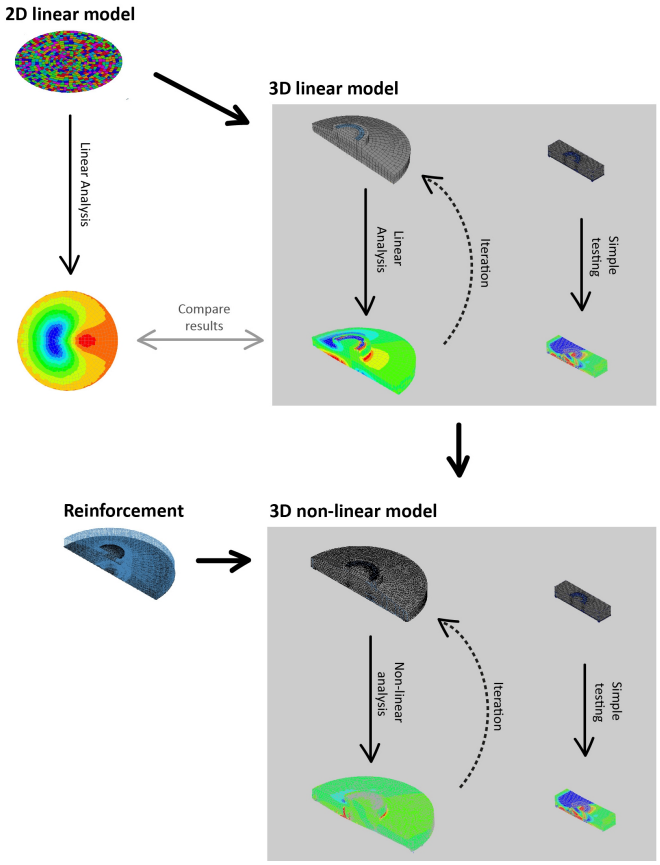

Figure 3.2: Schematization of the applied method.

3.5. Modelling parameters to be determined

To be able to satisfactorily model the turbine foundation to answer the research questions some more detailed aspects of the model need to be determined.

3.5.1. Model properties

Different aspects of the model need to be accounted for. Such as the material models used to include non-linearity and their required mechanical properties, and whether non-linearity will be applied to every individual part of the structure or if simplifications can be utilized in that respect. Moreover, default meshing properties like mesher type and element size may influence the results, as will the method of introducing the loads onto the structure. Another challenge is modelling the foundation piles, and their structure-soil interaction, and determining to what level of detail they should be incorporated. Like for instance whether inclination of the piles or their horizontal stiffness will influence the stresses in the structure or not.

3.5.2. Foundation design

To be able to look at the model and interpret the results, understanding of the foundation design must be obtained. The way the load is transferred through the anchor cage into the structure and subsequently into the foundation piles should be studied. The influence the prestressing load on the anchor cage has on this distribution is important as well. This leads to a better understanding of the stress- and strain distribution along inside the structure.

3.5.3. Optimization

After the structural behaviour has been studied, the obtained insights can be used to determine how to perform limit state checks for the serviceability- and ultimate limit states, and whether the structure will comply or not. Subsequently this can then be used to study the possibilities into optimization of the foundation design, more specifically the applied reinforcement. Apart from altering the current reinforcement bar design, the possibility of applying steel fibre reinforced concrete and its effect can also be looked into.

4

The wind turbine foundation

In Figure 4.1 a picture of a typical on shore wind turbine foundation is shown. In this picture the sloped top, the pedestal and the insert ring, to be connected to the tower, can be seen. In this case the top is uncovered but this may still be covered by soil in a later stage of construction.

Figure 4.1: A recently finished wind turbine foundation

4.1. Model schematization

Figure 4.2 shows a simplified computer generated overview of half of the foundation structure, including the foundation piles.

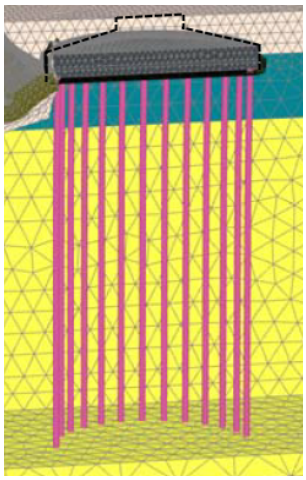

Figure 4.2: A simplified isometric view of half of a foundation structure including foundation piles but without the turbine tower

The main focus of this project will be the concrete structure connecting the turbine tower to the foundation piles beneath. A top view of this structure including the anchor cage, or insert ring, and the pedestal can be seen in Figure 4.3. In this figure the locations of the foundation piles have been indicated with dotted circles for an illustrative purpose, although in reality they can't be seen from the top.

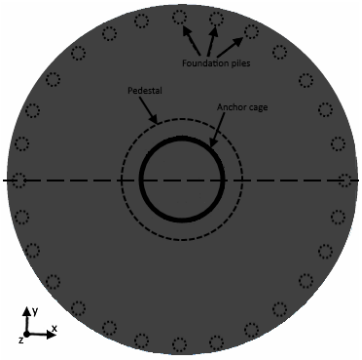

Figure 4.3: A top view of the foundation structure including the pedestal and the anchor cage. Additionally the placing of the foundation piles has also been indicated

In Figure 4.4 a schematic rendition of the connection between the turbine tower and the foundation structure is shown. It illustrates that the turbine loads are not defined exactly on the top of the foundation. The exact point of load application varies per manufacturer. This deviation results in an additional moment on the foundation centre of mass due to the horizontal wind load. In Figure 4.4 a partial schematization of the foundation piles is included as well.

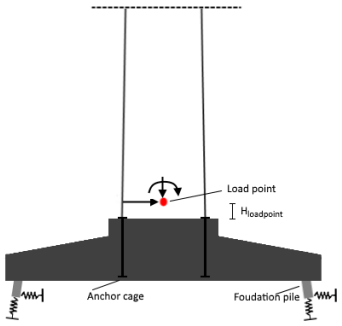

Figure 4.4: A more detailed schematic of the way the forces and moment are supplied by the wind turbine manufacturer. Also included is the anchor cage which looks like 2 tendons in cross-sectional view

4.2. Loading

There are several different load cases that influence the design of the foundation structure.

4.2.1. Load cases

In Figure 4.5 these loads are depicted schematically working on the cross section defined in Figure 4.5a. The most significant ones are the vertical-, horizontal-, and overturning moment loads exerted by the turbine, shown in Figure 4.5b, Figure 4.5c and Figure 4.5d repectively. The vertical load is the result of the weight of the turbine tower and the turbine itself. The overturning moment and horizontal load are the result of wind loading. The corresponding design loads are provided by the turbine manufacturer and differ for every type of turbine. These differences are caused by the size of the turbine but different manufacturers may prescribe different loads for similarly sized turbines and towers. In some cases the foundation design may include soil on top of the structure, this will produce a linearly decreasing distributed load from the outer edge towards the centre up to the point where the structure is above ground as shown in Figure 4.5e. If the groundwater level is higher than the underside of the structure, the water pressure will cause an upward distributed load as can be seen in Figure 4.5f. In Figure 4.6 the soil- and water levels, including minimum and maximum expected deviations, are shown for the reference project. These levels may vary for other projects, as shown schematically in Figure 4.6, and should be applied to the model accordingly.

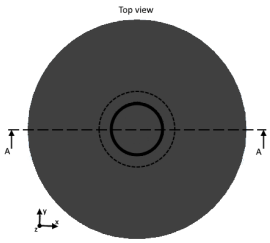

(a) Top view of the foundation construction with location of cross section A-A used to show different loads

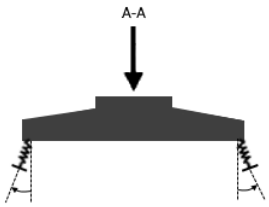

(b) Schematic representation of the vertical turbine load

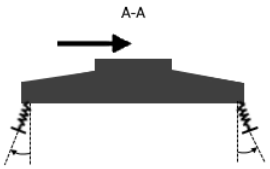

(c) Schematic representation of the horizontal turbine load

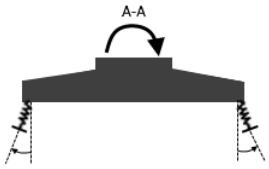

(d) Schematic representation of the turbine moment load

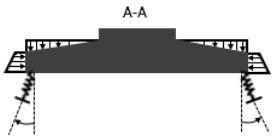

(e) Schematic representation of the soil load on the structure in case of it being (partially) covered

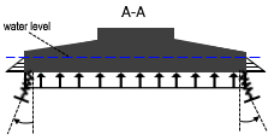

(f) Schematic representation of the water pressure on the structure in case of the ground water level being above the bottom of the structure

Figure 4.5: Mechanical schematics of the different types of loading on the foundation structure

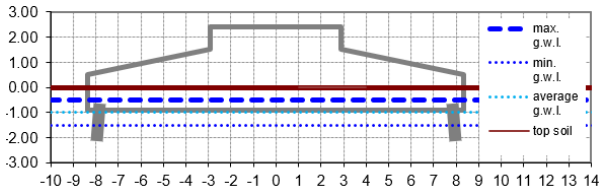

Figure 4.6: Schematic representation of a cross section of the foundation structure

4.2.2. Characteristic loading

The loading used in the calculations is provided by the manufacturer. The loading for the wind turbine in the reference project is shown in Table 4.1. The operational load used in the foundation design is the 1/100 year exceeding load, according to the Germanische Loyd Guidelines 2010. The fatigue load is determined using the mean load $+/-0.5\times$ the equivalent load (p.t.p), using inverse S-N slope 9. To determine the applicable safetyfactors the following was used:

- Consequence class : CC2 (tabel B1 NEN-EN 1990-1-1)
- Reliability class : RC2 (tabel B2 NEN-EN 1990-1-1)
- Design life : 20 years (tabel 2.1 NEN-EN 1990-1-1)

The specifications from the wind turbine supplier, to which RHDHV designs the foundation, are the following about dynamic effects of the wind turbine in operational mode:

> The load assumptions are according to the IEC 61400-1 normal, class IEC as per specifications for WTG1. This causes loads from the turbine tower on the foundation as mentioned in the load specification which is added to the calculation in appendix 1. Extreme winds cause the maximum loads on the foundation; in this case the wind turbine is not operating. These loads can be qualified as quasi-static. Therefore the calculations of the maximum loads are performed in a similar way as for the static loads.

Table 4.1: Nominal loading of a Nordex N117/3600 – HH120 m IEC2, IECS, IEC3a NCV wind turbine

Load type:		Extreme	Operational	Fatigue			
				Mean	p.t.p.	Max	Min
Horizontal loads	Fres (kN)	1004	556	304	356	482	126
Vertical loads	Fz (kN)	-5334	-5494	-5176	-116	-5234	-5234
Bending moments	Mres (kNm)	123538	65677	40255	35024	57767	22743

The nominal loads used in the reference project and consequently for the analyses used for the comparisons in this project can be found in Table 4.1.

The previously described loads can be elaborated on slightly and therefore the following loads are considered in the 2D plate model:

1. Self weight foundation block
2. Dead load turbine (tower + nacelle + blades)
3. Soil load on top of foundation
4. Ground water, maximum level
5. Ground water, minimum level
6. Ground water, average level
7. Wind, Extreme
8. Wind, Operational
9. Fatigue, Maximum
10. Fatigue, Minimum

4.3. Turbine connection to the foundation

A turbine is connected to the foundation through an anchor cage as shown in Figure 4.7 or an insert ring. Because the forces are transferred vertically the exact effects of loading are hard to estimate in a 2D model, while they should be easy to find once this cage is integrated in a 3D model. The anchor bolts are prestressed to improve the fatigue behaviour of the anchor by ensuring the base of the tower remains connected to the foundation despite of the tensile forces caused by moment loading. By doing so the stiffness of the connection is automatically increased since the behaviour will be determined by the mobilised concrete as opposed to only the longitudinal stiffness of the anchor bolts. The expectation is that incorporating the prestressing load into the 3D model will lead to stiffer behaviour of the structure.

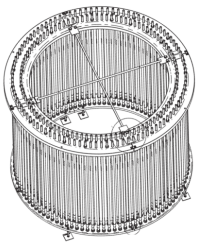

Figure 4.7: A typical anchor cage

4.4. Foundation piles

As the foundation structure is essentially only a means to transfer the turbine loads to the foundation piles in the soil, these piles need to be taken into account. In a simplified model these piles, and their interaction with the soil, may be modelled as springs. The properties of these springs are based on the information supplied by the geotechnical engineers at RHDHV. For the linear analysis the vertical pile stiffness, $k_{pile,vert}$ was determined to be:

$$k_{pile,vert} = 170\text{MN}\,\text{m}^{-1} \tag{4.1}$$

In addition to the vertical spring stiffness the horizontal resistance may also influence the results in a 3D model analysis. It is difficult to determine the exact horizontal spring constant per pile, therefore the total horizontal stiffness, k_{hor}, that is required for the entire structure is given. This should satisfy the following demand:

$$k_{hor} = 540\text{MN}\,\text{m}^{-1} \tag{4.2}$$

In practice the software package GROUP is used to determine whether a proposed foundation pile design will satisfy the demand.

5

Models for linear analysis in 2D and 3D

As described RHDHV currently uses a 2D plate model for linear analysis to determine the pile forces and required reinforcement. In this chapter some of the aspects of this model will be discussed. Additionally the modelling considerations that are necessary to obtain a 3D model from this 2D model are described. To adequately determine the distribution of forces, moments, stresses and displacements in a structure to be able to check or improve the design the model used to do the calculations must reflect the reality sufficiently without becoming to complex to be handled. Additionally it is also important to be able to interpret and visualize the results. There are a lot of modelling options and possible simplifications of reality available, so choices have to be made and validated. This chapter will describe these choices and the resulting model to be used for the linear analyses.

5.1. Result visualisation for comparison between 2D and 3D models

To be able to compare the 2D and 3D models similar output data needs to be produced. This data should also be presented in a way that enables comparison, which can require additional modelling. An example of this is that the distributed moments are directly visible in a 2D model while this is not the case for a 3D model. In contrast to this, for a 2D model, it is required to take extra steps to visualize the stress distribution over the height. This is not required for a 3D model.

In Figure 5.1 some of the simplifications, made to the basic structure to obtain the 2D plate model, are shown. Figure 5.1a shows the top view with the pedestal and the load spreading plate. In Figure 5.1b cross section A-A is shown with the pedestal in a lighter shade of grey to reflect the fact that it was not included in the 2D plate model. Figure 5.1c schematically represents the final plate model in which the height of the structure has been included by defining a geometry thickness. In Diana this thickness is automatically assumed to be symmetrically distributed under and above the model elements. This results in the fact that the plate is always in the centre of mass of the foundation.

To be able to study the effects of the actual proposed reinforcement design, the simplifications used in the 2D model can not be applied to a 3D model without losing critical information. And as this model will be used to get a more detailed understanding of the structural behaviour the pedestal is included. To be able to visualize and compare the the internal distributed forces and moments in both models, a composed surface element cross section is used in the 3D model. Composed surface elements calculate distributed moments and forces over a defined height on both sides from the primary Cauchy stresses in solid elements and reinforcements located in said elements that are intersected by the normal line. To be able to compare the results, this composed element surface needs to be at mid height, at the centre of mass, of the structure at every point along the x-axis. This is shown in Figure 5.2.

Because the composed surface elements are shell elements their local z-axis is always perpendicular to the surface and as the distributed moments and forces in them are calculated along the local z-axis, using a tapered surface following the mid height of the structure does not yield the required results, as this local z-axis will not coincide with the global definition. Therefore this composed element surface needs to be divided into several rings, placed at different heights in the centre of mass, with local z-axes along the global z-axis. This yields a discrete distribution of the elements over the height instead of a continuous one, but since the elements themselves are also finite in size this won't cause a problem as long as the rings are narrow enough.

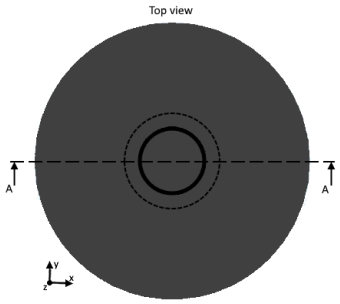

(a) Top view of the foundation construction

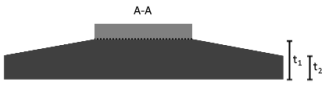

(b) Cross section A-A including the pedestal which was not modelled in the 2D model

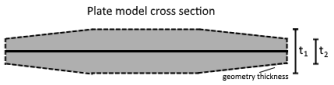

(c) Similar cross section of the 2D plate model in which the model and the geometry thickness are shown

Figure 5.1: Overview of simplification for the 2D model

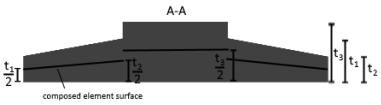

Figure 5.2: Schematic cross section A-A for the 3D volume element model including the desired location of the composed element surface

In this model rings with a width as large as the default element size are used. In Figure 5.3 these discrete rings are shown in the model. Figure 5.4 depicts an isometric view of the discrete rings for better visualisation.

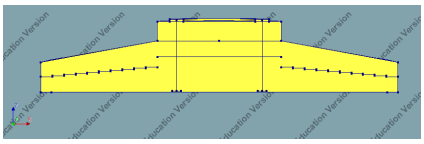

Figure 5.3: Cross sectional side view of the 3D model in which the composed element rings can be seen

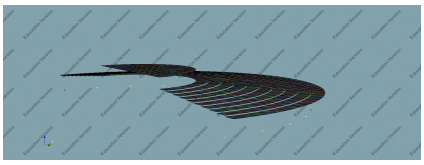

Figure 5.4: An isometric view of the meshed composed surface element rings

5.2. Translation to reinforcement

In the 2D plate model CQ40S quadrilateral (Figure 5.5a) and CT30S triangular (Figure 5.5b) shell elements were used. These can be used to find the distributed moments and forces. In Figure 5.6 the relations used to find the moment distribution in the centroidal cross section are depicted. Additionally the distributed reinforcement moments in the top and bottom layers, shown in Figure 5.7, can be determined. Figure 2.2b and Figure 2.2a in chapter 2 are examples of this output.

In the 3D volume element model the necessary reinforcement can be determined more accurately by looking at the stresses and strains in the structure after loading. However, to be able to compare the results of the 3D model to the 2D model for validation the previously described composed element surface is used.

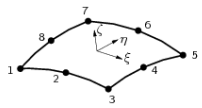

(a) A CQ40S quadrilateral shell element used in the 2D plate model

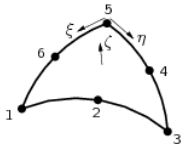

(b) A CT30S triangular shell element used in the 2D plate model

Figure 5.5: The two types of elements used in the 2D plate model[7]

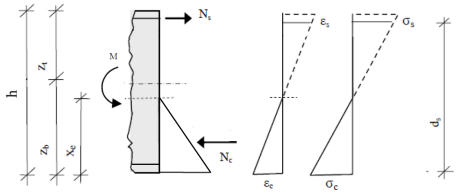

Figure 5.6: The relation between stresses, strains, internal moments and forces in a beam or slab under loading that causes bending with extension in the upper side

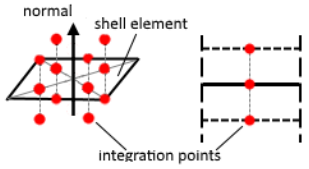

Figure 5.7: Default 2 × 2 × 3 Simpson's (reduced) integration scheme for a CQ40S shell element

5.3. Model considerations

As previously described, to be able to obtain a finite element model from a mechanical model certain choices have to be made. These choices are based on the information that is to be extracted from the model and the type of input.

5.3.1. Concrete material properties

For the linear model the material properties of the reference project were used for concrete. These are summarized in Table 5.1. The specific weight and Poisson's ratio were determined by RHDHV based on the concrete class and the effective Young's modulus was calculated using a weighed average, over the area of occurrence based on a preliminary calculation, of the cracked and uncracked concrete Young's moduli.

Table 5.1: Material properties of concrete

Specifications	
Young's modulus	25900 N mm^{-2}
Poisson's ratio	0.20
Specific weight	24 kN m^{-3}

5.3.2. Whole circle versus demi-circle

For the 2D model the whole circular cross-section was modelled. As a linear analysis does not require exceptionally small elements which can also be said for a simple plate model, computational efficiency was not a big issue. However when looking at a 3D model with volume elements the number of elements and consequent amount of calculations increases substantially. And since this is only a step on the way to modelling non-linearity, which in general requires smaller elements and longer calculations, increasing the efficiency becomes more interesting. Symmetry is often a way of making a more computationally efficient model, and in the case of 3D volume elements it also provides an easy way to analyse stresses in the cross section through the centre. For this circular structure, modelling half of the structure or even just a quarter may be considered. The latter however can be dismissed quickly due to the different types of simultaneous loading. In several load combinations, like a moment load and a vertical load, the different boundary conditions required

to impose symmetry conditions would conflict. Modelling only half the circular shape also requires some acuity because of the variable amount of foundation piles and their location. If only fixed supports would be taken into account a line support could be applied and using symmetry would always be possible, however individual springs are more complicated because the stiffness of the piles on the cross section edge should have modified values for the spring constant k_{pile}. Additionally a symmetry boundary condition has to be applied. In this case the displacement in y-direction was set to 0 for the entire surface along the x-axis. This boundary condition is shown in Figure 5.8. In this figure the set of different discrete supports in y-direction represents a continuously supported surface.

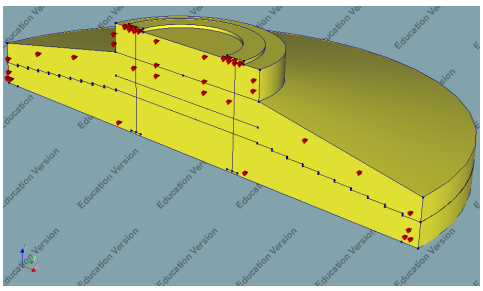

Figure 5.8: Isometric view of the structure in which the symmetry boundary condition can be seen

5.3.3. Element types and sizes

The default element size was initially chosen as $h = 0.5$ m. A mesh size dependency study will be performed during the model validation process to determine the effect of this parameter. However in Figure 5.9 a comparison between a fine and a more coarse mesh is shown and although the finer mesh does provide a better idea of the distribution it can be observed that both yield rather capricious moment distributions in de composed surface.

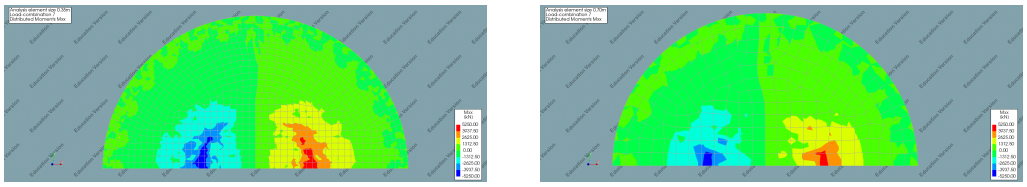

(a) Mxx with element size h=0.35m hexa/quad elements

(b) Mxx with element size h=0.70m

Figure 5.9: Comparison between a fine and a coarse mesh hexahedra/quadrilateral elements

Because of the historical use and development of the finite element method in structural mechanics hexahedra elements combined with quadrilateral elements are commonly used. As stated before the 2D surface element model was made up out of quadrilateral shell elements supplemented with triangular ones to be able to mesh the circular cross-section. To compare the results obtained from this model to the ones from the 3D volume element model initially Hexa/Quad elements were applied as default element type. However Hexa/Quad elements have limitations when applied to irregular shapes, and considering the fact that the top of the structure consists mainly of a sloped circular edge the application of Tetrahedral elements can be beneficial and lead to a more regular mesh. While a regular mesh is always desirable for finite element analysis this is even more so the case for an analysis in which composed surface elements are used to find results, due to the nature of the applied procedure.

In Figure 5.10 the distributed moments found by doing a similar analysis with different types of elements are shown next to each other. It is clear that the model with tetrahedra yields a visually smoother result, that is also slightly more symmetrical. Noteworthy however is the fact that while the same element size was used, the model composed of tetrahedra requires more elements and was more computationally expensive. Because at this stage these downsides are not very significant tetrahedral elements will be used because they yield more accurate results, and smoother distribution over the elements.

As not all shapes can be modelled using exclusively Hexa/Quad elements, using these as the default element type yields a mesh with a combination of the following element types:

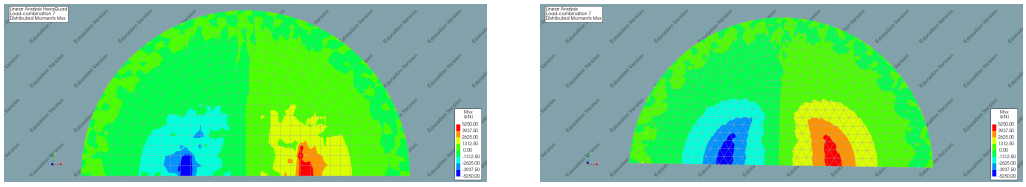

(a) Mxx in the composed element cross-section in a model composed of hexahedra (h=0.50m) LC7

(b) Mxx in the composed element cross-section in a model composed of tetrahedra (h=0.50m) LC7

Figure 5.10: Comparison between models with hexahedron and tetrahedron elements as default

- CHX60: a twenty-node isoparametric solid brick element. Figure 5.11a
- CPY39: a thirteen-node isoparametric solid pyramid element. Figure 5.11b
- CTE30: a ten-node, three-side isoparametric solid pyramid element. It is based on quadratic interpolation and numerical integration. Figure 5.11d
- CTP45: a fifteen-node isoparametric solid wedge element. It is based on quadratic interpolation and numerical integration. Figure 5.11c

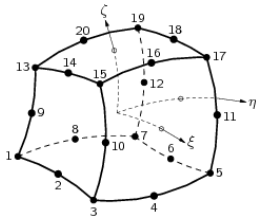

(a) CHX60

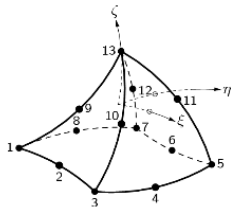

(b) CPY39

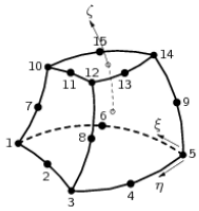

(c) CTP45

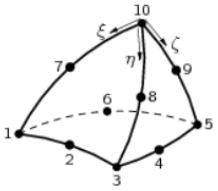

(d) CTE30

Figure 5.11: The different volume element types used[7]

The previously described composed element surface is made up out of the following surface element types:

- CQ8CM: an eight-node quadrilateral curved base element. It must be combined with a composition of CHX60 solid brick elements to form a composed solid element. Figure 5.12a
- CT6CM: a six-node triangular curved base element. It must be combined with a composition of CTP45 solid prism elements to form a composed solid element. The orientation of the triangular faces of the prisms must match the orientation of the base element. The 'integration scheme' in the triangle is 4-point which matches the default $n_{lc} = 4$ of the CTP45 element. Figure 5.12b

As previously described using tetrahedra as default elements yields a more regular mesh, this can also be seen in the element types required to form the entire mesh. In this case only CTE30 elements, shown in Figure 5.11d, were used for the structure itself and for the composed surface only CT6CM elements, as shown in Figure 5.12b, are required.

When modelling the supports as springs, material properties are attached to vertices to model the geotechnical behaviour of the piles. To model springs another distinct element type is used: SP1TR for linear springs. The SP1TR element is a one-node translation spring/dashpot. This element type is show in Figure 5.13

(a) CQ8CM (b) CT6CM

Figure 5.12: The surface element types used to produce the composed element surface[7]

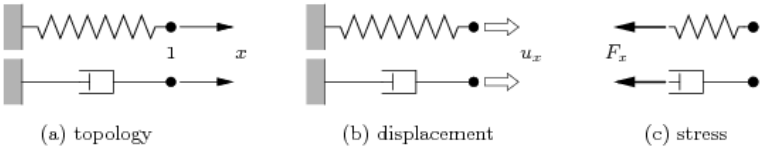

Figure 5.13: Spring element SP1TR[7]

5.3.4. Modelling the anchor cage

In Figure 5.14 a side view and a cross section of the anchor cage is shown. It consists of two load spreading plates and 2 rows of anchor bolts in between.

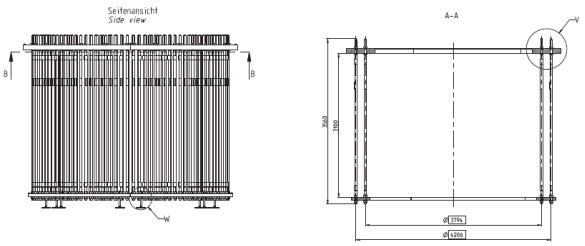

Figure 5.14: Sideview and cross section of an anchor cage

Using tetrahedra elements that are too big in the LSP produces elements with very sharp angles that are could spawn numerical errors due to the small height of the plate. Therefore the LSP is meshed using smaller elements than used for the concrete parts. To avoid unnecessary mesh refinement and consequent irregularities in the mesh around the bottom LSP, the bottom LSP was simply modelled as a ring shaped sheet and the geometry is defined as reinforcement grid with the height of the LSP as effective thickness in both directions. In addition to this plate a cylindrical shell was modelled to be able to apply the prestressing load to a defined reinforcement grid geometry with bars defined only in vertical direction. In Figure 5.15a and Figure 5.15b the load spreading plates and cylindrical shell are shown.

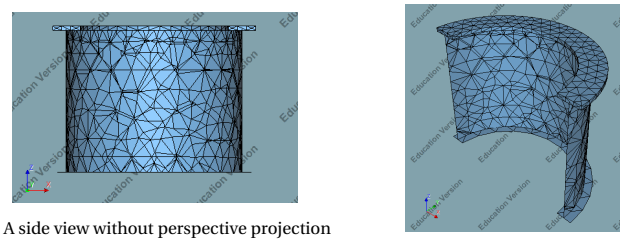

(a) A side view without perspective projection showing the meshed load spreading plates and prestressing tendons shell

(b) An isometric view of the meshed load spreading plates and anchor cage

Figure 5.15: Method for moment load introduction

For the load spreading plates the properties in Table 5.2 are used. An increased stiffness was used for the top LSP to take into account the effect of the tower placed on it. The bottom plate has a normal Young's modulus as it is not affected by the tower and using overly stiff material would influence the stress distribution in the bottom of the structure too much.

Table 5.2: Material properties of steel

Specifications	
Young's modulus top LSP	$2e11\,\mathrm{N\,mm^{-2}}$
Young's modulus bottom LSP	$2e8\,\mathrm{N\,mm^{-2}}$
Poisson's ratio	0.29
Specific weight	$78\,\mathrm{kN\,m^{-3}}$

5.3.5. Local axes

Because the prospective reinforcement design is axisymmetric it is convenient to define all distributed moments such that the primary directions are also centred around the middle of the structure. Therefore the local axes in the composed element surface are defined as shown in Figure 5.16.

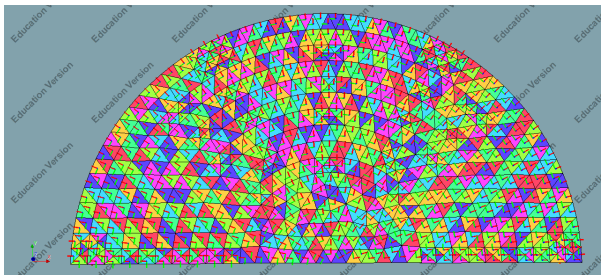

Figure 5.16: Definition of local axes

5.3.6. Resulting mesh

Figure 5.17 shows an isometric view of the meshed structure that is the result of the previously described modelling choices, and in Figure 5.18 the cut surface is shown in its meshed form. There is a mesh refinement that can be seen around the top load spreading plate.

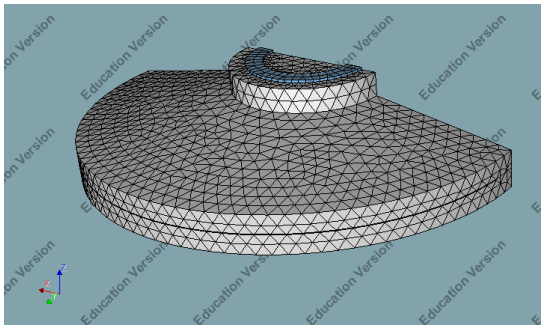

Figure 5.17: An isometric view of the meshed 3D FEM model

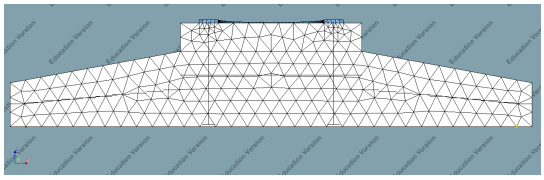

Figure 5.18: A side view along the x-axis of the meshed 3D FEM model

5.4. Supports

The 2D plate model only took into account the vertical pile stiffness as the horizontal wind load was exclusively modelled by determining its contribution to the overturning moment. Therefore only vertical piles were considered. The contribution of the the soil stiffness to the horizontal resistance was checked in the

geotechnical model. The supports that were modelled are shown in Figure 5.19. Because the first step in this design process is obtaining a 3D model that is comparable to the existing 2D model the initial supports used are the same. After comparing the 2D and 3D results a more extensive pile head model was used.

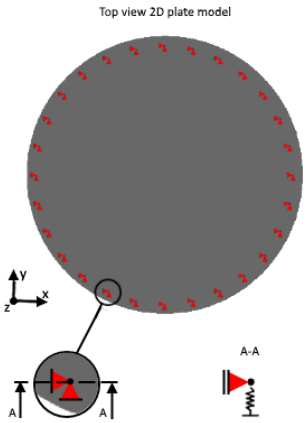

Figure 5.19: A detail of the supports used in the 2D plate model shown in reference to the plate model

In Figure 5.20 the model design process is shown in a stepwise manner. In Figure 5.20b the 2D plate model is shown including the defined geometry thickness. Subsequently Figure 5.20c shows the 3D model that uses horizontally fixed springs comparable to the supports used in de 2D model. In Figure 5.20d the fixed supports at the location of each pile were replaced by a single horizontally fixed support in the centre of the structure. In Figure 5.20e it can be seen that the inclination of the foundation piles was included. As a last step the horizontal pile resistance, as a result of soil resistance, was modelled as additional horizontal springs in de opposite direction of the horizontal load. The value used for this resistance was derived from the horizontal resistance demand of the structure. The total resistance was divided by the number of piles as shown in Equation 5.1. In this equation $k_{pile,hor}$ is the horizontal stiffness per pile and N_{piles} is the number of foundation piles. This method is conservative as the actual pile design is always higher than the demand in reality, while at the same time it does ignore the fact that the interaction between the structure and the soil also contributes to the horizontal stiffness of the total construction. Contrary to the horizontal components of the inclined pile springs which are defined radially, the soil resistance springs were all modelled in the same direction. for the cross-section along the x-axis this looks like is shown in Figure 5.20f. The horizontal spring constant per pile was found by dividing the total demanded horizontal spring constant by the amount of piles as these can be considered to form a parallel system. This yields conservative spring constants since the total resistance is always checked to be higher than the demand. Note that the supports in Figure 5.20b are placed slightly closer to the centre of the structure as an inclination of the piles was taken into account to determine where the supports would be attached at the cross section at mid-height.

$$k_{pile,hor} = \frac{k_{hor}}{N_{piles}} = \frac{540\text{MN m}^{-1}}{28} = 19.3\text{MN m}^{-1} \tag{5.1}$$

Solely using inclined springs, modelled with a working direction with the z-axis in the direction of the corresponding foundation pile, produces a convergence criterion error in Diana. To remedy this problem an additional horizontal support can be introduced to the situation in Figure 5.20d, as shown in Figure 5.21. This means that horizontal displacements of the entire structure caused by horizontal loading are prohibited, while the extension of the underside of the structure is still only restricted by the horizontal components of the pile springs Despite Diana not being able to entirely solve the linear set of equations it does produce credible results for load cases that do not include horizontal loading. The pile forces from these results were compared to the ones produced by the model with the additional support and they are similar with differences that are within 1% of the total resulting forces.

Because the inclination of the piles will still be quite close to vertical the horizontal pile force components are not expected to be very large and thus they will most likely not contribute greatly to the distributed moments in the structure.

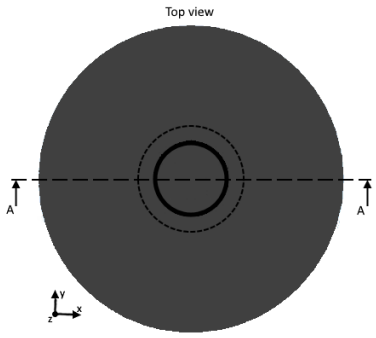

(a) Top view of the foundation construction in which cross section A-A is shown

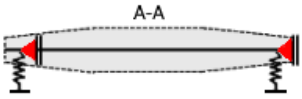

(b) Cross section of the 2D plate model showing vertical spring supports that are fixed in horizontal direction

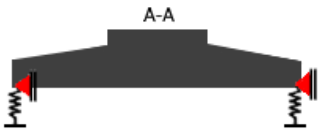

(c) Cross section of the 3D model showing vertical spring supports that are fixed in horizontal direction comparable to the supports used in de 2D model

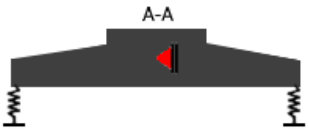

(d) Cross section of the 3D model showing the foundation piles as vertical springs while the centre is supported laterally

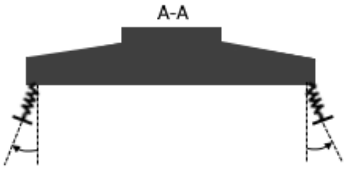

(e) Cross section of the 3D model with inclined springs to model inclined foundation piles

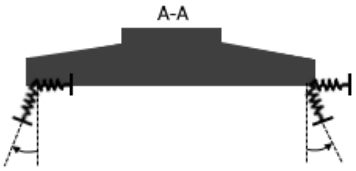

(f) Cross section of the 3D model with inclined springs to model tilted foundation piles, with additional horizontal springs representing the vertical pile stiffness due to interaction with the soil

Figure 5.20: Overview of simplification for the 2D model

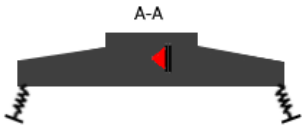

Figure 5.21: Cross section of the 3D model with inclined springs to model the foundation piles and an additional support to function as an additional boundary condition

5.4.1. Multi-linear springs as supports

Furthermore although some of the piles are subjected to tension a linear spring with $k_{pile,vert} = 170\text{MN m}^{-1}$was used to model the pile. Linear springs provide a good initial insight into the displacements of the structure and the corresponding pile forces, but assumptions have to be made that these remain within boundaries for which the piles still behave linearly . If these limitations are exceeded and the foundation piles fail, re-distribution of forces will occur, and it is desirable to determine the effects and their magnitude. The spring properties that are used in this case are based on the interaction between pile and soil. This interaction differs per location of each pile, but a typical load-displacement diagram for the reference project can be seen in Figure 5.22. Although tensile behaviour is not as readily available, the loads and displacements in the load-displacement diagram were reduced to one third to take into account the fact that the pile tip only offers additional resistance to downwards displacement.

It is possible to use a combination of linear functions to describe this behaviour using the displacements and corresponding loads from this diagram. However a more generalized bi-linear approach is used that makes use of modified pile stiffnesses and a bi-linear point. Subsequently a spring was used that is described using an elongation-force diagram. For both the behaviour in compression and in tension a high spring constant was used up to 80% of the failure load, after which a reduced spring constant was used until the failure load was reached. The elongations corresponding to these failure loads were calculated using Equation 5.2.

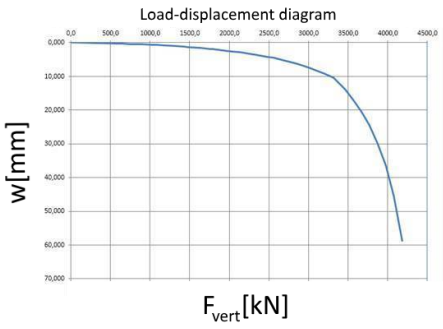

Figure 5.22: Typical load-displacement diagram for a foundation pile in tension for the Wieringermeer project

Here $k_{pile,high}$ is the vertical pile stiffness used to approximate the initial slope of the load-displacement diagram, and $k_{pile,low}$ is the lower vertical pile stiffness to represent the second slope. $\Delta u_{80\%}$ is the displacement at 80% of the maximum determined displacement value $\Delta u_{80\%}$. Finally, $F_{failure}$ is the maximum load the pile can carry before failing. This yields a diagram like the one shown in Figure 5.23. The failure loads and pile stiffness in both compression and tension vary per project because besides being influenced by the type and dimensions of the pile itself they are dependent on the soil properties on the building site as well. The factors used in these calculations are based on Figure 5.22

$$\begin{aligned} k_{pile,high} &= 2k_{pile,vert} \\ k_{pile,low} &= k_{pile,high}/25 \\ \Delta u_{80\%} &= \frac{0.80F_{failure}}{k_{pile,high}} \\ \Delta u_{100\%} &= \Delta u_{80\%} + \frac{(1-0.70)\,F_{failure}}{k_{pile,reduced}} \end{aligned} \tag{5.2}$$

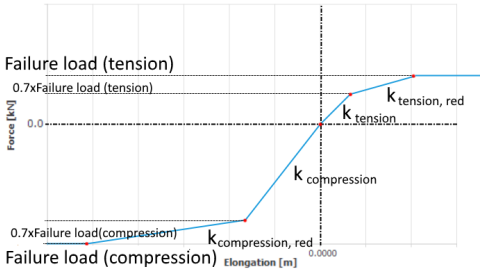

Figure 5.23: Elongation-force diagram used in the model to include non-linearity for the pile stiffness

5.5. Loads

The loads caused by water pressure and soil are simply incorporated in the model as distributed loads on their respective surfaces or rather as a linearly decreasing distributed load in the case of soil loading. The vertical, horizontal turbine loads are also modelled as distributed loads on the top face of the top load spreading plate in their respective directions. The moment loads are less straight forward as they are a direct result from the turbine tower, and as the tower has a ring shaped horizontal cross section the moment will have to be introduced as a varying distributed load with values chosen accordingly.

5.5.1. Introducing loads for the 2D model

In the 2D model the foundation structure was modelled as a plate at mid height with the corresponding thickness as geometry.

Because of this, assumptions had to be made about the introduction and distribution of the loads. In reality the load is introduced to the concrete via a steel O-shaped ring. Subsequently it spreads out over an increasing area along the height of the structure. In the 2D model a set of 3 circular line loads was used to simulate this. The method used to achieve this is shown schematically in Figure 5.24. It was assumed that the ratio of spreading to height is 1. In a 3D model these assumptions do not have to be made as the distribution is calculated naturally.

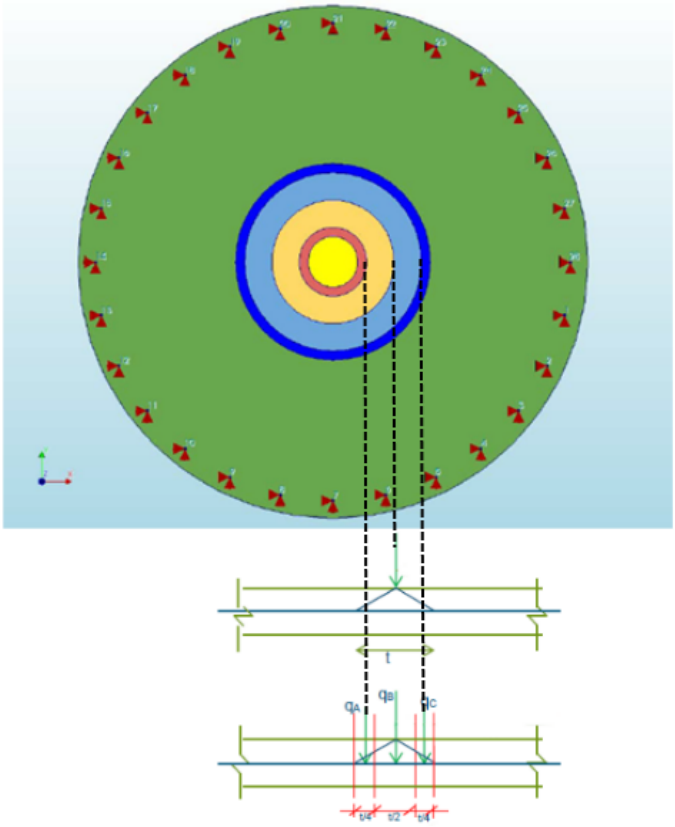

Figure 5.24: Introduction of forces from the tower as assumed for the 2D plate model

To apply a moment in the shape of a ring certain steps need to be taken. A function has to be used as shown in Figure 5.25. The values that need to be used for the functions and accompanying loads are found by using the moment of inertia of every individual ring as a part of the total moment of inertia of the area over which the load is distributed and the corresponding radii.

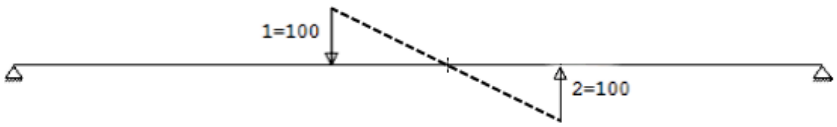

Figure 5.25: Method for applying a moment by using line loads

5.5.2. Load introduction for the 3D model

Unlike for the 2D model in which line loads were used to model the introduction and spreading of the forces and moments, for the 3D model surface loads were used which acted on a steel load spreading plate. To be able to do this the moment caused by wind loading had to be translated to a maximum stress by using the moment of inertia and the radius of the load spreading plate. This stress was subsequently attached to the

load spreading plate using a linear function going from 1 to -1 in between the outer diameter of the LSP.

The extreme values for the distributed load representing the moment load are determined similarly to the way the maximum stress corresponding to a bending moment in a circular hollow section is determined. This is compared in Equation 5.3 and Equation 5.4.

$$\sigma_{max} = \frac{M_{bending}}{S_{CHS}} = \frac{M_{bending}}{I_{CHS}} r_{out} = \frac{M_{bending}}{\frac{\pi}{4}\left(r_{out}^4 - r_{in}^4\right)} r_{out} \tag{5.3}$$

Where:

- σ_{max} = maximum normal stress in a beam cross-section;
- $M_{bending}$ = bending moment in a beam;
- I_{CHS} = moment of inertia of a circular hollow section;
- r_{out} = outer radius of a circular hollow section;
- r_{in} = inner radius of a circular hollow section.

So analogously:

$$q_{moment} = \frac{M_{wind}}{\frac{\pi}{4}\left(r_{LSP,out}^4 - r_{LSP,in}^4\right)} r_{LSP,out} \tag{5.4}$$

Where:

- q_{moment} = maximum for the distributed load used to model a moment load on the LSP;
- M_{wind} = moment load due to wind;
- $r_{LSP,out}$ = outer radius of the LSP;
- $r_{LSP,in}$ = inner radius of the LSP.

The primary reason to do so is because it is more realistic, which is the initial goal of the model transformation, and it provides the possibility of realistically introducing the prestressing forces in the anchor cage. Additionally it provides a more straight forward method of introducing the horizontal wind loads and there is an actual area over which the load, that has been described as a single horizontal force, may be distributed. Of course in reality the LSP is loaded by the turbine tower. This can be seen as a cylindrical shell, which results in circular line loads on the LSP. However, as distributed loads are more favourable than concentrated ones in non-linear analysis, this method was used with the next step of the project in mind.

Previously the anchor cage and the way it was incorporated in the model was shown. Again in Figure 5.14 a side view and a cross section of the anchor cage can be seen, it clearly shows the load spreading plate which was used to introduce the turbine loads in the model. The way the moment load is simulated is described in Figure 5.26. Figure 5.26a shows where the cross section A-A is located relative to the x-axis. In Figure 5.26b the linear function used to introduce the moment load is depicted. applying this function to a distributed load over the area of the LSP yields the distributed load shown in Figure 5.26c. To clarify the nodal equivalent forces that are the result of this method are shown in Figure 5.27 working on a meshed LSP in isometric view.

5.5.3. Anchor cage prestressing load

For the previously described grid geometry on a cylindrical shell the local x-axis was taken in the global z-axis so the prestressing could be applied in the correct direction. This also provided the possibility to define bars in the local x-direction exclusively and the ability to use the spacing and diameters of the actual anchor cage as direct input.

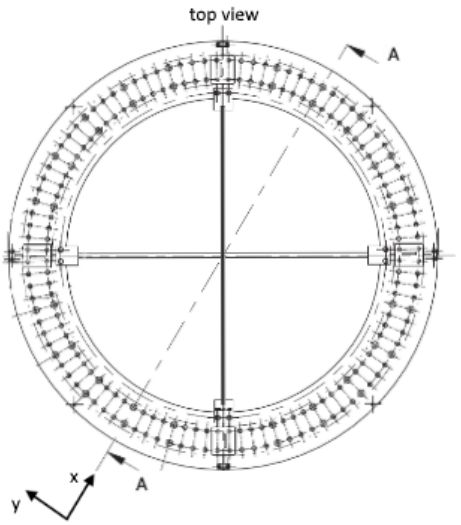

(a) Top view of the anchor cage and load spreading plate with cross section A-A indicated

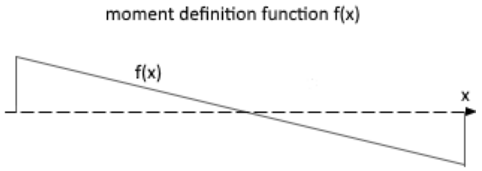

(b) The function along the x-axis applied to a distributed load used to introduce a moment load to the LSP and subsequently to the foundation structure

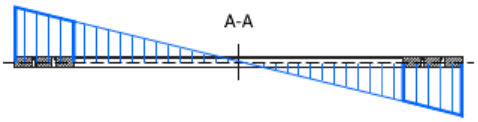

(c) The distributed load on cross section A-A that is used to simulate a moment load

Figure 5.26: Method for moment load introduction

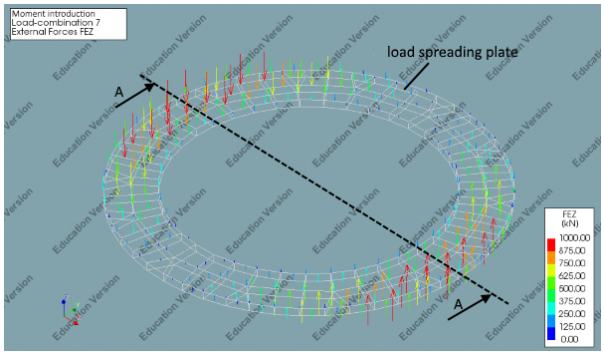

Figure 5.27: Vector diagram of external nodal forces on the meshed LSP shown in isometric view

5.5.4. Load cases and combinations

One of the most important differences in loading between the 3D and 2D models is the way the moments that are resultant of the horizontal wind loads are treated. In case of the 2D model all the horizontal loading is translated to a moment by multiplying by a predefined lever arm, which is depicted in Figure 4.4. Because this lever arm does not always coincide with the hight of the pedestal and load insert ring as was shown in Figure 4.4, in the 3D model the effect of the horizontal force is taken into account by using a combination of

the horizontal force and a multiplication of it bt the difference between the defined arm and the height of the insert ring.

For the 2D model the previously stated load combinations yield Table 5.3

Table 5.3: Load combinations used in the 2D model

		Combinations Used									
		Dead	Turbine_SW	Soil	Gr_water_max	Gr_water_min	Gr_water_avg	Extreme	Operational	Fatigue_max	Fatigue_min
Load cases	Geometry load combination 1	1.00									
	Geometry load combination 2		1.00								
	Geometry load combination 3			1.00							
	Geometry load combination 4				1.00						
	Geometry load combination 5					1.00					
	Geometry load combination 6						1.00				
	Geometry load combination 7							1.00			
	Geometry load combination 8								1.00		
	Geometry load combination 9									1.00	
	Geometry load combination 10										1.00
ULS Max	Geometry load combination 11	1.35	1.35	1.35		1.00		1.10			
ULS Min	Geometry load combination 12	0.90	0.90	0.90	1.00			1.10			
SLS Fatigue max	Geometry load combination 13	1.00	1.00	1.00			1.00			1.00	
SLS Fatigue min	Geometry load combination 14	1.00	1.00	1.00			1.00				1.00
SLS Extreme	Geometry load combination 15	1.00	1.00	1.00			1.00	1.00			
SLS Operational	Geometry load combination 16	1.00	1.00	1.00			1.00		1.00		
Analysis Load case	Geometry load combination 17							0.973			

Table 5.4: Additional Load combinations used in the 3D model

		Combinations Used												
		Dead	Turbine_SW	Soil	Gr_water_max	Gr_water_min	Gr_water_avg	Wind extreme	Wind operational	Fatigue_max	Fatigue_min	Add extreme moment hor wind	Add operational moment hor wind	prestressing load
Load cases	Geometry load combination 18										1.00			
	Geometry load combination 19	1.35	1.35					1.1	1.00		1.1			
	Geometry load combination 20							1.00			1.00		1.00	
	Geometry load combination 21													1.00
	Geometry load combination 22							1.00				1.00		
	Geometry load combination 23							1.00				1.00		1.00

The first 10 load combinations are simply the load cases. The other combinations are the following:

- Combination 11 & 12 are ULS - only extreme load case used as it is the worst case
- Combination 13 & 14 are Fatigue
- Combination 15 & 16 are SLS
- Combination 17 Extreme wind load with correction factor for comparison between 2D and 3D
- Combination 18 LC Horizontal wind load extreme
- Combination 19 includes horizontal load ULS max
- Combination 20 includes horizontal force and moment weight 1
- Combination 21 prestressing only
- Combination 22 extreme moment only
- Combination 23 extreme moment + prestressing anchor cage

For comparison between the 2D and 3D models LC2 (vertical loading from the turbine), LC17 or LC18 (the reduced moment load, as to not take into the account the effect of the horizontal loading from the turbine) in the 2D model were compared to LC2 (vertical loading turbine), LC7(moment loading only without the moment effect from the horizontal wind load) in the 3D model respectively.

LC7 in the 2D model can also be compared to LC22 in the 3D model(The extreme moment including horizontal loading). However this is only partly possible as LC7 in the 2D model does not take into account the horizontal force itself thus neglecting the resulting horizontal displacements, strains and corresponding stresses.

To be able to compare 2 equal situation a correction factor that scales the moment load including the horizontal wind load in the 2D model to a moment load without it is required. It was calculated as shown in Equation 5.5 for the reference case specifically.

$$\begin{aligned} M_{c.o.m.} &= M_{top} + H_{wind} d_{wind} \\ r &= \frac{M_{top}}{M_{c.o.g.}} = \frac{123538}{126943} = 0.973 \end{aligned} \tag{5.5}$$

Where:

- $M_{c.o.m.}$ = the moment applied to the centre of mass on the vertical axis in the 2D model;
- M_{top} = the moment at the top of the pedestal as specified by the supplier;
- H_{wind} = the horizontal wind load as specified by the supplier;
- d_{wind} = the offset between the centre of mass and the point of application for the horizontal load.

However the moment exerted by the external forces and the reaction forces (nodal equivalent) multiplied by their distance from the centre in the x-direction for LC7 in the 2D model resulted in a moment of only 125650kN m instead of 126943kN m. With the same check a moment of 123231kN m for the 3D model was found, which is closer to the actual moment of 123538kN m. The difference may be corrected with a correction factor if necessary. Therefore an additional load combination was introduced into the 2D model. As only 17 load combinations are present in the 2D model this is LC18. Not to be confused with LC18 in the 3D model which accounts for the horizontal wind loading. When the element size is increased this inaccuracy increases as well. This is likely caused by the way Diana handles elements and nodal forces.

Because there is a deviation between the top of the pedestal, where the loads are attached in the 3D model, and the point of loading according to the turbine manufacturer (see Figure 4.4) the application of an additional moment is still required. This is has been accounted for by adding the additional load case 'Add extreme moment hor wind'.

LC22 & LC23 are used for comparison to determine the effects of prestressing the anchor cage. LC22 is just a simple moment load without prestressing, and LC23 is the same moment load but in this case the prestressing force is applied.

It must be noted that the horizontal components of the soil- and water pressure were omitted in the model. This was done because due to the fact that they act all around the structure they will not influence the lateral movement of the structure, and the concrete is assumed to be much stiffer so the influence of these loads to the stiffness is negligible. The vertical components are taken into account because they do affect the vertical displacements and the vertical loading of the foundation piles.

6

Results of the linear analyses

Running a linear analysis on a finite element model as described in the previous chapter produces a lot of different results. For the validation of this model the primary results that were studied are the distributed moments and shear forces, the stresses, the displacements and the cross-sectional forces in the supports, which translate to pile reaction forces. In this chapter the 2D model will be compared to the 3D model with identical supports and subsequently the results of the 3D models with different supports will be compared. Additionally the effects of the non-linearity in the foundation piles are looked at, and lastly the effects of applying a prestressing load to the anchor cage are covered. In this chapter two different viewpoints will be used primarily, the side view and the top view. These are defined as shown in Figure 6.1. Figure 6.1a shows the top view of the structure and also the location of the side view. This is shown in Figure 6.1b, for this model it is simply the view in the direction of the y-axis while in reality this would be a cross section of the structure along the x-axis.

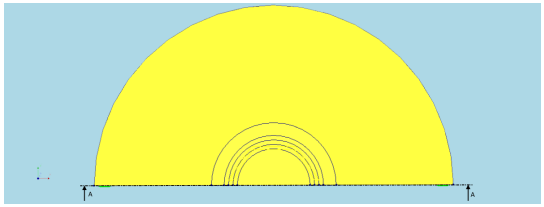

(a) Definition of the "top view" of the foundation structure

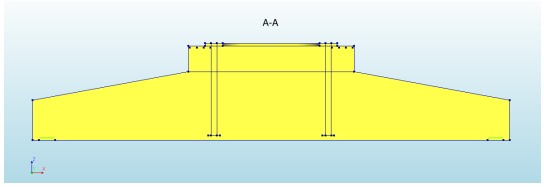

(b) Definition of the "side view" of the foundation structure

Figure 6.1: Definition of the viewpoints to be used

6.1. Comparison between 2D and 3D Models

To determine the validity of the new 3D model a comparison is made to the old 2D model. Both models should produce similar results when subjected to similar loads. Primarily the effects of a simple moment load are compared and in some cases a vertical load as opposed to different load combinations because the simplicity enables an unambiguous and simple comparison of what causes certain effects. As previously described load combination 18 for the 2D model and load combination 7 for the 3D model are the comparable simple moment loads. In Figure 6.2 an example of the deformed model is shown.

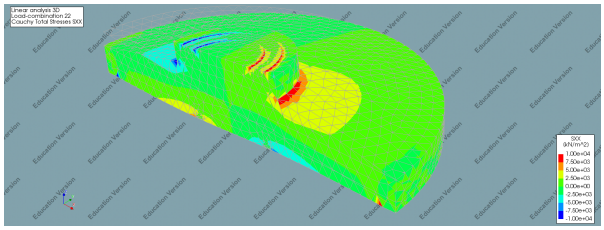

Figure 6.2: Example of a deformed model under moment loading with normal stresses project on it

6.1.1. Distributed moments

A construction subjected to loading will resist deformation and this yields internal distributed forces and moments. In this section the resultant distributed moments in the 3D model will be compared to the ones in the 2D model. Subsequently the differences in results that were obtained from 3D models with different types of supports will be discussed. Before this discussion it is important to establish what definitions were used for the coordinate systems and sign conventions. In Figure 6.3 the generalized moments are shown with the sign convention as used in Diana. This sign convention means that a positive moment yields positive stresses in the upper plane and that a positive shear force yields positive shear stresses. It is important to note that the local element axes have been defined radially around the centre of the structure as shown in Figure 5.16. In general in this chapter subscripts with lower case letters like m_{xx} denote local axes while capital letters refer to global axes as is the case for σ_{XX}.

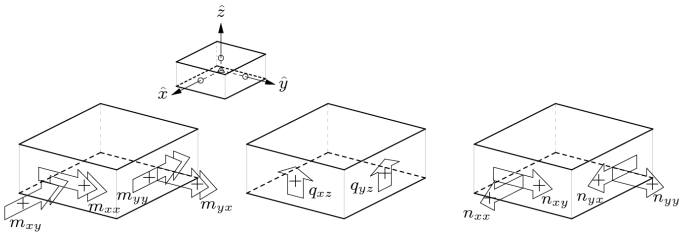

Figure 6.3: Definition of generalized moments and forces[7]

For m_{xx}, which is the distributed moment working in plane on the surface with a normal in positive local x-direction, the results of the 2D and 3D models are shown in Figure 6.4. Figure 6.4a shows the distributed moment calculated by analysis of the 2D model and in Figure 6.4b the distributed moments on the cross-section at mid height in the 3D model results are depicted. For a simple moment load the first thing that can be checked whether the distributed moments are point symmetric along the axis around which the moment is applied. By the previously described definition this x-axis always points to the centre of the structure. Due to irregularities in the mesh this symmetry will not be perfect, but it provides a good first indication. Both situations in Figure 6.4 show this symmetry. The moment distribution looks similar and the corresponding values seem to agree as well. the area over which the moments are distributed appear to be slightly smaller, especially for the higher values.

Different ways of modelling the supports or foundation piles are analysed. The consequent results are compared, and the obtained insights are used for the modelling considerations for the final 3D model.

In Figure 6.5 the distributed m_{xx} is shown for the model in which the horizontal boundary conditions per pile were replaced by a single fixed centre point. It can be seen that this way of modelling yields slightly reduced moments in the composed element surface. Also some sort of discontinuity can be seen at the edge of the pedestal. This is most likely caused by the fact that for the interpolation entire elements are taken into account while they may only be partly located under the pedestal. The next step was to incorporate the fact that the piles may be placed under an angle. The results shown in Figure 6.6 are almost indistinguishable from the ones in Figure 6.5 which is explicable because for this step a central horizontal fixed support was still used and the pile inclination was not large which still yields the same vertical forces and only small horizontal ones. Subsequently the central support was removed and a horizontal stiffness was introduced. The distributed moments are shown in Figure 6.7. The introduction of additional horizontal springs yields small reduction on the left side and a small increase on the right side in m_{xx}. This increase is caused by the additional horizontal forces produced by the springs, corresponding more to reality.

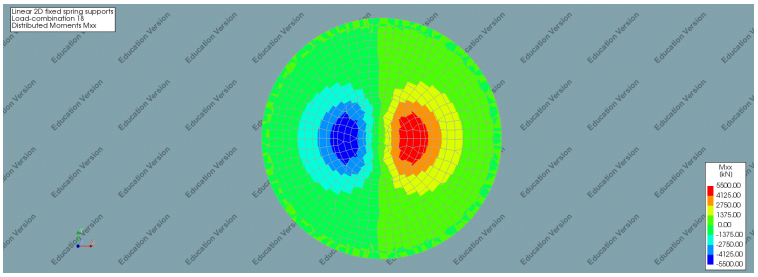

(a) m_{xx} in the 2D plate model load combination 18 (simple moment load)

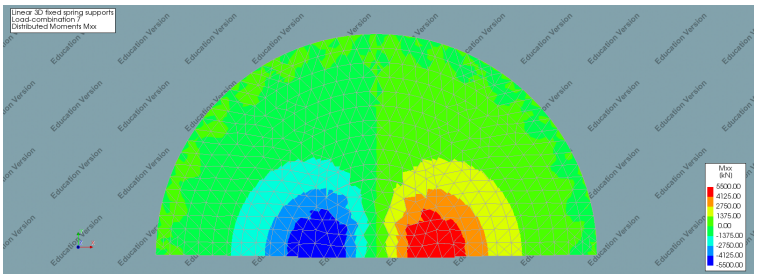

(b) m_{xx} in the 3D solid element model with horizontally fixed vertical springs for supports. load combination 7 (simple moment load)

Figure 6.4: Comparison of m_{xx} for the 2D and the 3D models with horizontally fixed vertical springs for supports. load combination 7 (simple moment load)

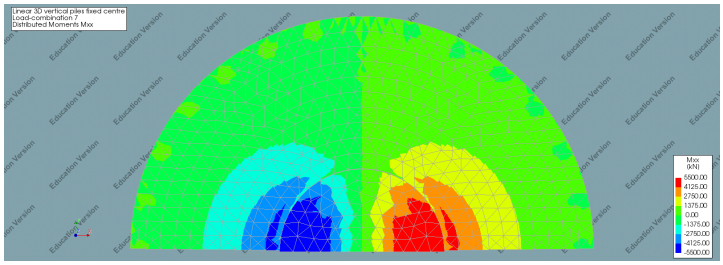

Figure 6.5: m_{xx} 3D with vertical spring supports and supported centre point. load combination 7 (simple moment load)

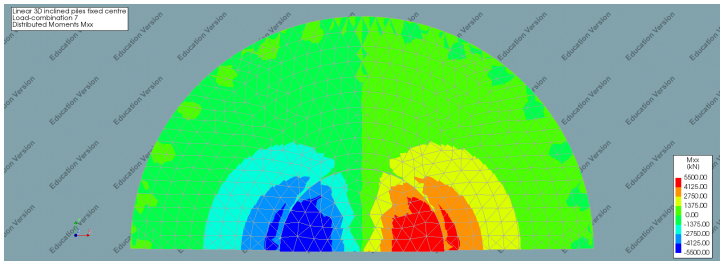

Figure 6.6: m_{xx} 3D with inlinced pile supports and fixed centre point. load combination 7 (simple moment load)

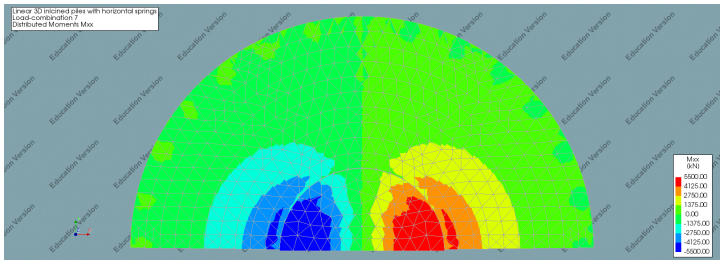

Figure 6.7: m_{xx} 3D with inclined pile supports and horizontal springs. load combination 7 (simple moment load)

In Table 6.1 numerical values are shown for the distributed moments as calculated by Diana. Because the peak values tend to be too high, for the m_{xx} an average of the moments in several elements around the maximum has been determined which yields a slightly lower result. All of the results have been compared to the least and most complex model variants, the 2D and 3D with inclined piles and horizontal soil stiffness models respectively. It is clear that the highest moment found in the 2D model is lower than the ones found in the 3D models.

This can be explained by the fact that the pedestal was not included in the 2D model. The addition of the pedestal yield a structure that is stiffer in the centre leading to higher local moments. Because the total moment remains the same the values outside of the pedestal are expected to be lower, which seems to be the case as the the red are just outside of the pedestal is narrower than in the pedestal itself. This also explains why although the maxima in the 3D models are higher, the distribution of the moments in the visual representation seems reduced compared to the 2D model.

Comparing the different 3D model variants numerically only shows differences of approximately 1%, from which may be concluded that a simpler model can be used to find usable results and to be continued with for the non-linear analysis. These values also shown that the inclusion or omission of the anchor cage and bottom LSP do not influence the linear analysis significantly.

Table 6.1: Numerical values for the distributed moments under simple moment loading

	2D	3D horizontally fixed piles	3D vertical piles with fixed centre	3D inclined piles with fixed centre	3D inclined piles with bedding	3D inclined piles with bedding without anchor cage
m_{xx} [kN]	5158.98	6441.56	6780.66	6406.77	6491.60	6523.99
Deviation with respect to 2D	1.00	1.25	1.31	1.24	1.26	1.26
Deviation with respect to Inclined piles with bedding	0.79	0.99	1.04	0.99	1.00	1.00
m_{xx} max [kN]	5459.00	7002.00	7134.00	7030.00	7125.00	7062.00
Deviation with respect to 2D	1.00	1.28	1.31	1.29	1.31	1.29
Deviation with respect to Inclined piles with bedding	0.77	0.98	1.00	0.99	1.00	0.99
m_{yy} max [kN]	3174.00	4930.00	5076.00	5164.00	5078.00	4664.00
Deviation with respect to 2D	1.00	1.55	1.60	1.63	1.60	1.47
Deviation with respect to Inclined piles with bedding	0.63	0.97	1.00	1.02	1.00	0.92

Because the external moment is applied in the same direction as the internal m_{xx}, it is expected that this will be the most significant and therefore dominant. To check the model this has to be validated. Similarly to m_{xx} the m_{yy} presented in Figure 6.8 appear to be smaller for the 3D model. The difference is somewhat bigger in this case. The m_{yy} is more spread out for the 2D model, and again the reduction around the pedestal can also be seen.

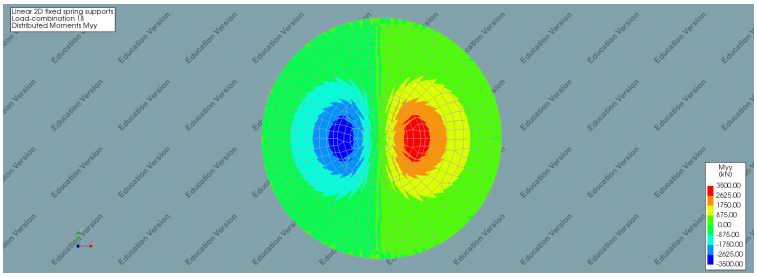

(a) m_{yy} in the 2D plate model under moment loading

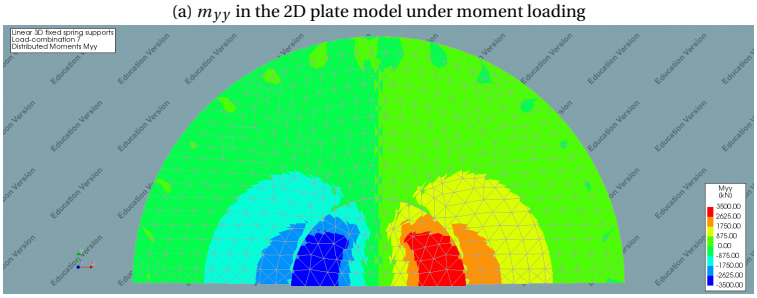

(b) m_{yy} in the 3D solid element model with horizontally fixed vertical springs under moment loading

Figure 6.8: Comparison of m_{yy} under moment loading

While the results for the different types of support did differ for m_{xx}, the results for m_{yy} are more or less identical for all cases. A small difference can be seen for the case with the additional horizontal springs in which the distributed moments are slightly larger. This is presumably caused by the fact that contrary to the other horizontally free support types more significant horizontal reaction forces occur, and as they are located eccentrically in relation to the neutral axis they will produce a moment, albeit rather small.

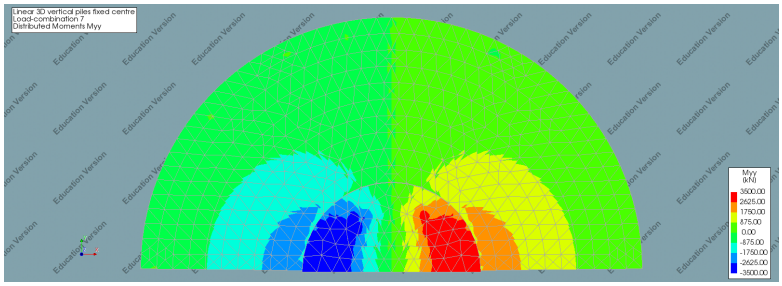

Figure 6.9: m_{yy} 3D with vertical spring supports and fixed centre point. load combination 7 (simple moment load)

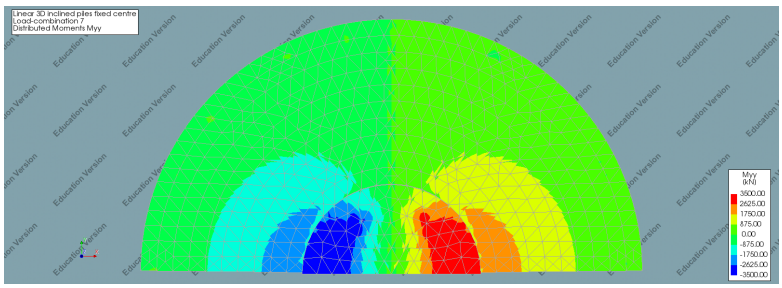

Figure 6.10: m_{yy} 3D with inclined pile supports and fixed centre point. load combination 7 (simple moment load)

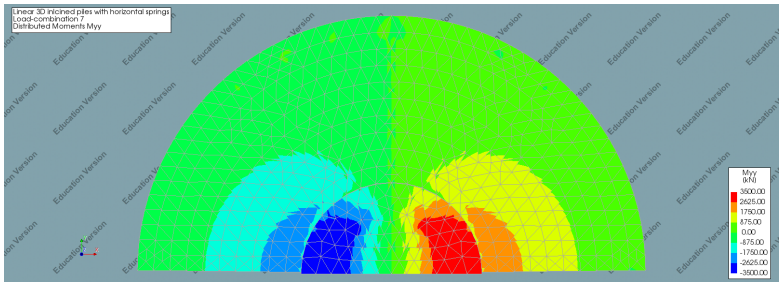

Figure 6.11: m_{yy} 3D with inclined pile supports and horizontal springs. load combination 7 (simple moment load)

6.1.2. Distributed shear forces

The distributed shear forces are important to determine the amount of shear reinforcement required. In Figure 6.12 the distributed shear forces in the plane with the normal in x-direction are compared. The shear forces in Figure 6.12a appear to be lower and less spread out than the ones in Figure 6.12b. The addition of the pedestal leads to lower distributed shear forces in the centre of the structure. The vertical load that needs to be resisted remains the same while the height, and thus the area, over which it is distributed is increased. However, outside of the pedestal the shear forces are higher for the 3D model than they are for the 2D one. This suggests that the for the shear forces the assumptions are not conservative and this may lead to increased reinforcement. The general distribution however is as can be expected resulting from a moment load as they are largest at the cross section over which the moment is applied and fade out towards the edges.

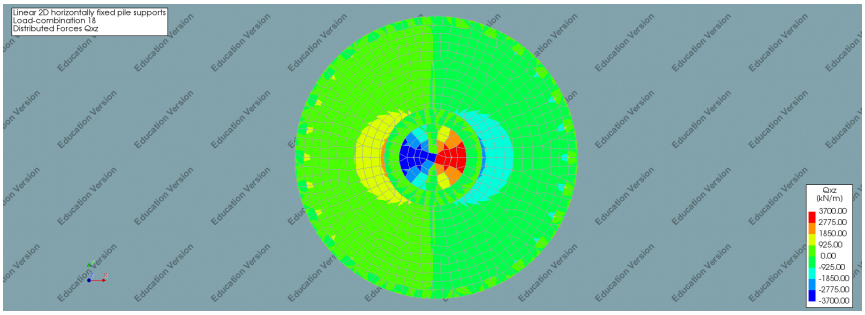

(a) Q_{xz} in the 2D plate model

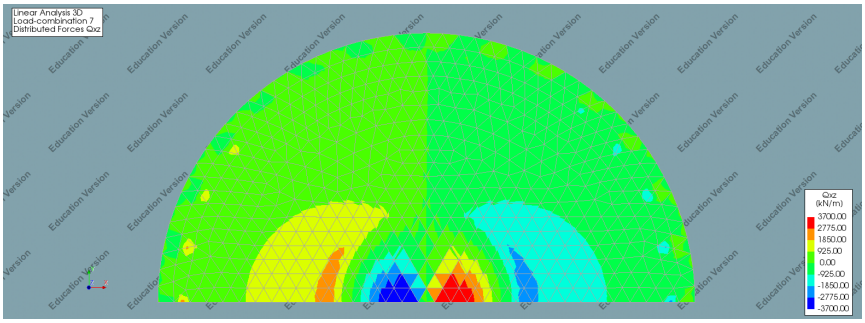

(b) Q_{xz} in the 3D solid element model

Figure 6.12: Comparison of Q_{xz}

6.1.3. Displacements

Displacements caused by the turbine loads in the structure are important because ultimately the purpose of the foundation structure is to prevent displacements of the tower and turbine. Essentially the 'stiffness' of the structure is the relation between exerted loads and displacements. The gradient of the displacement is somewhat steeper for the 2D model. This might be because the addition of the pedestal in the 3D model increases the structural stiffness in the centre of the foundation.

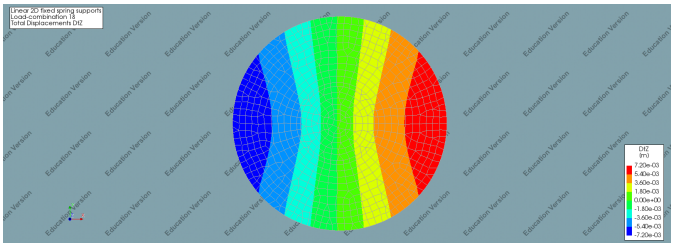

(a) Top view of vertical displacement for LC18 for the 2D model

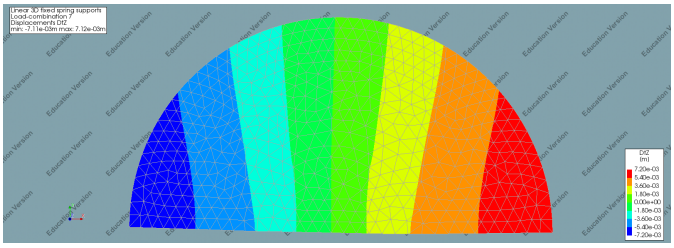

(b) Top view of vertical displacement for LC7 for the 3D model with horizontally fixed vertical piles(the pedestal has been hidden)

Figure 6.13: Comparison of vertical displacement (d_Z) under simple moment loading for the 2D and 3D model

In Figure 6.14 the vertical displacements caused by moment loading for the model with inclined piles and horizontal springs is shown. The displacements for the model with horizontally fixed vertical springs in Figure 6.14a can be compared with the ones for the model with inclined piles and horizontal soil springs in Figure 6.14b to determine the influence of the different supports.

The general distribution remains similar, but the gradient has increased slightly for the model with the inclined piles. This might be attributed to the fact that the vertical pile resistance component for an inclined pile is lower than the total vertical resistance, which is used if the pile is placed vertically. This can also explain the slight increase of maximum displacement.

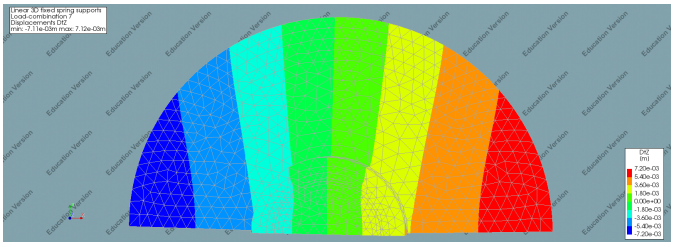

(a) Top view of vertical displacement for LC7 for the 3D model with horizontally fixed vertical piles

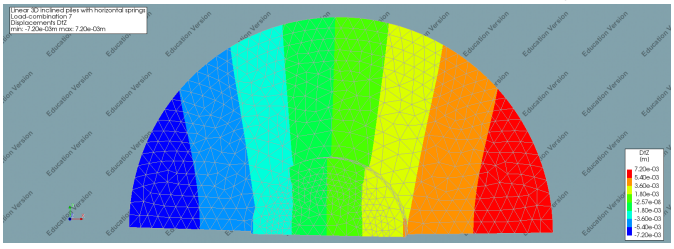

(b) Top view of vertical displacement for LC7 for the 3D model with inclined piles and horizontal springs

Figure 6.14: Comparison of vertical displacement (d_Z) for simple moment loading

6.1.4. Stresses

Because the span between opposite foundation piles and the moment is applied around the y-axis the stresses are assumed to be the largest in the cross section along the centroidal axis in x-direction. In Diana the principal stresses are defined as can be seen in Figure 6.15.

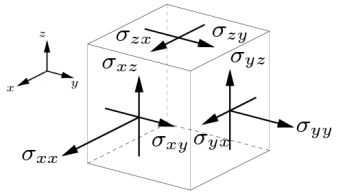

Figure 6.15: Definition of cauchy principal stresses[7]

In Figure 6.16 the stress distributions for different horizontal planes in the foundation are shown. In the top plane, in Figure 6.16a, it can clearly be seen that tension occurs in top right, while it is clear from Figure 6.16c that there are tensile stresses in the bottom left. This means that the tensile stresses are located where the structure elongates and compression occurs oppositely as can be expected. Figure 6.16b shows the neutral cross section in which the stresses in x-direction are approximately zero.

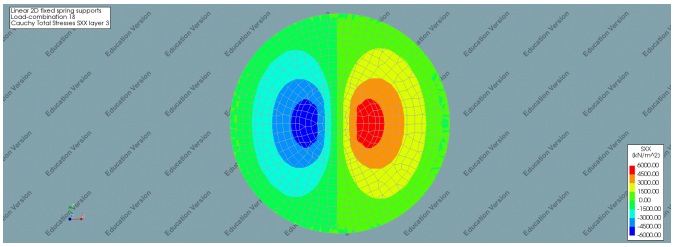

(a) σ_{XX} (global) in top view of the top layer of the 2D model for a simple moment load (LC18)

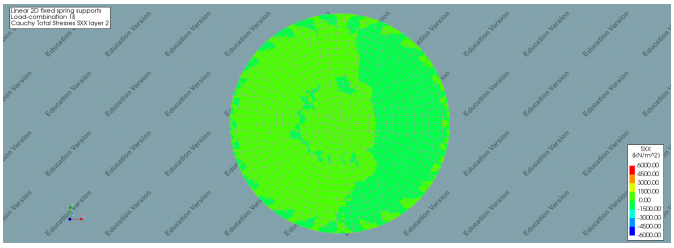

(b) σ_{XX} (global) in top view of the middle layer of the 2D model for a simple moment load (LC18)

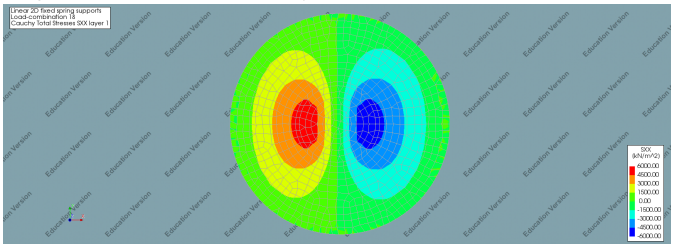

(c) σ_{XX} (global) in top view of the bottom layer of the 2D model for a simple moment load (LC18)

Figure 6.16: Top view of normal stresses in global X-direction at different layers in the 2D model under moment loading with horizontally fixed foundation piles

The stresses shown in Figure 6.16 can be compared to the stresses in the 3D model with horizontally fixed springs shown in Figure 6.17. The stresses are rather similar line where the stresses are zero follows the centre of mass and the tension- and compression zones match as well. The only real differences are caused by the introduction of the pedestal and the two load spreading plates. Especially the bottom LSP, which has a much higher elastic modulus than the surrounding concrete, causes a distortion in the smooth stress distribution. But these discrepancies are exactly as was to be expected.

As was the case before the different types of supports studied can now be compared. In Figure 6.18 the stresses under moment loading are shown for the different ways of modelling piles.

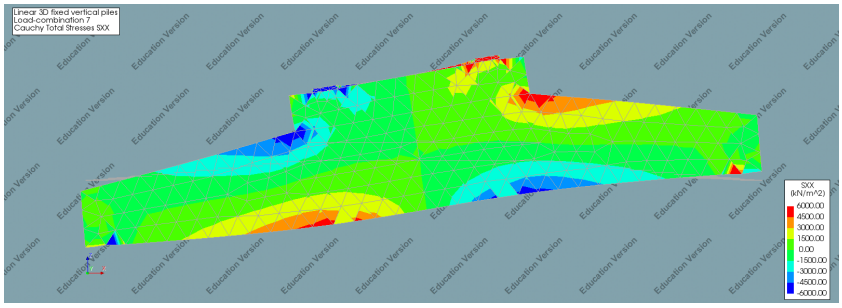

Figure 6.17: Side view of σ_{XX} in the 3D model under moment loading (LC7) with horizontally fixed vertical springs

The biggest deviation is seen in Figure 6.18b, where there are stresses occurring at the fixed central support. These stresses are the result of a horizontal reaction force. The horizontal components of the reaction forces in the inclined piles are in the same direction for piles in both tension and compression. This leads to a resultant horizontal force from the piles which is in equilibrium with the horizontal reaction force in the centre support.

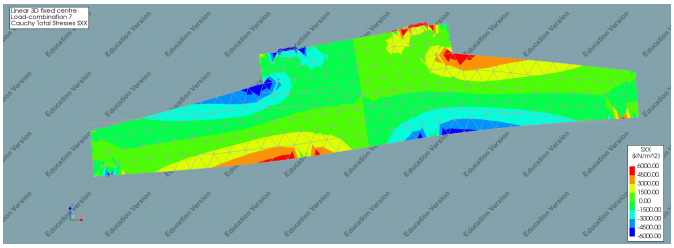

(a) Side view of σ_{XX} with vertical piles and a fixed centre point under simple moment loading (LC7)

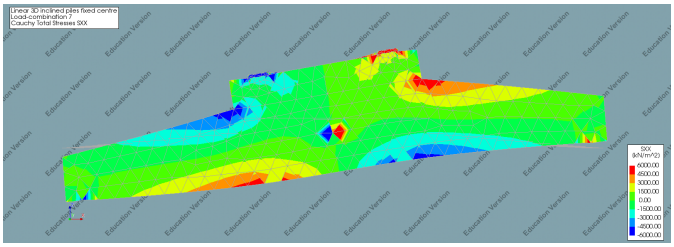

(b) Side view of σ_{XX} with inclined piles and a fixed centre point under simple moment loading (LC7)

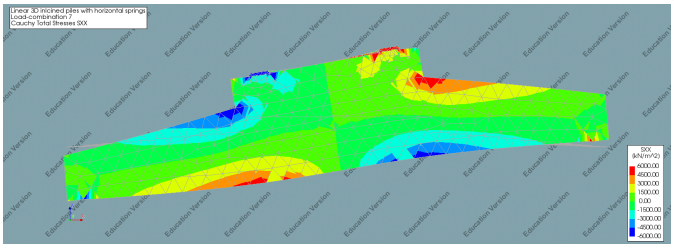

(c) Side view of σ_{XX} with inclined piles and horizontal springs under simple moment loading (LC7)

Figure 6.18: Normal stresses in the centre cross section caused by moment loading side view

Points of interest for the quantitative comparison of tensile stresses are shown in Figure 6.19. In point 1 the stresses in x-direction as a result from vertical loading are taken, at point 2 the stresses caused by moment loading are compared.

In Table 6.2 numerical values for the maxima of normal stress in x-direction for all model variants are given as they were calculated directly for simple vertical- and moment loading. Additionally normal stresses in the elements around the previously described points of interest are averaged and presented. The values in this table are compared to the 2D model and to the most complex one. As far as the maximum values go, the 2D model is almost not comparable to the 3D models. The reason for this is that in the 3D model some irregularities occur that are not present in the 2D model, such as the pedestal, the load spreading plates and

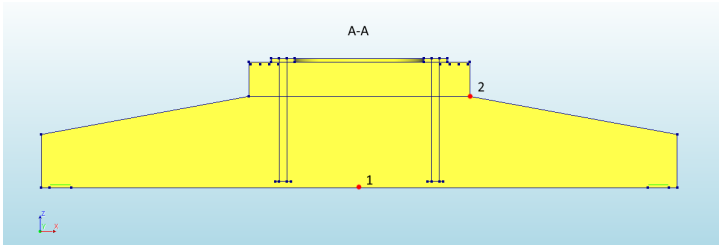

Figure 6.19: Points of interest for tension shown in the side view cross section

Table 6.2: Numerical values for σ_{XX}

		2D	3D horizontally fixed piles	3D vertical piles with fixed centre	3D inclined piles with fixed centre	3D inclined piles with bedding	3D inclined piles with bedding without anchor cage
σ_{XX} due to vertical load [kNm^{-2}]	maximum	989.66	4729.00	995.00	970.00	945.00	906.00
	Relative to inclined piles with bedding	1.05	5.00	1.05	1.03	1.00	0.96
	Averaged in point 1	988.33	330.91	495.78	497.73	496.05	490.98
	Relative to inclined piles with bedding	1.99	0.67	1.00	1.00	1.00	0.99
σ_{XX} due to moment load [kNm^{-2}]	maximum	5838.00	15800.00	15900.00	22400.00	22400.00	23100.00
	Relative to inclined piles with bedding	0.26	0.71	0.71	1.00	1.00	1.03
	maximum without pedestal	-	14700.00	11200.00	13899.00	11300.00	11600.00
	Relative to inclined piles with bedding		1.30	0.99	1.23	1.00	1.03
	Averaged in point 2	5226.02	5804.60	5256.06	5184.38	5132.70	5577.26
	Relative to inclined piles with bedding	1.02	1.13	1.02	1.01	1.00	1.09

the fact that the supports are placed eccentrically. As could be seen in the previous figure there are mostly peak stresses around the LSP. To potentially reduce this effect the maximum stresses outside of the pedestal were also collected. An additional benefit of this that for reinforcement design the pedestal can be seen as a separate entity and therefore both values provide meaningful information. However the maxima outside of the pedestal are still significantly higher than they are in the 2D model, which is presumably a result of the modelling of the supports. The averaged stresses in point 2 are also shown to determine the maximum stress where it can be expected to occur, the stresses found after averaging are a lot closer to the values found with the 2D model which suggests that the current reinforcement design is still valid. The fact that there are high concentrations of stresses at several points in the structure is a point of interest for the non-linear analysis.

Although the values resulting from the vertical loading are significantly lower than the ones as a result from moment loading they still provide a good opportunity for comparing the different models. While the results of the four latter models show no big differences the model with the fixed supports is clearly an outlier for this case. The combination of low average stress in point 1 and a high maximum stress can be explained by the fact that the horizontally fixed supports resist the horizontal displacements at the underside of the structure. This leads to high horizontal normal stresses relative to the other models. This is not seen for the 2D model in which the supports are also horizontally fixed. But for the 2D model the supports are effectively placed at mid-height.

For the structure with a central horizontal support high maximum stresses occur but this is at the support location as can be seen in Figure 6.18b. The fact that this only occurs for the model with inclined piles is because the vertical reaction forces also produce a horizontal component which work in the same direction at both sides of the structure and thus they do not balance each other out. As a result extra stresses occur in the horizontally fixed centre point. To ensure that the inclusion of the anchor cage and bottom LSP does not change the structural behaviour too much to render comparisons with the old 2D model, and the consequent reinforcement design, useless an analysis without these elements present was also compared but it does not seem to have a significant effect in the linear analysis.

In Table 6.3 the maxima and the averaged values in point 2 for σ_{ZZ} are shown. Just like Table 6.2 this table shows that the differences between the latter 4 models are rather insignificant. As was the case for stress concentrations around the LSP for σ_{XX}, a point of concern for the non-linear analysis are the peak values for σ_{ZZ} at the supports, primarily at the piles in which tensile stresses occur.

Table 6.3: Numerical values for σ_{ZZ}

		3D horizontally fixed piles	3D vertical piles with fixed centre	3D inclined piles with fixed centre	3D inclined piles with bedding	3D inclined piles with bedding without anchor cage
σ_{ZZ} due to moment load [kNm^{-2}]	maximum	22600.00	27100.00	28900.00	28900.00	28800.00
	Relative to inclined piles with bedding	0.78	0.94	1.00	1.00	1.00
	Averaged in point 2	5679.38	6088.22	5967.08	6172.65	5894.44
		0.92	0.99	0.97	1.00	0.95

6.1.5. Structural behaviour for combined loading

As mentioned before, simple load cases were compared as these are more comprehensible. But as a reference for the non-linear model combined loading is also important. In Figure 6.20 the vertical displacement is shown and it can be seen that the neutral axis, in the green area, has moved slightly to the right. Moreover it goes without saying that this neutral axis is no longer at 0 but slightly lower due to the effect of the vertical loads.

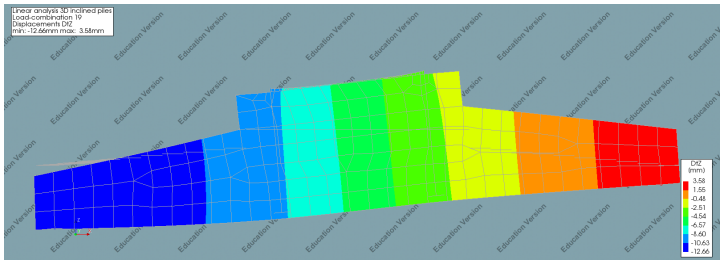

Figure 6.20: Side view of vertical displacement for inclined piles and horizontal springs under combined ULS loading (LC19)

In Figure 6.21 it can be seen that the combined loading results in somewhat reduced symmetry. The concentration of the stresses moves to the left side of the structure. Although this is fairly logical it is an important observation as it means that the maximum stresses will be higher due to the influence of the vertical loading, and the bottom left increases in importance concerning potential tensile failure and reinforcement yielding. It must be noted that although the focus is on one point or area, this can occur anywhere at the same distance from the centre of the construction as the wind can come from any direction. Therefore the reinforcement design must be approached in an axi-symmetric manner.

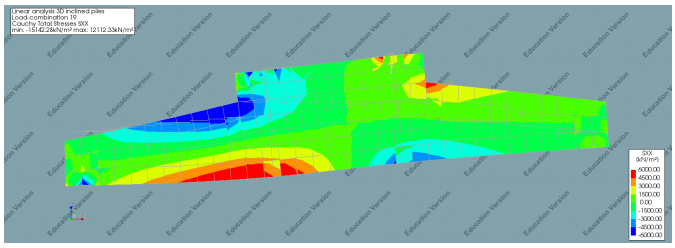

(a) Side view of σ_{XX} with inclined piles and horizontal springs under combined ULS loading (LC19)

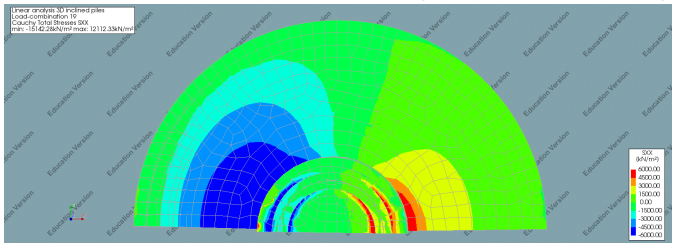

(b) Top view of σ_{XX} with inclined piles and horizontal springs under combined ULS loading (LC19)

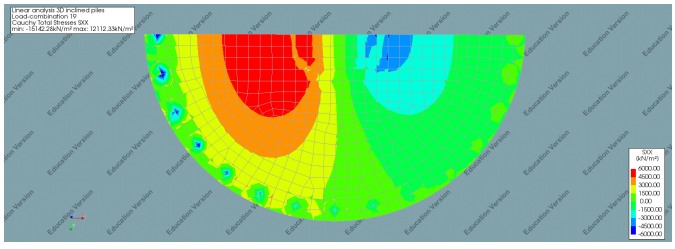

(c) Bottom view of σ_{XX} with inclined piles and horizontal springs under combined ULS loading (LC19)

Figure 6.21: Normal stresses under combined ULS loading

6.2. Pile loads

Reaction forces in the springs can be found. To determine the effects of the different ways of modelling they need to be compared side by side. This has been done for the vertical turbine load (purely vertical) and the (simple) moment load. The pile forces in Figure 6.22a do not seem to differ significantly and not in a constant manner either. This is most likely caused by small mesh irregularities. Only the 2D model seems to have a discernible pattern, namely increasing pile loads for piles closer to the centre in the x-axis. In Figure 6.22b the different components of forces the inclined piles exert on the structure are shown to illustrate how much of horizontal effect can be expected.

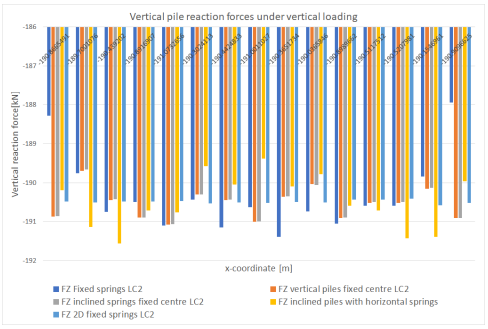

(a) Vertical pile reaction forces due to vertical loading only for all different types of supports

(b) Components of the reaction forces due to vertical loading only for inclined piles

Figure 6.22: Pile reaction forces under vertical loading

In Figure 6.23a it is clear that the forces in the 2D model are higher, but this is most likely caused by the fact that the piles are modelled closer to the centre, as previously described, leading to higher forces to generate the required resisting moment. The variant with inclined piles also shows slightly higher values. This can be explained by the fact that the additional moment caused by the reaction force in the centre needs to be resisted as well, leading to somewhat raised pile forces.

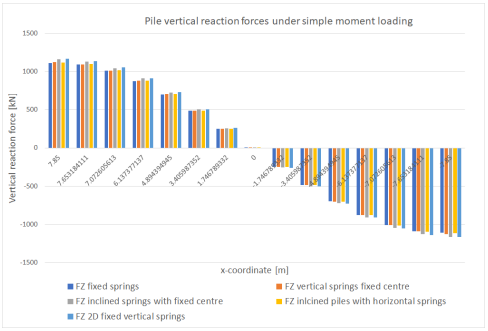

(a) Vertical pile reaction forces due to moment loading only for all different types of supports

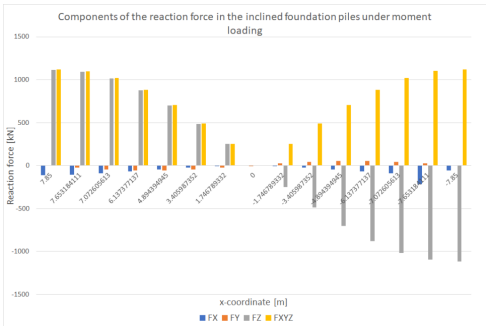

(b) Components of the reaction forces due to moment loading only for inclined piles

Figure 6.23: Pile reaction forces under moment loading

In previous result descriptions it could be seen that the effects of the inclined piles were not very large. This is supported by Figure 6.23b where it can be seen that the reaction forces other than the vertical one are relatively small.

6.2.1. linear springs vs. non-linear springs

In Figure 6.24 the reaction forces and displacements are shown for all foundation piles numbered from right to left along the x-axis, as shown in Figure 6.24a, for a non-linear analysis that only incorporates multi-linear piles as non-linear elements.

In Figure 6.24b it can clearly be seen that the reaction force in the right pile, which is in tension, is capped at a load factor of 1.5 with the second tensile pile following suite, meaning that the maximum tensile force is reached in these piles, meaning they are pulled out of the ground.

Because the failure load in compression is much higher this doesn't happen yet for the left pile.

It can be seen that the gradient for the compressive piles only increases slightly after the maximum tensile strength is being reached in the compression piles at a load factor of 1.5, but once the first piles on the left start reaching their limit as well the increase becomes significant.

Pile 10 is the last pile to reach its maximum compressive capacity at a load factor of little under 2.5.

While the displacement in all the piles, shown in Figure 6.24c, is almost linear from the start they all start to increase almost exponentially after the first tension pile reaches its tensile capacity.

At a load factor of 2.5 all piles reach an almost 0 slope suggesting maximum capacity of the entire structure, which correlates to the last pile reaching maximum compression as seen in Figure 6.24b.

It is clear that when the first tensile piles reach their maximum capacity the loads are redistributed to the other piles, and the compressive piles contribute more to the resistance of the structure.

Note that these figures have been made for ULS loading, meaning that there is an applied load factor of 1.1 already included in the results.

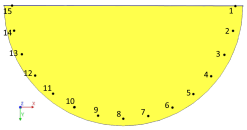

(a) Underside view of the foundation with numbered piles for reference

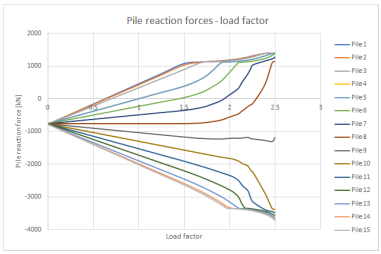

(b) Reaction forces in the piles numbered from left to right along the x-axis for non-linear piles under simple moment loading

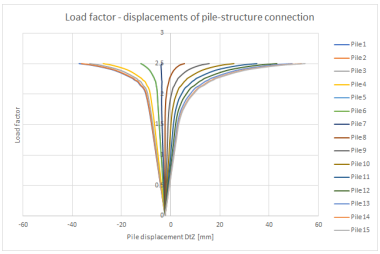

(c) Displacements in the piles numbered from left to right along the x-axis for non-linear piles under simple moment loading

Figure 6.24: Pile reaction forces under moment loading

The graphs in Figure 6.24 are visually supported by Figure 6.25.

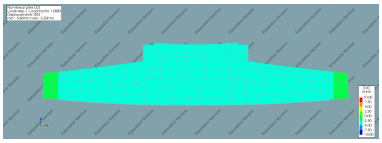

(a) Side view of the displacement for non-linear foundation piles under vertical loading. Load factor 1.0 on self weight and vertical turbine load)

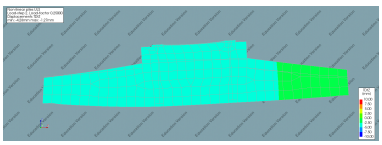

(b) Unscaled Side view of the displacement for non-linear foundation piles under moment loading. Load factor 0.25

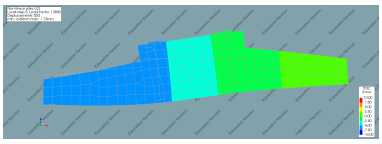

(c) Side view of the displacement for non-linear foundation piles under moment loading. Load factor 1.0

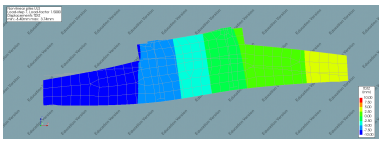

(d) Side view of the displacement for non-linear foundation piles under moment loading. Load factor 1.50

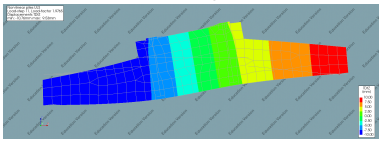

(e) Side view of the displacement for non-linear foundation piles under simple moment loading. Load factor 1.977

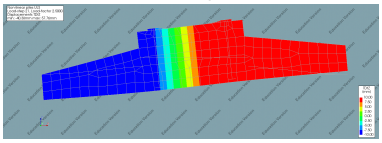

(f) Side view of the displacement for non-linear foundation piles under moment loading. Load factor 2.5

Figure 6.25: Pile reaction forces under moment loading

In Figure 6.26 it can be seen that the redistribution of forces in the piles does not cause significant alterations in the stress distribution. Figure 6.26a shows a comparable stress distribution to the one shown

in Figure 6.21a for ULS loading, and although the maximum stress values are higher as a result of increased loading at load factor 2.5 the overall shape of the stress distribution is still similar in Figure 6.26.

(a) Side view of normal stress σ_{XX} for non-linear foundation piles under moment loading and initial vertical loading. Load factor 1.0

(b) Side view of normal stress σ_{XX} for non-linear foundation piles under moment loading and initial vertical loading. Load factor 2.5

Figure 6.26: Pile reaction forces under moment loading

6.3. Influence of prestressing the anchor cage

In Figure 6.27 the different stress components caused by a prestressing load of 570kN per anchor bolt. Logically the effect is very visible in vertical direction in Figure 6.27c, but also in x-direction as shown in Figure 6.27a. The corresponding displacements are shown in Figure 6.28.

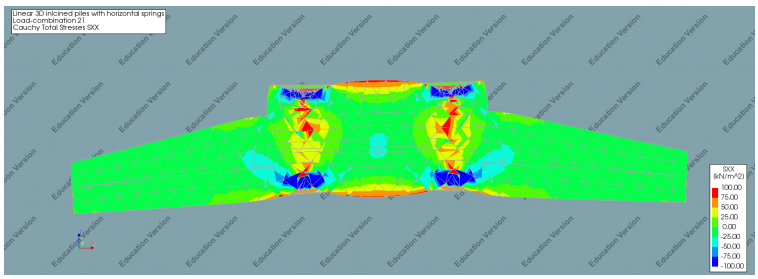

(a) Side view of σ_{XX} caused by prestressing load only

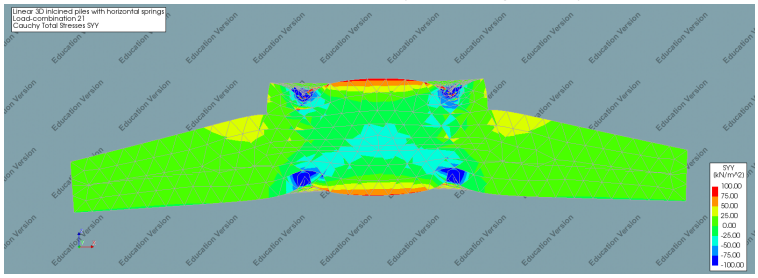

(b) Side view of σ_{YY} caused by prestressing load only

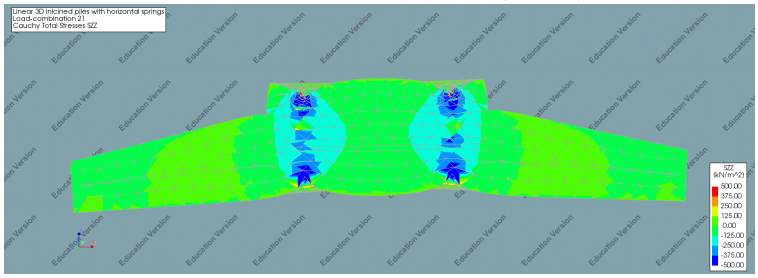

(c) Side view of σ_{ZZ} caused by prestressing load only

Figure 6.27: Different stress components caused by prestressing on the deformed structure

Although the effects on the stresses can be seen, the actual effect for the deformation, shown in Figure 6.29 is negligible. Figure 6.29a in which the deformations without prestressing are shown and Figure 6.29b where the prestressing load is included are almost identical. This follows from the fact that the displacements caused exclusively by the prestressing load are of a smaller magnitude than the displacements resulting from the moment load. But it also means that the prestressing load does not lead to a significant increase in structural stiffness in a linear analysis.

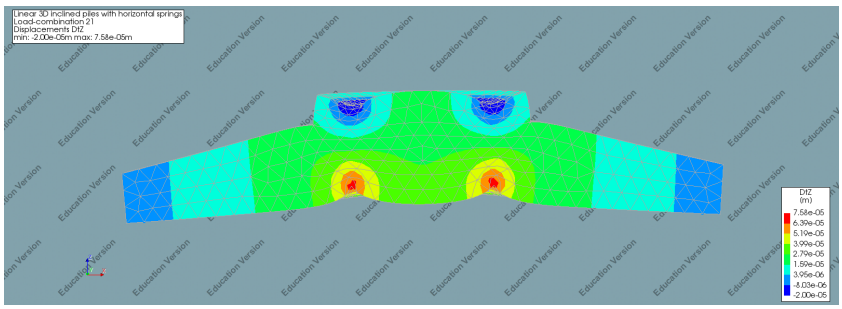

Figure 6.28: Vertical displacement only due to prestressing of the anchor cage

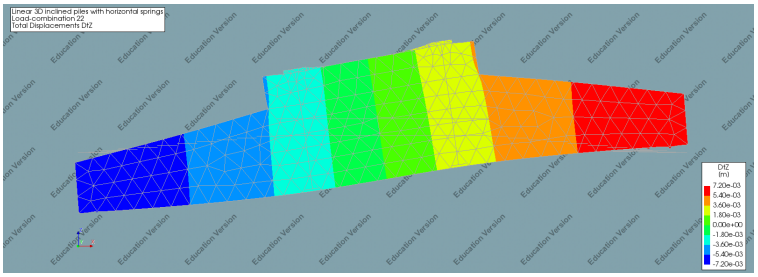

(a) Vertical displacement due to moment loading without prestressing of the anchor cage

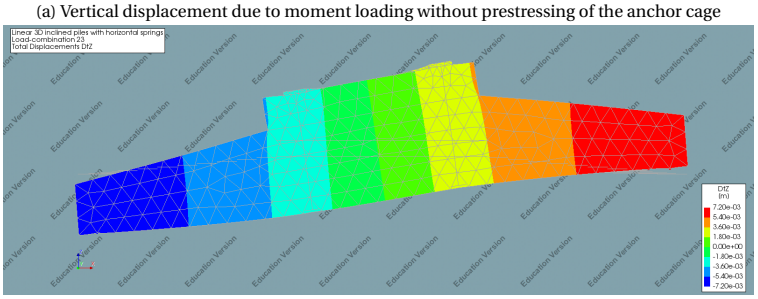

(b) Vertical displacement due to moment loading with prestressing of the anchor cage

Figure 6.29: Comparison of vertical displacement d_Z with and without prestressing of the anchor cage

7

Model for non-linear analysis

After the linear analyses the results and findings from those analyses can be used to further develop the model into one suited for non-linear analyses. Apart from the obvious additions to material properties several modifications have to be made to be able to handle the increased complexity.

7.1. Modifications of the model geometry

There are some aspects of the linear model that, with the results from the linear analyses in mind, require reconsideration due to possible problems in non linear analysis.

7.1.1. Foundation piles

The foundation pile springs were the cause of high stresses, which is a likely cause of divergence in a non linear analysis. To avoid this the connections between the foundation structure and the piles was modelled as circular plates with a structural interface connection. Including an inclination for the pilesis rather complex when they are modelled as such, but the effects of this have been shown to be small in the linear analyses. For the spring interface properties the previously used horizontal and vertical pile stiffnesses, of 170MN m^{-1} and 19.3MN m^{-1} respectively, were divided by the pile cross-sectional area. In practice this had to be achieved by defining interface tractions corresponding to relative interface displacements. The correlation between relative displacements and tractions is shown in Figure 7.1. The relative displacement depends on what surface the interface is defined and which it connects to. In the case for the piles it is defined on the pile and connected to the bottom surface of the construction. In the output this leads to slightly different results than would be the case for stresses as in this case the positive interface tractions are directed upwards and the negative ones downwards, while an upward reaction load in the foundation pile would yield compression in the pile which would be denoted as negative when considering stresses.

(a) Definition of positive interface relative displacements

(b) Definition of positive interface tractions

Figure 7.1: Relation between positive tractions and relative displacement in interfaces[7]

The tractions corresponding to the relative displacements are found by taking the values from the load-displacement diagram in chapter 5 and dividing them over the cross-sectional area of the foundation piles. The resulting diagram is shown in Figure 7.2.

As opposed to the modified stiffness for edge piles with the spring supports this method does not require special treatment of the piles at the edge. These plates were fixed in all directions. A view of the underside of the structure with these piles is shown in Figure 7.3.

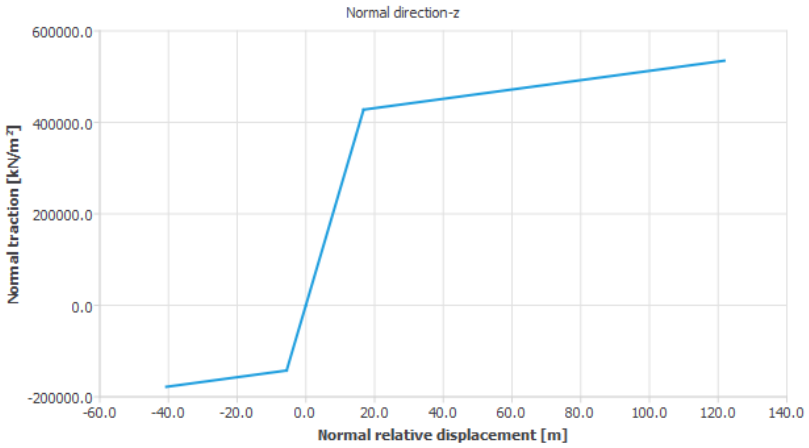

Figure 7.2: Relative displacement-traction diagram for the boundary interface used for the foundation piles

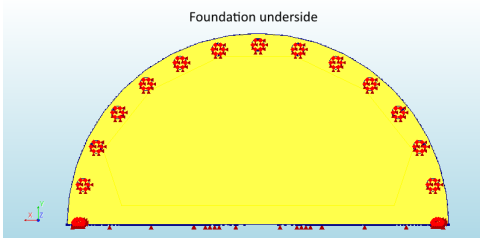

Figure 7.3: The underside of the structure with the piles modelled as circular sheets with a spring interface

Additionally the mesh of the circular piles was reduced to decrease deviant stress concentrations as well as illustrated in Figure 7.4.

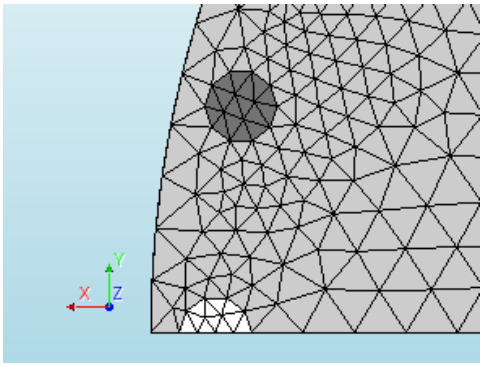

Figure 7.4: A more detailed view of the mesh refinement around the foundation piles as seen from the underside of the structure

When the piles are only modelled as flat shells connected directly to the bottom of the structure, albeit via structural interfaces, the reinforcement that would connect the piles to the the foundation structure in practice can't continue into what would be the piles. This leads to the piles tearing from the bottom of the structure when the interface tractions reach the concrete tensile strength. Because in reality the reinforcement between the foundation and the piles is continuous this is a failure mode that is not actually expected. To avoid this the top of the piles is modelled and connected to the bottom of the structure, after which the pile interface was connected to the bottom of these model elements as shown in **??**. Linear concrete properties were assigned to these pile head elements as to avoid the previously described tearing effect.

To model the interfaces CT36I elements were used supplemented with CQ48I elements for analyses in which square elements were used. These element types are shown schematically in Figure 7.5 and Figure 7.6 respectively.

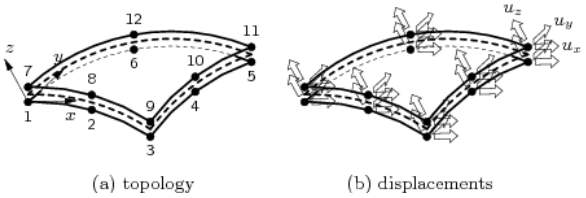

(a) topology (b) displacements

Figure 7.5: Topology and displacements of a CT36I element which is an interface element between two planes in a three-dimensional configuration[7]

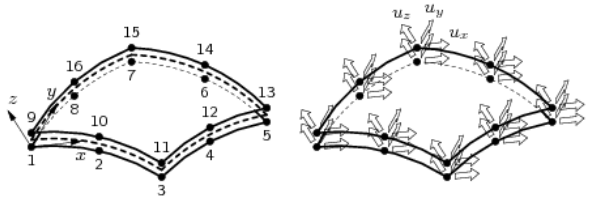

(a) topology (b) displacements

Figure 7.6: Topology and displacements of a CQ48I element which is an interface element between two planes in a three-dimensional configuration[7]

Bottom LSP interface
In addition to an interface for the top LSP another interface is applied at the bottom LSP. Without such an interface tensile stresses would arise in the concrete under the LSP when the prestressing load is introduced, and above it when a high enough moment load is applied. This can result in erroneous cracking in the underside of the structure. For the bottom no tension interfaces were applied to the areas of the concrete under the bottom LSP. This will reduce the tensile stresses in the underside although due to the reinforcement tension is not eliminated altogether.

7.2. Reinforcement design

For the foundation structure a multitude of types and locations of reinforcement were used to withstand the tensile stresses and shear forces caused by the turbine loading.

- radial rebar (top, bottom and in the pedestal);
- tangential rebar (top, bottom and in the pedestal);
- orthogonal meshed (top, bottom and in the pedestal);
- splitting rebar (top and bottom);
- shear rebar;
- suspension rebar.

In Figure 7.7 an overview of all the reinforcement combined is shown. To make this somewhat less complex in Figure 7.8 the different reinforcement sets are shown in three separate figures. Figure 7.9 shows a cross-section in which all relevant dimensions and the set names are included.

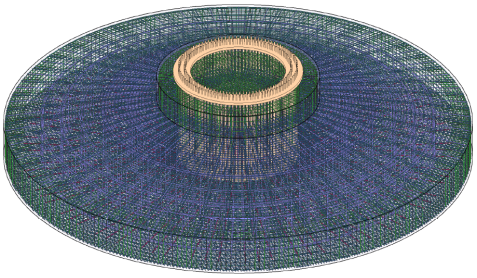

Figure 7.7: Overview of all reinforcement in the foundation structure

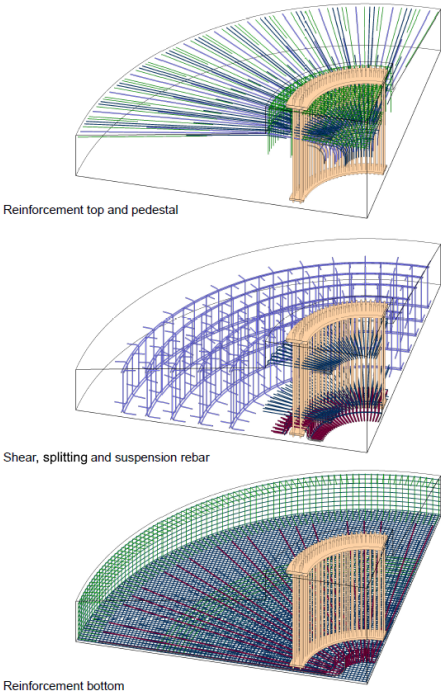

Figure 7.8: Overview of the reinforcement split up into several groups

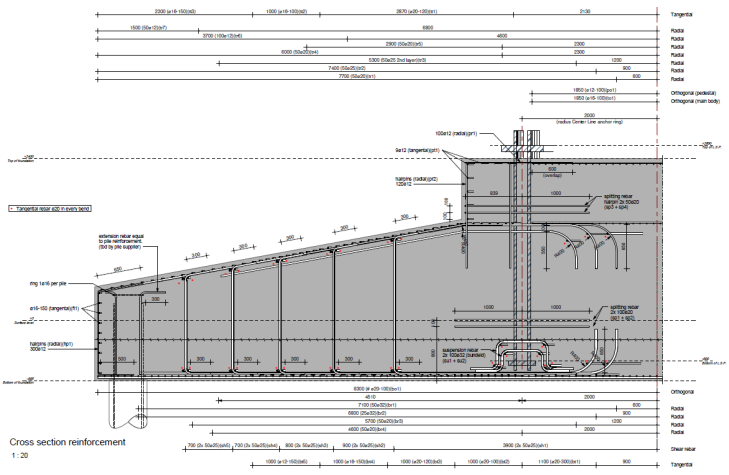

Figure 7.9: Cross section showing the reinforcement including all the reinforcement set names

7.2.1. Reinforcement in the model

The different types of rebar are defined by the following parameters.

- layer position;
- bar diameter;
- centre to centre distance;
- amount;
- start radius;
- end radius;
- bar length;
- bend radius;
- diameter bar.

Not all parameters are necessary for all types of reinforcement. For instance the tangential reinforcement groups do not require an amount as this is based on the start and end diameter in combination with the centre-to-centre distance. In turn the radial reinforcement groups do not require the centre-to-centre distance to be defined as their placement is based on the amount of bars that have to be distributed over 360 degrees in the structure (this would also be complicated as the c.t.c. distance varies over the distance from the centre of the foundation). To slightly simplify the model the bend radii were omitted in this model.

All the types of reinforcement that were used in the reference project were incorporated in the model. Some of these types of reinforcement can be assumed not to have a significant impact in advance, but as this model will be used to study the possible reduction of reinforcement they were all modelled. It must be noted that not all reinforcement is used for acquiring the bending moment resistance that is the primary target of this study.

The orthogonal web reinforcement in the bottom of the structure and in the top of the pedestal were not modelled as discrete embedded bar elements, but as circular sheets with corresponding reinforcement grid properties. For such a grid the bar diameters in both x- and y-directions are required and their respective c.t.c. distances.

7.2.2. Reinforcement model simplification

Although determining all the bend radii usually is an important aspect of the reinforcement design. In reality minimal bending radii are required because the rebar may crack if they are bent to sharply. Additionally some stress concentrations may arise which could be problematic for fatigue loading. However because fatigue is not in the scope of this research and the quality of the rebar elements is not influenced by the bending process used in practice, in this model the bend radii have been omitted. Including the bend radii in the model would require mesh refinement and increase of reinforcement seeding.

7.2.3. Reinforcement geometrical model

In Figure 7.10 the geometrical reinforcement model is shown in its entirety. The orthogonal reinforcement, which are modelled using circular sheets with grid geometries are clearly visible. Because the all the reinforcement together in the isometric view is somewhat unclear, Figure 7.11 shows the reinforcement model as seen from the cross section along the x-axis. This clearly shows the vertically placed shear reinforcement and the suspension rebar around the bottom LSP. To clarify the placement of the radial and orthogonal reinforcement in Figure 7.12 a top view of the reinforcement is shown. For clarity the orthogonal grids located at the bottom and in the top of the pedestal have been hidden.

7.2.4. Reinforcement steel constitutive model

There are 2 general methods of modelling reinforcement in Diana: bonded or bond-slip reinforcement. For the first type the reinforcements are embedded in the structural elements, and have no degrees of freedom of their own. In practice this means that perfect bond is assumed. The second type is somewhat more complex and models the reinforcements as trusses or beam elements internally and connects them to the structural

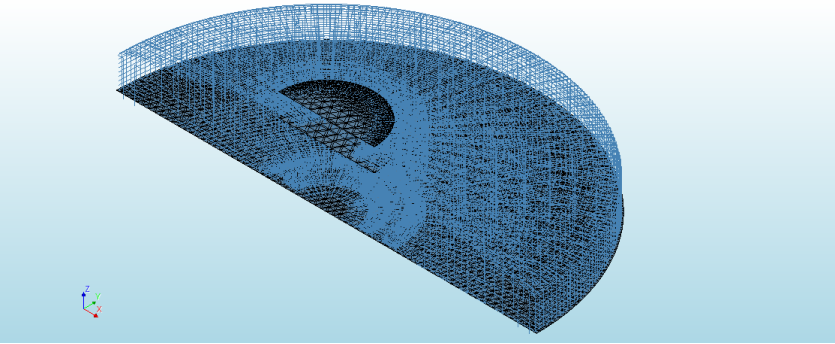

Figure 7.10: Isometric view of the meshed reinforcement model used in this analysis

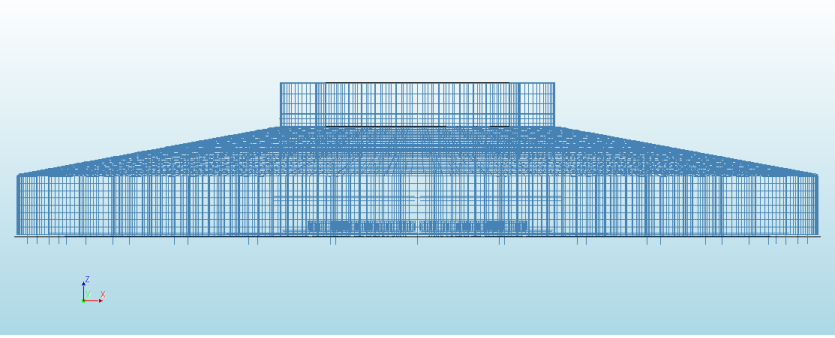

Figure 7.11: View along the centroidal x-axis cross section of the meshed reinforcement model

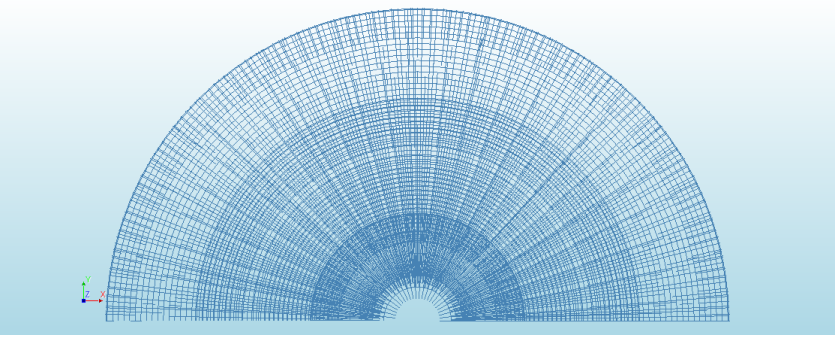

Figure 7.12: Top view of the meshed reinforcement model in which the orthogonal grid reinforcement has been hidden

mother elements via line-solid interfaces. This enables non-linear bond-slip behaviour to be modelled. Due to the size of the model and the prediction of a distributed crack pattern it is expected that the interaction between the concrete mother elements and the reinforcements will remain close to linear and thus the use of embedded reinforcement elements will suffice, and using a more complicated bond-slip model is currently unnecessary.

There are several different integrated reinforcement steel models available in Diana. Many of these were specially developed for cyclic loading. As the fatigue loading has been transformed to a modified static load it is not necessary to use these models. A simpler model using von Mises plasticity can be used. As advised in the RWS guideline[8] an elasto-plastic material model with post-yield hardening as shown in Figure 7.13 is used.

Within the elasto-plastic steel model the type of hardening should be chosen. For this model isotropic hardening was used. meaning that the yield surface of the bi-axial stress-strain relation becomes larger once the initial yield surface is exceeded, while its centre point remains fixed. As opposed to kinematic hardening where the surface size prevails while the centre point shifts. Diana offers the possibility to use isotropic hardening or a combination of both. Because cyclic loading is not in the scope of this project, this exact

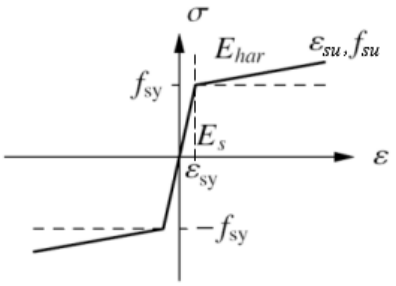

Figure 7.13: Stress-strain diagram for reinforcement steel with post-yield hardening behaviour

behaviour is not very important. The hardening part in the stress-strain relation does however yield a more stable analysis.

7.2.5. Reinforcement steel material properties

The material properties used for reinforcement in this project can be found in Table 7.1

Table 7.1: Reinforcement material properties

Parameter	Value	Unit
f_{sy}	500	MPa
f_{su}	630	MPa
ϵ_{sy}	0.0025	MPa
ϵ_{su}	0.075	MPa
E_s	200	MPa

7.3. Limit state verification

The fib[2] has proposed three methods for ultimate limit state verification. These are the global resistance factor method(GRF), the partial safety factor method(PF) and the estimation of coefficient of variation resistance method(ECOV). The latter two have drawbacks for the intended purpose of the model. The PF uses low strength parameters which may cause deviations in structural response, and thus show a different failure mode than would realistically be the case. The ECOV method always requires two non-linear finite element analyses, which would be cumbersome for application in different projects. Although in development of the model analyses will be done with different parameters according to the GRF- and PF methods for validation, the primary focus will be on the parameters corresponding to the GRF method.

7.3.1. Global Resistance Factor Method

The GRF method is based on the assumption that the global resistance of a structure can be described by using a single global safety factor. In this method relatively high values for material strengths, $f_{cm,GRF}$ and $f_{ym,GRF}$, are used as found from the characteristic values by Equation 7.1 and Equation 7.2. Therefore the final result needs to be corrected by the global safety factor γ_{GL}, determined in Equation 7.3, that accounts for a the model uncertainties.

$$f_{cm,GRF} = 0.85 f_{ck} \tag{7.1}$$

$$f_{ym,GRF} = 1.1 f_{yk} \tag{7.2}$$

$$\gamma_{GL} = 1.2 \times 1.06 = 1.27 \tag{7.3}$$

The advantage of using relatively high "mean" material strength properties is that it will likely give a better approximation of failure modes compared to the lower values used in the partial safety factor method which may show yielding where it would not occur in reality. However to ensure safety the design resistance R_d is

taken as the design value of the ultimate load, P_d, calculated with Equation 7.4 where P_u is the ultimate load obtained from the analysis by inputting "mean" mechanical properties.

$$R_d = P_d = \frac{P_u}{\gamma_{GL}} \tag{7.4}$$

7.3.2. Serviceability limit state

Besides ULS verification the serviceability limit state(SLS) must be checked to determine whether the construction will remain functional for its intended use and be able to stand routine loading. For verification of the SLS the Eurocode dictates post-analysis checks of:

- stress state control
- crack opening control
- deflection control

These three points can be translated to straight forward demands:

Stress state control for a wind turbine foundation implies that the reinforcement may not yield as this is critical for fatigue loading. Crack opening is limited to 0.20mm as determined in relation with the environmental conditions to reduce corrosion damage. Lastly deflection is limited by the maximum allowable inclination of the tower, which has been determined to be 12.5mm m^{-1} by the manufacturer in the reference project. The verification of the SLS is done for an analysis in which unfactored values are used for material strength. Additionally the operational load without a load factor is used.

7.4. Model parameters

For the non-linear analysis several additional or altered model parameters are required.

7.4.1. Mesh size

If a mesh is used that is too coarse the stress field will show considerable jumps[8]. Therefore a maximum element size is advised. For a slab structure this is the lowest value of $\frac{l}{50}$, $\frac{b}{50}$, or $\frac{h}{6}$. In the case of the reference project which has a diameter of 16.7m this yield a maximum element size of $\frac{16.7}{50} = 0.334$m.

The equivalent length or crack bandwidth was determined automatically by method Rots, based on element size, because in general the mesh is quite regular. According to this method the crack bandwidth is found with: $h_{eq} = V^{1/3}$, where V is the volume of the element, which yields $h_{eq} = h$ for cubic hexahedra elements.

Setting the crack band with h a priori is less trivial in case of non-square elements, therefore the use of hexahedra elements as opposed to the tetrahedra used for the linear analysis was studied. However this resulted in a significant amount of elements with very acute or obtuse angles which can lead to instability in a non-linear analysis. Additionally the use of triangular and tetrahedra elements also generated a more regular mesh and therefore, although comparison of results of analyses done with either element type showed no significant differences, primarily tetrahedra meshing was used as default.

To determine mesh size dependency, analyses with the default element size multiplied by 0.8 and 1.2 were run. This did not yield significant differences in results.

7.4.2. Constitutive model for concrete in compression

Choosing the right constitutive model for the non-linear analysis is of utmost importance. A total strain based crack model would be logical to use. A guideline by the Dutch ministry of infrastructure and environment (Rijkswaterstaat) [8] was used as a starting point.

For validation primarily the general resistance factor method(GRF) is used as explained previously. Both the mean measured and GRF material properties are calculated and collected in Table 7.2.

In the reference project a minimal concrete quality of C30/37 was prescribed. Corresponding model properties can be derived from the provisions of the fib Model Code 2010. According to the model code the relations in Figure 7.14 can be used to determine the material properties of concrete required for a non linear analysis based on the characteristic compressive strength as defined by specifying a minimal concrete class.

	f_c [MPa]	f_{ct} [MPa]	E_c [MPa]	v	$G_F\left[\frac{Nmm}{mm^2}\right]$	$G_c\left[\frac{Nmm}{mm^2}\right]$
Mean measured	$f_{cm}=f_{ck}+\Delta f$	* $f_{ctm}=0.3(f_{ck})^{2/3}$ concrete grades ≤C50 $f_{ctm}=2.12\ln(1+0.1(f_{ck}+\Delta f))$ concrete grades > C50	* $E_{ci}=E_{c0}\left(\frac{f_{cm}}{10}\right)^{1/3}$ $E_{c0}=21500MPa$	variable	$G_F=0.073f_{cm}^{0.18}$	$G_c=250G_F$
Characteristic	$f_{ck}=f_{cm}-\Delta f$	$f_{ck,min}=0.7f_{ctm}$	$E_{ci}=E_{c0}\left(\frac{f_{ck}}{10}\right)^{1/3}$		$G_F=0.073f_{ck}^{0.18}$	
Mean GRF	$f_{cm,GRF}=0.85f_{ck}$	$f_{ctm,GRF}=0.3(f_{cm,GRF})^{2/3}$ concrete grades ≤C50 $f_{ctm}=2.12\ln(1+0.1(f_{cm,GRF}))$ concrete grades >C50	$E_{ci}=E_{c0}\left(\frac{f_{cm,GRF}}{10}\right)^{1/3}$		$G_F=0.073f_{cm,GRF}^{0.18}$	
Design	$f_{cd}=f_{ck}/\gamma_c$	$f_{ctd}=f_{ck,min}/\gamma_c$	$E_{ci}=E_{c0}\left(\frac{f_{cd}}{10}\right)^{1/3}$		$G_F=0.073f_{cd}^{0.18}$	

Figure 7.14: relations for the material properties of concrete to be used for different types of analyses

Table 7.2: Material properties

Parameter	Value	Value,GRF	Unit
f_{ck}	30	30	MPa
f_{cm}	38	25.5	MPa
f_{ctm}	2.90	2.60	MPa
E_c	33551	26373	MPa
G_F	0.1405	0.1308	Nmm/mm^2
G_C	35.13	32.69	Nmm/mm^2

As suggested by the Rijkswaterstaat guideline a parabolic compression model, shown in Figure 7.15 is applied. This model requires the compressive fracture energy in combination with the element size and the maximum compressive strength as input parameters. The values in Table 7.2 are used.

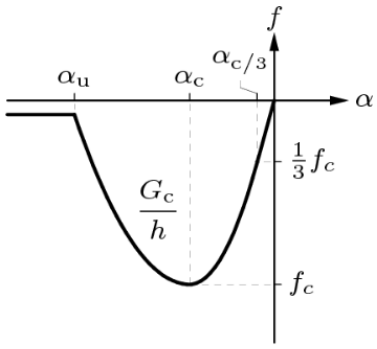

Figure 7.15: Parabolic constitutive model for concrete in compression

Three distinct strain values can be calculated which can be used for visualisation of results in the coming chapters. Firstly Equation 7.5 is used to find the strain $\alpha_{c/3}$, at which one-third of the maximum compressive strength f_c is reached.

$$\alpha_{c/3} = -\frac{1}{3}\frac{f_c}{E_c} \tag{7.5}$$

The strain α_c , at which the maximum compressive strength is reached is found with the relation in Equation 7.6.

$$\alpha_c = -\frac{5}{3}\frac{f_c}{E_c} \tag{7.6}$$

Finally, the ultimate strain α_u, at which the material is completely softened in compression, is found with Equation 7.7. It is clear that the softening branch of this behaviour model is dependent on the fracture energy exclusively. It is also possible to define a retention strength, but this was not done for this analysis.

$$\alpha_u = \alpha_c - \frac{3}{2}\frac{G_C}{hf_c} \tag{7.7}$$

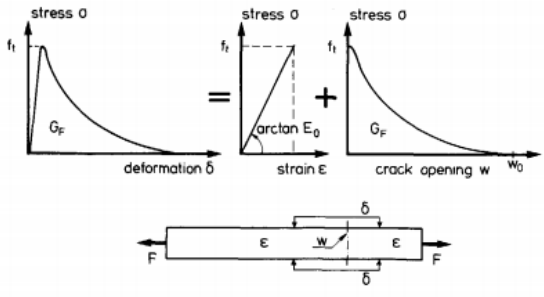

Figure 7.16: Seperation of the complete tensile stress-deformation relation for concrete into a stress-strain and a stress crack opening relation according to the fictitious crack model[9]

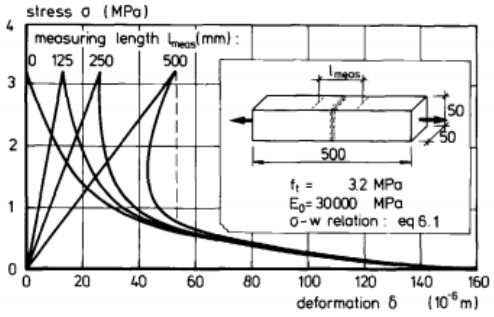

Figure 7.17: Stress-deformation relation as influenced by measuring length[9]

Using the aforementioned equations with the material properties in Table 7.2 this yields the following strains:

$$\alpha_{c/3} = -3.22e-4$$

$$\alpha_c = -16.11e-4$$

$$\alpha_u = -73.69e-4$$

7.4.3. Constitutive model for concrete in tension

There are several different constitutive models to describe the tensile behaviour of concrete. A variety of these models has been incorporated in Diana. The focus of these models is on the softening behaviour of concrete. The total material behaviour in tension is made up out of a stress-strain and a stress-crack opening relation as shown in Figure 7.16. However as the functions describing this behaviour are dependent on the element size and this model uses quite large elements, due to the size of the construction, the effect of the softening behaviour is relatively small compared to the linear behaviour up to the onset of the first cracks. In Figure 7.17 the relation between stress and deformation as influenced by measuring length has been shown, this relation holds as well for element size in numerical analysis. In this figure it can be seen that a large measuring length results in a negative post cracking slope, which makes a finite element model very unstable.

Because of the large size of the construction the cracks will spread over a large area and the force redistribution will still be accurate even when using a simpler model. For a model of this size it is beneficial to use the tension-stiffening principle. Tension-stiffening is the phenomenon where the stiffness of the structure is assumed to be significantly influenced by the fact that concrete adheres to reinforcement bars, and tensile force normal to the cracked plane is carried by the cracked concrete between cracks. Most known tension-stiffening relationships relate average stresses to average strains. This leads to the fact that the post-cracking behaviour of the concrete is less dependent on the element size. The force-elongation diagram corresponding to this behaviour is shown in Figure 7.18.

In a concrete-related tension-stiffening model it may be assumed that tension-stiffening is effective either in the whole tension area or the effective area. In the effective area approach, the influence of tension-stiffening is limited to a volume of concrete in relatively close proximity to the bar, called the tension stiffening

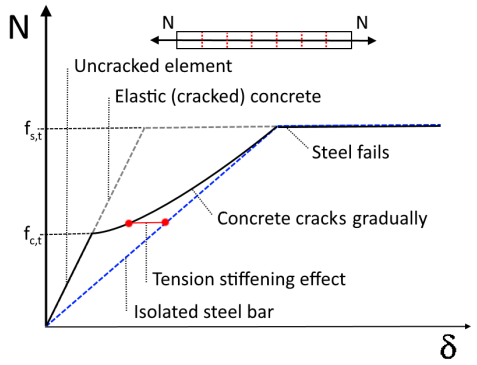

Figure 7.18: Force-elongation relation for tension stiffening behaviour of reinforced concrete structures

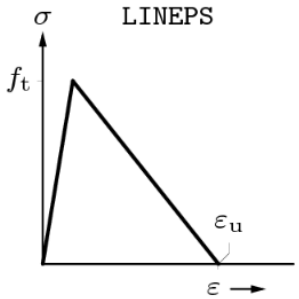

Figure 7.19: Ultimate strain based linear softening behaviour of concrete in tension

zone. Outside this zone, the second mechanism of post cracking prevails, that of tension softening[12]. Because of the size of the foundation model the cracks can be assumed to be distributed neatly over the areas in which tension occurs, so a tension-stiffening model can be applied over the whole structure. This does not yet account for the concrete in between the top and bottom where the reinforcement is located. However it has been shown that for a finite element analysis using a post-cracking relationship based on ultimate strain for an under-reinforced concrete the obtained load–deflection relationship matches an experimentally obtained one[4]. The same research states that the FE analysis results represent an upper bound for the tensile-stiffening effect. Therefore this will require careful attention post analysis.

To model the tension-stiffening behaviour the descending branch of the constitutive model in tension, or post cracking behaviour, should reflect the fact that the concrete will gradually crack until steel failure. Therefore linear softening behaviour, independent of the element size, as shown in Figure 7.19 with the ultimate strain, $\epsilon_{u,c}$, based on the reinforcement steel properties as described by Equation 7.8 is used. This method reflects the use of average stresses and strains. The fact that the concrete will not be able to reach the actual reinforcement ultimate strain and that it represents an upper bound is partially accounted for by reducing the concrete ultimate strain by half.

$$\epsilon_{u,c} = \frac{1}{2}\frac{f_{t,steel}}{E_{steel}} \tag{7.8}$$

The second important strain value in this relationship is the one corresponding to the tensile strength of the applied concrete. This strain, ϵ_{crack}, is linearly dependent on the concrete Young's modulus and is calculated with Equation 7.9.

$$\epsilon_{crack} = \frac{f_{t,c}}{E_c} \tag{7.9}$$

For the standard element size used in this model this yields the stress-strain relations in Figure 7.20. Four diagrams are shown; the first linear one is based on tension-stiffening under the assumption that the concrete fully cooperates with the reinforcement untill the steel yields. The second one is a reduced version of this, taking into account that the concrete does not fully reach the steel yield strain. The third linear relation is a simple based on the fracture energy. The Hordijk relation is a commonly used, slightly more complex

relation, also dependent on the fracture energy. It can be seen that the area under the diagrams, representing the fracture energy, and the ultimate strain value are very different. The latter two, based on fracture energy are highly dependent on element size, and therefore not suitable for this model.

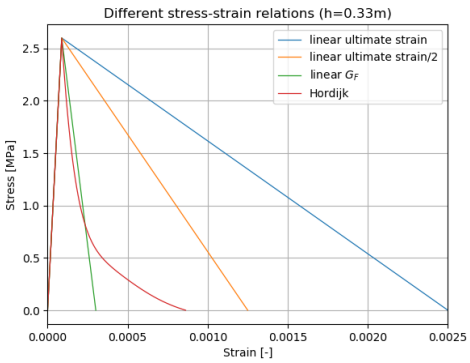

Figure 7.20: Stress-strain relations for different constitutive models for concrete in tension for the properties described above

The application of concrete model with linear post-cracking behaviour, based on the ultimate strain of steel reduced to half, resulted in analysis divergence at a significantly lower moment load than expected, namely 1.0359 in stead of around 1.27 or even higher, where failure of the structure could be expected. At the moment of divergence of the analysis some significant strains could be observed in the first principle direction in between the top and bottom reinforcement, as can be seen in Figure 7.21a, which suggest a form of splitting failure. Increasing the amount and length of the splitting reinforcement did increase the load factor for which divergence occured to 1.2347. At this load step similar, although more pronounced, strains could be observed as shown in Figure 7.21b. And even though the moment of failure for this model is closer to the expected minimum of 1.27 still no satisfactory explanation for structural failure could be found.

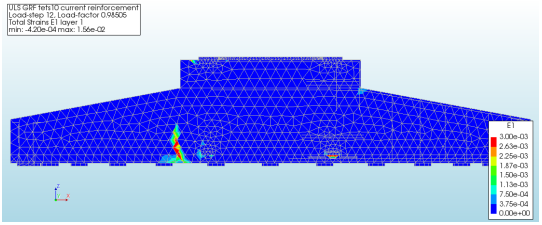

(a) Side view of σ_1 before failure (load factor of 0.98505) for a model with the current reinforcement design

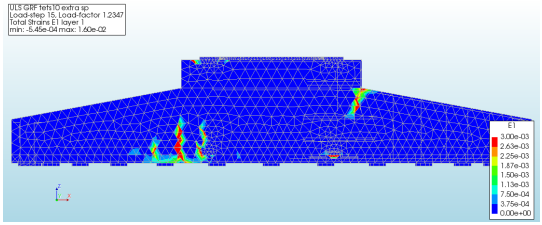

(b) Side view of σ_1 before failure (load factor of 1.2347) for a model with additional splitting reinforcement

Figure 7.21: Strain in first principle direction (σ_1) at the load step before failure for concrete modelled with a linear post-cracking stress strain relation

A possible explanation for this model instability is the abruptness of going from a gradient to horizontal in the linear stress-strain diagram. An alternative bi-linear stress-strain relationship, based on an ultimate strain of 16 times the critical concrete strain, to model tension-stiffening was suggested by Massicotte et al.[11]. This model, seen in Figure 7.22, more closely resembles other element size dependent models such as Hordijk. Because it was found that this model still suffered from problems with divergence. Allam et al.[4] suggested a modified version of this model, shown in Figure 7.23, with a more gradual response behaviour. Another benefit of this model is that the total fracture energy is slightly reduced while keeping the tensile strength and ultimate strain the same, which reduced the overestimation of total concrete strength.

In Table 7.3 the corresponding stresses and strain are found for the diagram in Figure 7.23 for the material properties used in the reference project. It must be noted that the ultimate strain is similar to the approximately $1.31e-3$ derived from the, reduced by half, ultimate strain of the reinforcement used for the linear post-cracking behaviour.

In Figure 7.24 the first principal strain at analysis failure for the modified Massicotte (or Allam) model is compared to the one for the linear model. In Figure 7.24a one clear splitting crack is shown, while the result in Figure 7.24b shows a more distributed cracking pattern. The failure load factor of the multi-linear model is lower than that of the linear one. This can be explained because of the fact that total fracture energy under

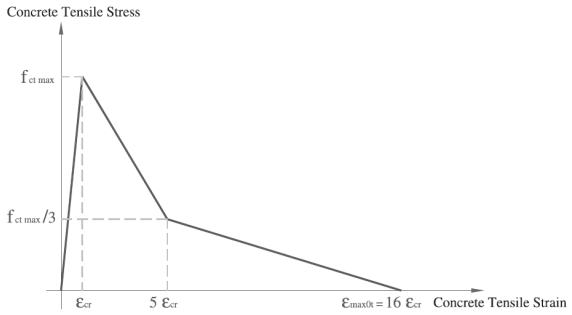

Figure 7.22: Stress-strain relationship suggested by Massicotte et al.[11]

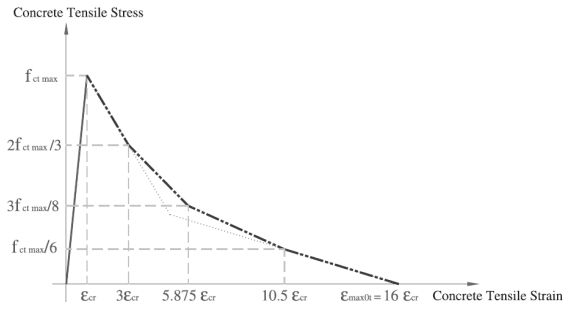

Figure 7.23: Modified multi-linear stress-strain relationship as suggested by Allam et al.[4]

Table 7.3: Reinforcement material properties

Stress [MPa]	0	2.60	1.73	0.97	0.32	0
Strain	0	$8.85e-5$	$2.65e-4$	$5.20e-4$	$9.29e-4$	$1.416e-3$

the multi-linear curve is lower than that under the linear one. However this is still contrary to expectations as increased stability was expected from the use of a more graduate post-cracking curve. As the multi-linear model did not increase the stability the linear model was used for further analysis.

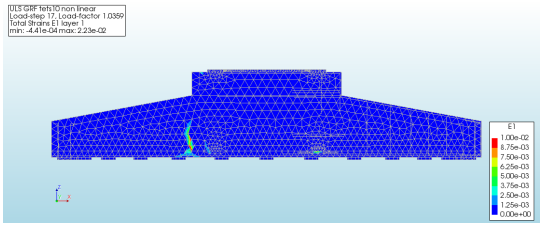

(a) First principal strain at failure load (1.0359) for linear post-cracking behaviour

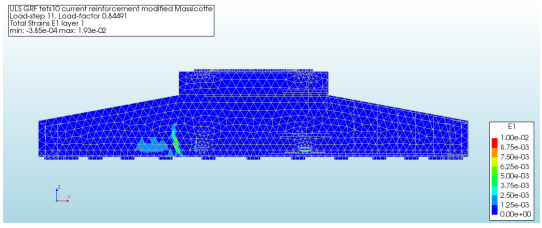

(b) First principal strain at failure load (0.8449) for modified Massicotte (multi-linear) post-cracking behaviour

Figure 7.24: Comparison of strain in first principle direction (σ_1) at the load step before failure for linear and multi-linear post-cracking models

To provide a better understanding of the effect of using a linear post-cracking relationship based on ultimate strain a comparison to concrete with the Hordijk softening relation can be made. This can be done for a smaller simpler model as to avoid having to use larger elements due to time and computational restraints as well as making understanding of the results easier. When a smaller element size is used the different constitutive relations become more comparable. This is illustrated in Figure 7.25 where a reduced element size was used in the calculation of the stresses. This shows that the linear reinforcement based ultimate strain model indeed offers a way to reduce element size sensitivity.

The Rijkswaterstaat guideline advices another alternative for dealing with the mesh size dependency of the post cracking behaviour when using a smeared crack model. A model based on fracture energy, as shown

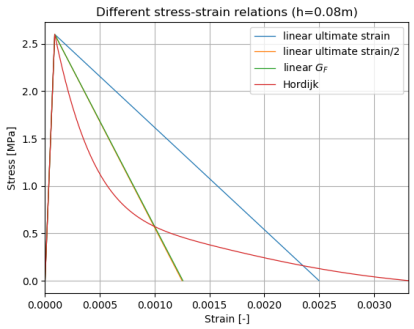

Figure 7.25: Stress-strain relations for different constitutive models for concrete in tension for the properties described above for a reduced element size

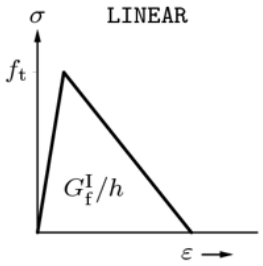

Figure 7.26: Tensile constitutive model based on fracture energy

in Figure 7.26, is based on the assumption that one crack per element will occur. But when larger elements are used in a big structure the expected crack spacing is smaller than the element size. Therefore multiple cracks would occur per element. This can be corrected by multiplying the fracture energy by the amount of expected cracks per element based on the equivalent length. This method can be used for any model based on fracture energy such as the exponential or Hordijk models as well.

According to the Eurocode[1] the average crack spacing can be calculated using Equation 7.10

$$s_{r,max} = k_3 c + \frac{k_1 k_2 k_4 \phi_{eq}}{\rho_{ef}} \tag{7.10}$$

where:

- c = concrete cover
- ϕ_{eq} = equivalent bar diameter for a mixture of bar diameters
- $\rho_{ef} = A_s / A_{cef}$
- A_s = area of steel
- A_{cef} area of effective embedment zone where the reinforcing bars can influence the crack width
- k_1 = coefficient for bond properties of the bar (between 0.8 and 1.6 for high bond bars and for bars with an effectively plain surface respectively)
- k_2 = coefficient for strain gradient (between 0.5 and 1.0 for pure bending and pure tension respectively)

The values of k_3 and k_4 for use in a country may be found in its National Annex. The recommended values are 3.4 and 0.425 respectively. Furthermore an intermediate value of 1.2 was taken for k_1 to represent normal bonding. and lastly the lower limit of 0.5 was used for k_2 as this is primarily a bending problem. The equivalent reinforcement diameter is calculated using Equation 7.11.

$$\phi_{eq} = \frac{n_1 \phi_1^2 + ... + n_n \phi_n^2}{n_1 \phi_1 + ... + n_n \phi_n} \tag{7.11}$$

Radial rebar check

Section	R (m)	h (m)	d (mm)	z (mm)	a_l (m)	Rebar 1	Rebar 2	Rebar 3	A_{sl} (mm²/m)	cover (mm)	M_d (kNm/m)	$A_{s;req}$ (mm²/m)	U.C. (-)	
Top radial -1	1.200	2.385	2285	2057	1.028	88 Ø16		50 Ø20	4430	66	2672	2726	0.62	
Top radial 1	1.800	2.385	2285	2057	1.028	113 Ø16	50 Ø25	50 Ø20	5568	66	4307	4433	0.80	(Mgem)
Top radial 2	2.300	2.385	2285	2057	1.028	50 Ø25	50 Ø25	50 Ø20	4484	66	4491	4627	1.03	(Mgem)
Top radial 3	3.000	2.366	2266	2039	1.020	50 Ø25	50 Ø25	150 Ø20	5104	66	4355	4522	0.89	(Mgem)
Top radial 4	4.000	2.183	2083	1875	0.937	50 Ø25	50 Ø25	150 Ø20	3828	66	3257	3669	0.96	
Top radial 5	5.000	1.999	1899	1709	0.855	50 Ø25	50 Ø25	100 Ø20	2563	66	2090	2571	1.00	
Top radial 6	6.000	1.816	1716	1544	0.772	100 Ø12	50 Ø25	100 Ø20	1784	66	1313	1781	1.00	
Top radial 7	8.200	1.412	1312	1181	0.590	150 Ø12	50 Ø25	100 Ø20	1415	66	317	558	0.39	
Bottom radial -1	1.300	2.385	2285	2057	1.028	82 Ø20	50 Ø32		8077	50	-6796	7088	0.88	
Bottom radial 1	1.800	2.385	2285	2057	1.028	113 Ø20	75 Ø32		8472	50	-7133	7454	0.88	(Mgem)
Bottom radial 2	2.200	2.385	2285	2057	1.028	138 Ø20	75 Ø32	50 Ø20	8636	50	-7725	8100	0.94	(Mgem)
Bottom radial 3	3.000	2.366	2266	2039	1.020	188 Ø20	75 Ø32	100 Ø20	8000	50	-7198	7593	0.95	(Mgem)
Bottom radial 4	4.000	2.183	2083	1875	0.937	252 Ø20	75 Ø32	100 Ø20	6800	50	-6071	6966	1.02	
Bottom radial 5	5.500	1.907	1807	1626	0.813	315 Ø20	75 Ø32		4609	50	-3468	4543	0.99	
Bottom radial 6	7.000	1.632	1532	1379	0.689	320 Ø20	75 Ø32		3657	50	-1616	2471	0.68	
Bottom radial 7	8.200	1.412	1312	1181	0.590	438 Ø20			2671	50	-524	927	0.35	

Calculation notes
Rebar is checked at R, where the depth of the section is the lowest.

Explanation

R	=	Lever arm of internal forces.	Rebar n	=	Bending rebar in cross section (tension only)
h	=	Height of cross-section at R.	A_{sl}	=	Total applied radial rebar.
d	=	Effective depth of cross-section.	cover	=	Cover on reinforcement.
z	=	Lever arm of internal forces in section,	M_d	=	Bending moment from Diana.
a_l	=	Distance to shift the start of anchorage according to [9.2].	$A_{s;req}$	=	Required bending rebar in section, calculated using calculated z.
			U.C.	=	Unity check on bending rebar. U.C. < 1.0 is ok.

Figure 7.27: Table in which the cross-sectional areas of the reinforcement are collected from which the reinforcement ratio is derived

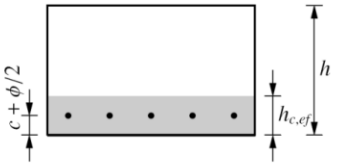

Figure 7.28: Effective area in a concrete slab for determination of crack spacing

In Figure 7.27 the amount of reinforcement bars per section and their corresponding diameters can be found. In this case the values for a distance of three metres from the centre point were taken as this is where the first cracks are expected.

To find A_s the amount of reinforcement bars per section present at 3 meters from the centre was multiplied by the cross-sectional area of the bars in that section. The concrete cover is also taken from Figure 7.27, which can be used to find the effective height, using the relation $h_{cef} = 2.5\left(c + \frac{\phi}{2}\right)$ for calculation of the area of the effective embedment zone as shown in Figure 7.28.

Subsequently the effective height is multiplied by the circumference at 3 meters to find the effective concrete area A_{cef}. Subsequently the reinforcement ratio can be found as shown in Equation 7.12. Additionally the the reinforcement ratio of the orthogonal reinforcement was calculated as shown in Equation 7.13.

$$\rho_{ef} = \frac{A_{s,rad}}{A_{cef}} = \frac{\sum_{i=1}^{4} \frac{1}{4}\pi\phi_i^2}{2\pi 3 h_{ef}} = \frac{0.07565}{18.850.1925} = 0.0208 \tag{7.12}$$

$$\rho_{ort} = \frac{A_{s,ort}}{A_{cef}} = \frac{n_{permeter} A_{s,ort,bar}}{h_{ef}} = \frac{90.2827e-2}{0.1925} = 0.0147 \tag{7.13}$$

Together this yields a reinforcement ratio of $\rho_{ef} = 0.0208 + 0.0147 = 0.0355$. It should be noted that this is higher that 0.02, which is normally considered as the reinforcement ratio value for which compressive strength becomes governing in ULS verification as the reinforcement will not reach its yield strength and undesirable brittle failure can occur.

Although the shape of the structure and the irregular reinforcement density make an exact calculation of the crack width difficult a rough estimation can be made. Using the previously described values this yields a crack spacing of around 382mm which is larger than the element size 320mm although it is of the same order of magnitude. While it is not needed for this specific case, the fracture energy can be found with Equation 7.14, where: $n_{cr} = max\left(1, \frac{h_{eq}}{s_{r,max}}\right)$.

$$G_F^{RC} = n_{cr} G_F \tag{7.14}$$

The tensile models that are described above are compared in Figure 7.29. As the assumed equivalent length was the same as the element size and the actual calculated crack spacing is slightly larger a reduced

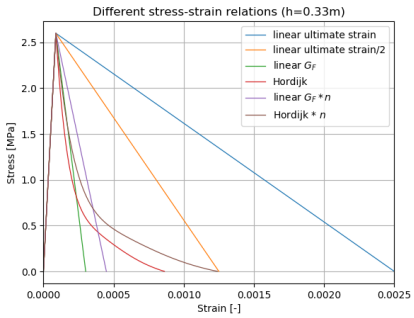

Figure 7.29: Stress-strain relations for different constitutive models for concrete in tension for the properties described above for the default element size

crack spacing based only on the concrete cover, $s_{r,max} = k_3 c = 224$mm, was used to illustrate the principle. The area under the diagram, which is directly related to the fracture energy is higher for the ultimate reinforcement strain models. This can be explained by the fact that the post cracking behaviour is much stiffer and prevalent because of the influence of the reinforcement in structure. In terms of ultimate strain the exponential model is quite similar, although the area under the diagram is still much lower. Another commonly used tensile model is the Hordijk stress-strain relation. This is also included in Figure 7.29.

7.5. Steel fibre reinforced concrete

As the reinforcement in the structure is already quite extensive, increasing it is impractical. Instead the application of SFRC can improve structural behaviour without increasing the complexity of the current reinforcement design. To optimize the material use it is also likely that partial omission of reinforcement bars in combination with the introduction of SFRC will not reduce the resistance of the structure.

7.5.1. Constitutive model

Fibre reinforcement only marginally improves the compressive behaviour of concrete[13], and as previously described the material properties used for concrete were calculated using the compressive strength, so it is not possible to simply increase the concrete class to represent the addition of steel fibres.

When taking into account the tension stiffening effect, as steel bars will still be used, the detailed softening behaviour which can differ from classical concrete becomes somewhat less important. The addition of fibres does yield higher fracture energy[5] and concrete tensile strength[13], thus altering the concrete stress-strain relation. As the ultimate strain remains the same because it was calculated using the rebar steel material properties increasing the concrete tensile strength will consequently also increase the fracture energy.

The mechanical performance of steel fibre reinforced concrete depend on various properties. The water-to-cement ratio and aggregate of the concrete itself is important, but so are the length, diameter and volume fraction of the fibres. According to [3] significant change in the mechanical properties of concrete can be observed like an increase of in between 10-25% in compressive strength but, in this case, more importantly about 31–47% increase in direct tensile strength

For a simple feasibility study compressive strength was multiplied by 1.17 and tensile strength by 1.39. The fibres in the concrete take op tensile stresses in micro cracks, which translates to increased fracture energy. This increase is automatically accounted for when the tensile strength is increased considering that the fracture energy is represented by the area under the stress-strain diagram.

7.6. Analysis parameters

For a non-linear analysis the outcome may be heavily influenced by the analysis parameters.

7.6.1. Loading sequence

Not all loads are applied simultaneously in reality, but as they do determine stresses present and more importantly the stiffness, and subsequent resistance, of certain areas of the structure they need to be applied sequentially. The applied loading sequence is:

1. Presstressing load on the anchor cage;

Table 7.4: Convergence criteria

Norm	Tolerance
Displacement	0.01
Energy	0.001

2. Self weight of the concrete structure including reinforcement in combination with vertical turbine load;
3. Load combination 20: moment load extreme moment caused by wind, horizontal wind load and additional moment due to eccentricity of horizontal load.

Although in reality prestressing would be applied after the self weight of the construction, this requires a slightly more complex phased analysis, which has been skipped because of the limited effect on the end result of the analysis.

7.6.2. Load steps

To be able to use this model for general design checks for multiple projects it is convenient to use the automatic step size option in Diana, as it will be generally unknown how the structure will behave and when the critical moments will occur. To determine an upper bound for the structure resistance a total step size of 2.0 was used with a maximum step size of 0.05, which is relative to the maximum load factor so this results in steps of 0.1. The reduction factor is 0.25, which means that if convergence is not reached within the allowed number of iterations it will reduce the load step to a quarter of the previous step. If a step size of 0.001 is reached in this manner the analysis will abort.

7.6.3. Solution procedure

For this analysis the regular Newton-Raphson iteration method is applied. A maximum of 20 iterations is specified. Analyses with a higher amount of iterations were performed but this did not improve model stability, while increasing the computational time. To improve the convergence behaviour a line search algorithm was used.

7.6.4. Convergence criteria

The convergence criteria determine the accuracy and reliability of the analysis results. If the convergence tolerance is chosen too big the resultant equilibrium will deviate too much from the actual one. However the tolerance cannot be infinity small either as this would result in an analysis that will never reach convergence. For this analysis the combination in Table 7.4 was chosen. The maximum number of iterations was set to 25.

8

Results of the non-linear analysis

For the results the potential failure modes and the corresponding load in terms of load factor will be defined for ultimate limit state analysis. Additionally the previously described control parameters will be analysed for the serviceability limit state. In this chapter primarily the moment of failure will be treated which occurred at a load factor of 1.0359 for this specific project, which is lower than expected considering the fact that the GRF method requires a post analysis division by a factor of 1.27.

8.1. Displacements

The overall vertical displacement just before failure is distributed as shown in Figure 8.1. It clearly is somewhat less symmetrical than was observed for the linear analysis, which can be attributed to the non-linear behaviour of the structure but it must also be taken into account that this is the result of a combination of loads while the primary focus of the linear analysis results was on isolated load cases. The negative displacement is of roughly the same magnitude as was determined in the linear analysis, but the positive displacement was reduced to approximately a third.

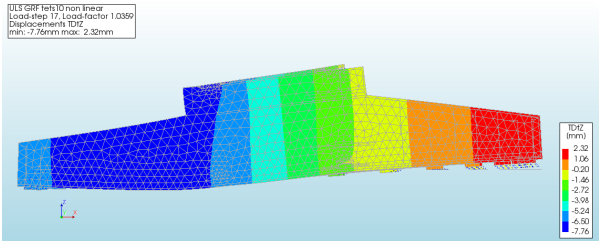

Figure 8.1: Vertical displacements in side view. Load factor 1.0359

8.1.1. Rotation of the tower base

The allowable inclination of the turbine tower has been limited to 12.5 mm m^{-1} by the manufacturer for this project. As this is a small rotation this translates to 0.0125 radians of rotation of the turbine base. This rotation can simply be found by comparing the vertical displacement at both extremes of the top load spreading plate, or any two points at equal distance from the centre along the x-axis actually, and dividing this by the distance in between them as clarified by Figure 8.2. With an increasing load this results in the diagram in Figure 8.3. It is clear that at the moment of failure the rotation of the tower base is well within the set limits.

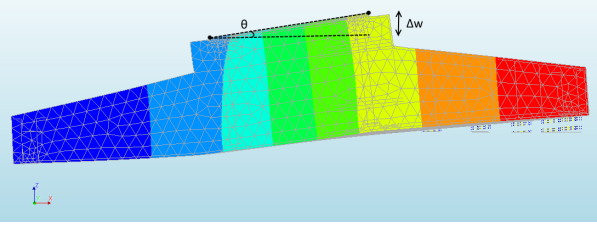

Figure 8.2: Visualization of the method for calculating the rotation of the tower base

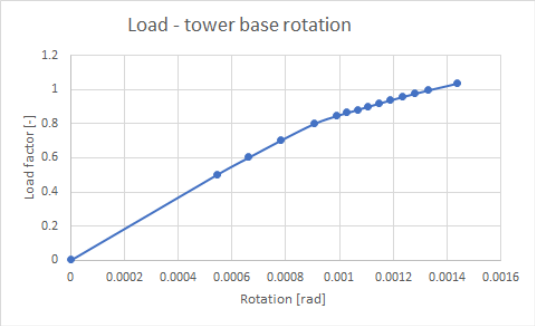

Figure 8.3: Load-rotation diagram. Rotation of the tower base. Load factor corresponding to moment load introduction

8.1.2. Load spreading plate-pedestal relative displacement

When the relative displacement between the LSP and the pedestal becomes positive this means that a gap is formed between the LSp and grout layer. The initial negative relative displacement represents compression of the intermediate grout layer. It is important that the gap between them, shown in Figure 8.4, stays limited as opening and closing cyclically may cause significant damage to the grout layer and subsequently the pedestal. In Figure 8.5 it can be seen that the opening of the gap starts at a load factor of approximately 0.7 at the outer edge of the LSP and is opening up at the inner edge at little under 1.0. This is somewhat low and perhaps an increased prestressing load is required, although the applied moment load is the extreme load case which is not likely to occur often. This is however an important issue as it is rather critical when looking at fatigue loading.

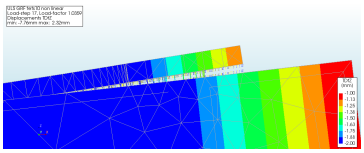

Figure 8.4: Close up view of the gap that arises between the pedestal and top LSP, which is represented by the relative displacement

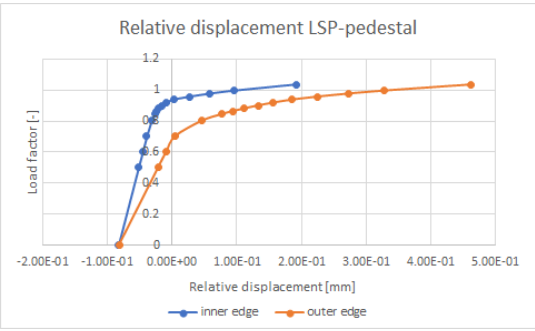

Figure 8.5: Load-displacement diagram. Relative displacement between LSP and pedestal. Load factor corresponding to moment load introduction

8.2. Prestressing of the anchor cage

Prestressing of the anchor cage increases the moment resistance of the structure as it reduces tensile stresses in vertical direction caused by moment loading. The anchor cage will move together with the structure, calling on the bending resistance of the construction, but also relative to the rest of the structure which leads to specific behaviour. In Figure 8.6 different phases of the combined behaviour of the anchor cage under prestressing load and the concrete are shown. By tightening the nuts, essentially a tensile force is applied and the anchor cage is prestressed as shown in Figure 8.6a. As the the bolts are tightened the space in between the LSP's is reduced and the concrete in between the two LSP's effectively functions as a compressive spring as can be seen in Figure 8.6b. When the moment load is applied it leads to one side of the anchor cage being loaded in tension, thus elongating the anchor bolt leading to an increase in tension in the bolt, but simultaneously decreasing the compressive stress in the "concrete spring". This is illustrated in Figure 8.6c. The last distinctive phase is when the "concrete spring" is fully relaxed and the tensile forces in the top LSP are directly transmitted to the bottom LSP, shown in Figure 8.6d, which will then lead to a significant increase in loading in the bottom of the structure.

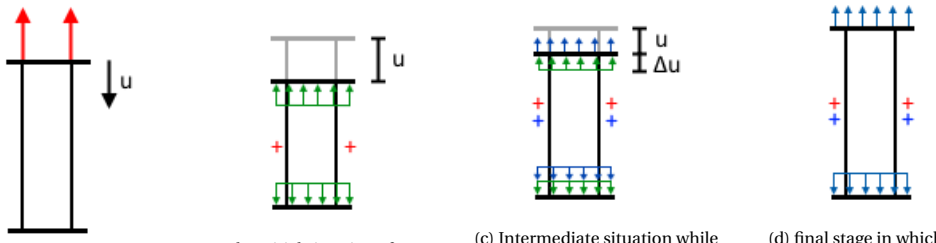

(a) Start of the prestressing load introduction.

(b) Initial situation after introduction of the prestressing load. concrete 'spring' is fully loaded

(c) Intermediate situation while introducing the tensile stresses on the upper LSP caused by the moment load. Concrete spring is relaxing.

(d) final stage in which the concrete spring is fully relaxed and equilibrium is only caused by the concrete resistance at the bottom LSP.

Figure 8.6: Different situations for the side of the anchor cage in tension in combination with intermediate concrete

When the relative displacement between the LSP and pedestal is higher that 0, which means that the 'concrete spring' is fully relaxed and the load is directly introduced into the bottom of the structure. This may cause unstable behaviour. Figure 8.7 shows the behaviour presented schematically in Figure 8.6 in the non linear analysis.

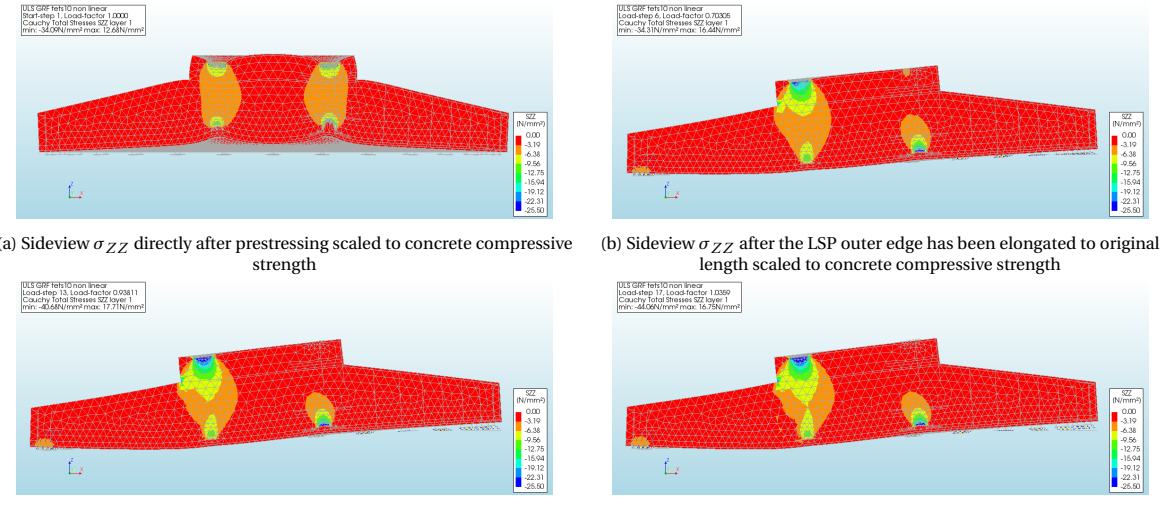

(a) Sideview σ_{ZZ} directly after prestressing scaled to concrete compressive strength

(b) Sideview σ_{ZZ} after the LSP outer edge has been elongated to original length scaled to concrete compressive strength

(c) Sideview σ_{ZZ} after the LSP inner edge has been elongated to original length scaled to concrete compressive strength

(d) Sideview σ_{ZZ} at load step before failure, scaled to concrete compressive strength

Figure 8.7: Different situations for the side of the anchor cage in tension in combination with intermediate concrete

The fact that unbonded anchor bolts are used in the anchor cage results in compressive stresses in the bottom of the structure above the load spreading plates. As these plates have no tensile connection to the

concrete interfaces must be applied to reach a realistic load transfer. This way of construction also leads to the fact that the applied moment load is also actually applied around the centre of mass of the foundation and not at the top of the pedestal.

The effects of prestressing the anchor cage are largely determined by the amount of applied prestressing. Damage due to cyclic fatigue loading and the potential risk of failure by pulling out of the anchor cage can be reduced by increasing the prestressing load on the anchor bolts. To determine the effect of different prestressing loads additional calculations were done for which the prestressing load was multiplied by a load factor. In Table 8.1 the model failure loads corresponding to different prestressing load factors are collected. For the stability of the model it appears to be beneficial to reduce the prestressing load. However, this will likely affect the fatigue damage negatively. The effects on the actual structural stability are still unclear, as the stresses and strains do not convincingly suggest mechanical failure.

Table 8.1: Influence of the amount of prestressing on the ultimate load

Prestressing factor	Ultimate load factor (wind load)
0.7	1.2233
1.0	1.0359
1.25	1.0394
1.5	0.8932

8.3. Strains and stresses

While chapter 6 focussed on distributed moments and stresses, for the results of this non linear analysis the resulting strain are more meaningful as the stresses in the structure will fluctuate as cracking of the concrete occurs. The general strain behaviour of the construction was already predicted with the previous linear calculations. The principal differences are caused by the limit values corresponding to the non-linear material properties used. Only when the structure as a whole starts behaving sufficiently non-linear larger differences may occur.

8.3.1. Concrete strains

The maximum strain values caused by a moment around the y-axis are expected in global x direction in the centre cross section. In the linear analyses the distribution of strains as a result from moment loading are more or less anti-symmetric along the x-axis as well as the y-axis when looking at the side view cross-section. Figure 8.8 shows that this is not as much the case for a non linear analysis. To illustrate this the values for compression and tension have been limited to equal values, showing that although the general locations of compression and tension are still the same the distribution has changed significantly. Figure 8.8 also shows that before cracking is shown to illustrate the fact that initially there was a significant compressive zone. The 2D and 3D linear analyses showed quite significant, almost symmetrical, tensile stresses and strains in the top of the structure next to the pedestal. The non-linear analysis shows that the tensile strains in the top of the structure are lower and less spread out. This is a result of the non-linear stress redistribution.

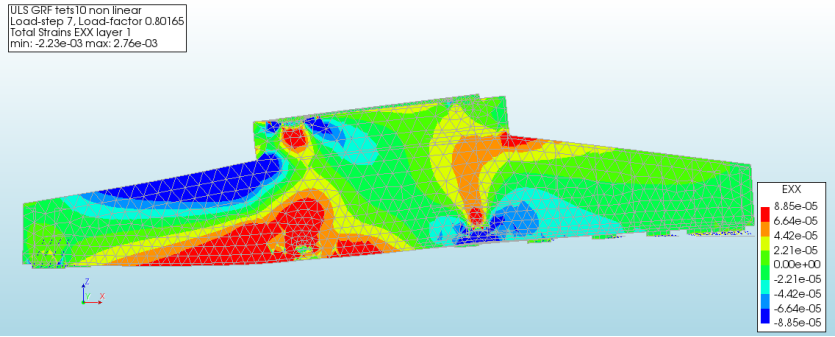

Figure 8.8: Side view of concrete strains ϵ_{XX} at load step before significant cracking (load factor 0.80166) scaled symmetrically

As the order of magnitude for compressive strains is higher than for tensile ones Figure 8.9 has been scaled only show compressive strains in global X direction up to $\alpha_c = -16.11e-4$ corresponding to the compressive

strength. In this figure red represents concrete that is not in compression, which is nearly the entire structure. Similarly Figure 8.10 only shows the tensile strains, only now they are represented by the red area. Figure 8.11 shows the concrete strain left of the pedestal at approximately two thirds of the height of the structure. This strain gradually increases until right before failure when it abruptly becomes positive. This shows that the compression zone reduces. However at the moment of failure the concrete in the reduced compression zone has not reached the compressive strength, which means that it should still be able to resist a bending moment. Additionally there is also reinforcement in this zone functioning as compression reinforcement.

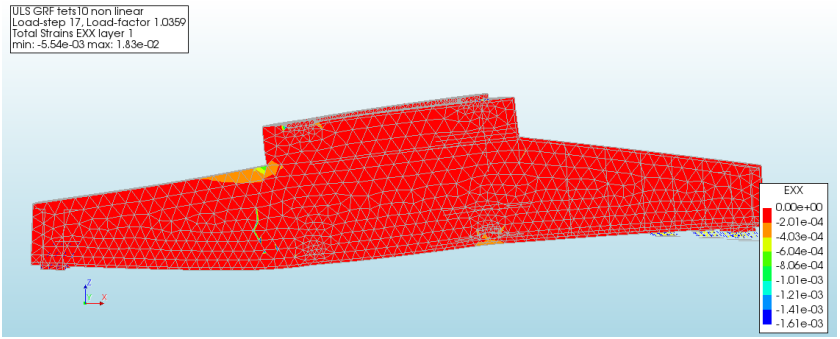

Figure 8.9: Side view of concrete strains ϵ_{XX} at load step before failure (load factor 1.0359) scaled to compressive strength of concrete

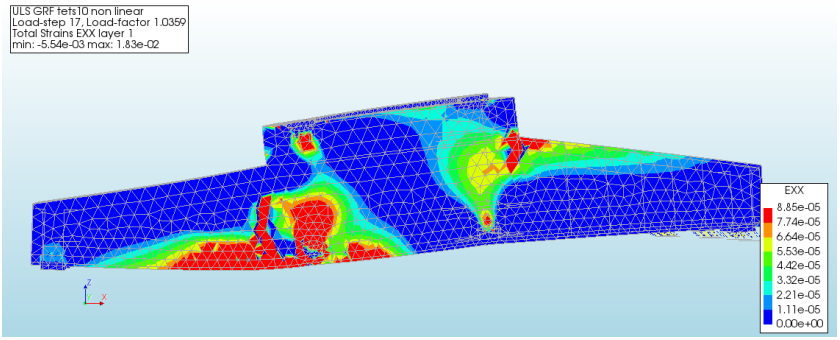

Figure 8.10: Side view of concrete strains ϵ_{XX} at load step before failure (load factor 1.0359) scaled to tensile strength of concrete

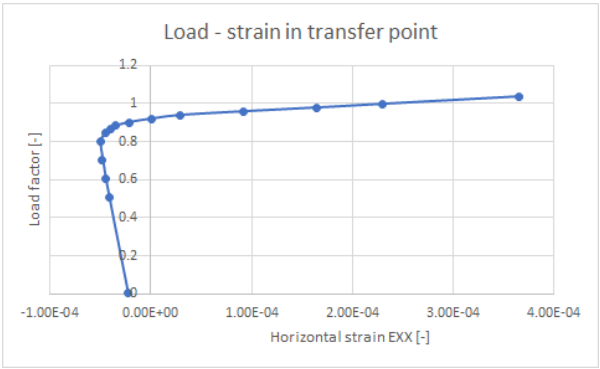

Figure 8.11: Load-strain diagram. ϵ_{XX} left above mid height in the point that becomes the transfer of tensile to compressive zone. Load factor corresponding to moment load introduction

Figure 8.12 in which the scale is limited to the ultimate strain based on the ultimate strain of steel shows that at the moment of failure a large part of the concrete in the proximity of the main fracture had no tensile capacity at all.

Although it is not as clear when the strain is scaled to the ultimate concrete strain, Figure 8.13 shows that the largest strain does not occur at the absolute bottom, but above it. This form of cracking can be called splitting cracking.

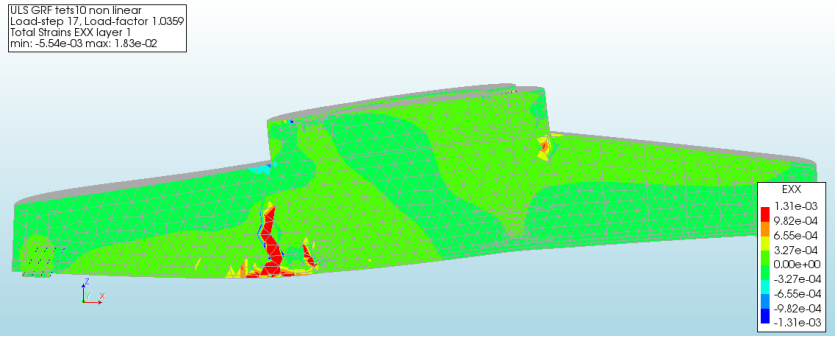

Figure 8.12: Side view of concrete strains ϵ_{XX} at load step before failure (load factor 1.0359) scaled to the ultimate tensile strain as applied in the linear constitutive model

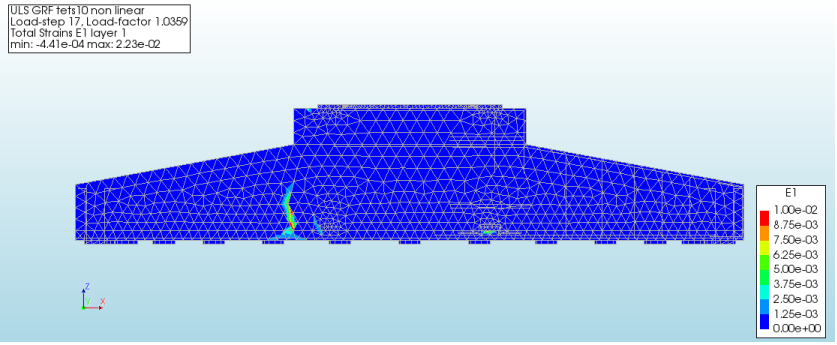

Figure 8.13: Side view of concrete strains ϵ_1 at load step before failure (load factor 1.0359) scaled to the scaled to only show positive strain

In Figure 8.14 the concrete strain in the bottom under the left side of the pedestal is shown which suggests concrete cracking after which the strain drastically increases.

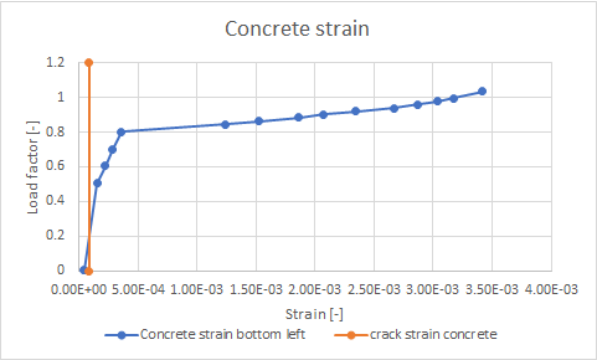

Figure 8.14: Load-strain diagram. ϵ_{XX} at the bottom left of the structure where first concrete yielding is seen. Load factor corresponding to moment load introduction

8.3.2. Reinforcement strains

The reinforcement strains and resultant stresses logically follow from the previously shown concrete strains. As the concrete reaches its cracking strain it will crack and the reinforcement will become active. Figure 8.15 and Figure 8.16 show the reinforcement stresses in global x-direction, which is along the longitudinal reinforcement that can be seen in the side view cross section. Both figures show that significant reinforcement stress only occur reasonably locally. Figure 8.18 shows that for the configuration in the reference project no significant reinforcement stresses in vertical direction are present at the moment of failure.

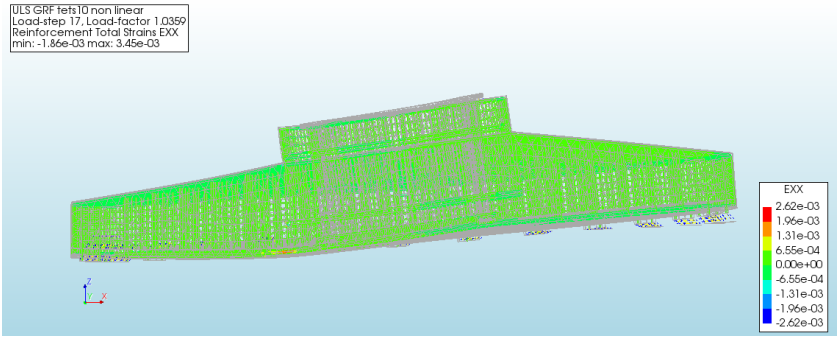

Figure 8.15: Side view of reinforcement strains $\epsilon_{XX,reinf}$ at load step before failure (load factor 1.0359) scaled to reinforcement yield strength

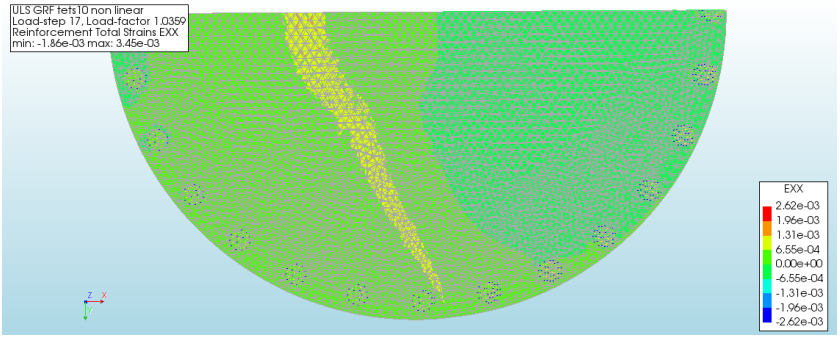

Figure 8.16: Bottom view of reinforcement strains $\epsilon_{XX,reinf}$ at load step before failure (load factor 1.0359) scaled to reinforcement yield strength

To provide a better insight into the distribution of the strains in the reinforcement Figure 8.17 has been included. It shows that minor reinforcement strain concentrations are found around the pedestal as well as in the bottom of the structure. This information can help predict the reinforcement behaviour for increased moment loading.

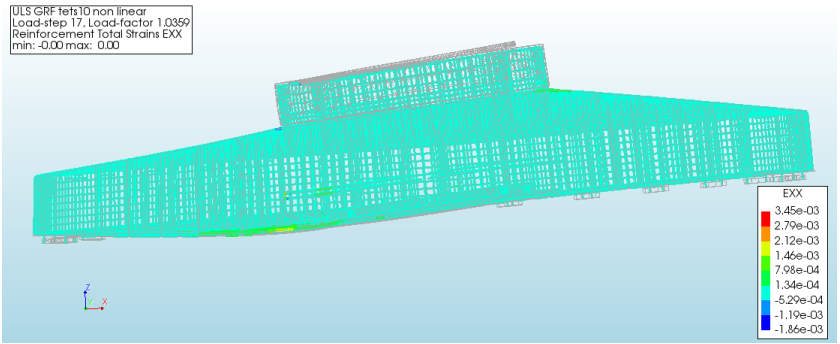

Figure 8.17: Side view of reinforcement strains $\epsilon_{XX,reinf}$ at load step before failure (load factor 1.0359) as scaled automatically

Because the expected ultimate loading is not reached it is not only interesting to see whether the ultimate values are reached, but also where the highest strains can be found. In Figure 8.19 it can be seen that vertical

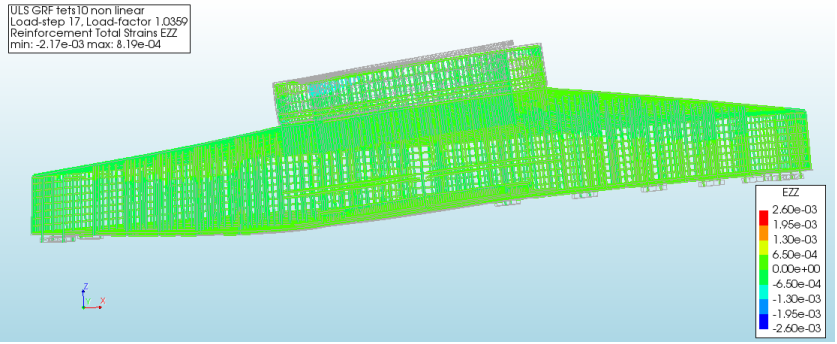

Figure 8.18: Side view of reinforcement strains $\epsilon_{ZZ,reinf}$ at load step before failure (load factor 1.0359) scaled to reinforcement yield strength

strains are primarily concentrated in and around the pedestal, as well as close to the foundation piles which are in compression.

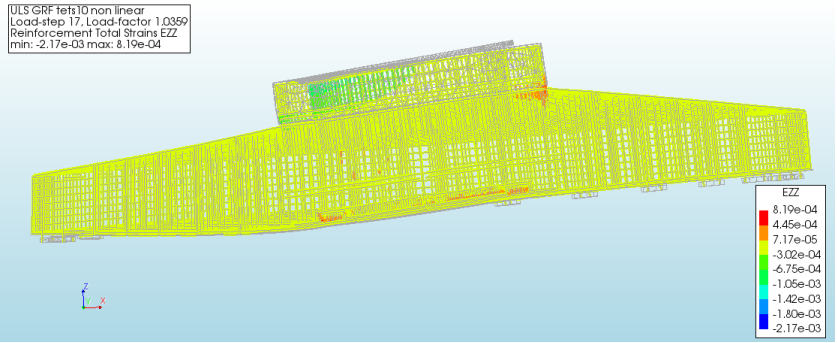

Figure 8.19: Side view of reinforcement strains $\epsilon_{ZZ,reinf}$ at load step before failure (load factor 1.0359) as scaled automatically

Figure 8.20 shows the increase of reinforcement stress at the bottom of the structure under the left edge of the pedestal as the moment load is increased. As previously described a superfluous reinforcement ratio can cause the reinforcement not to reach its yield strength which in turn can lead to brittle failure. Clearly the reinforcement stress has not reached its yield value when the construction fails.

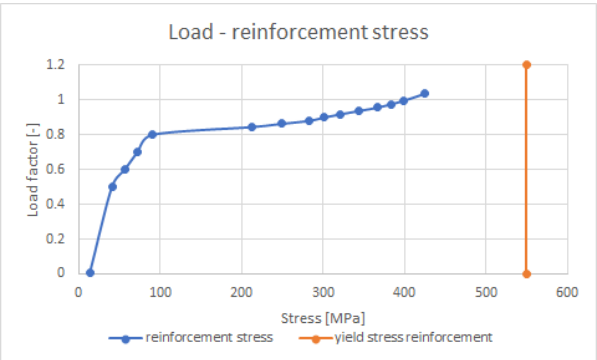

Figure 8.20: Load-stress diagram. $\sigma_{XX,reinf}$ at the bottom left of the structure where first concrete yielding is seen. Load factor corresponding to moment load introduction

Figure 8.21 shows the reinforcement stress in the outer left point of the slitting reinforcement. It can be seen that the reinforcement yield stress is reached at the moment the convergence problem occurs.

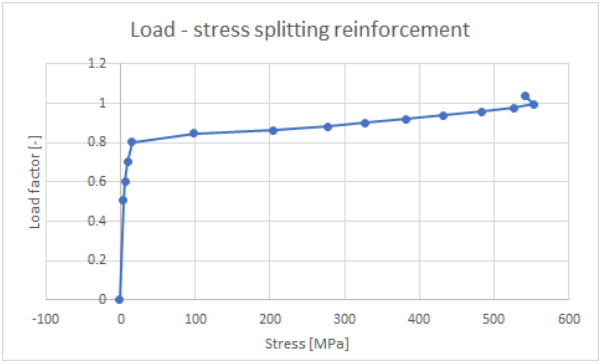

Figure 8.21: Load-stress diagram. $\sigma_{XX,reinf}$ in the outer end of the left splitting reinforcement bar. Load factor corresponding to moment load introduction

8.4. Concrete cracking behaviour

The cracking behaviour of a concrete structure is important as this determines where reinforcement is activated and where concrete stresses will be redistributed. Additionally expected crack widths should be limited as too wide cracks may result in corrosion of the reinforcement and significantly decrease the structural capacity of the construction. For this project for instance a maximum value of 0.20mm has been specified for the crack width.

8.4.1. Crack pattern

Firstly it is important to note that the crack widths that are shown in the forthcoming figures can't be translated to reality one-on-one as they should be corrected for the expected amount of cracks per element as described in chapter 7

The first cracks that occur in this analysis are the result of the introduction of the prestressing load on the anchor cage. As the anchor bolts are not bonded to the concrete the load spreading plates are simply pulled together leading to some minor crushing directly above the bottom LSP. As shown in Figure 8.22.

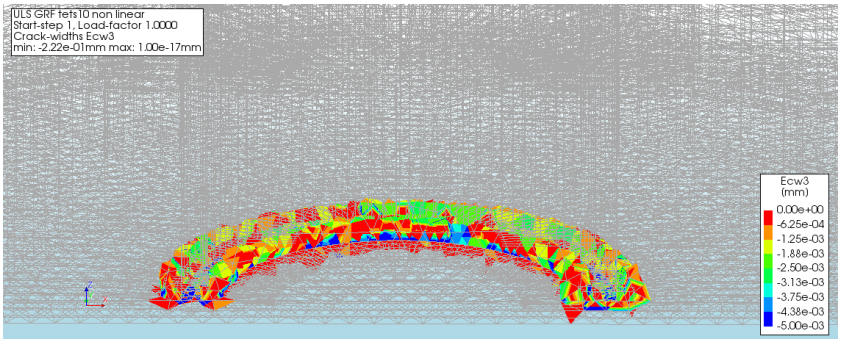

Figure 8.22: Close up of the crack width w_3 around the bottom LSP in sideview directly after prestressing, showing some minor crushing

In the analysis the next steps are the self weight of the concrete structure and the vertical load from the turbine tower, which both have similar effect, namely positive strain in the bottom of the structure as previously described which produces some concrete cracking in the bottom of the foundation although this is quite minor as can be seen in Figure 8.23b additional cracking compared to after prestressing as shown in Figure 8.23a is minimal.

The cracking behaviour of primary interest is that which is the result of the moment loading. The main locations for cracking are right from the centre in the top of the main structure and left from centre slightly above the bottom. This is somewhat different than expected from the stress distribution calculated in the linear analysis. The expectation was that the crack would start all the way at the bottom. Although the presence of reinforcement at the bottom leads to this internal cracking first. The first cracks originate at the centre cross section shown in Figure 8.24, and progress towards the outer edge of the structure as can be noticed most evidently in Figure 8.27 and also somewhat in Figure 8.29.

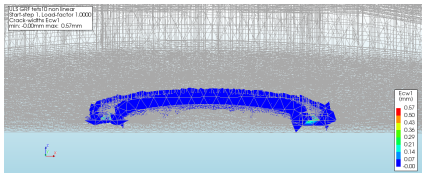

(a) Close up of the crack width w_1 around the bottom LSP in sideview directly after prestressing, showing some minor crushing

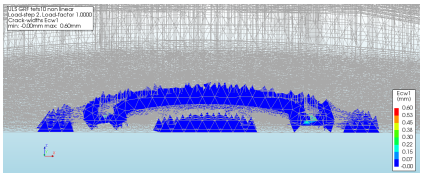

(b) Close up of the crack width w_1 around the bottom LSP in sideview directly after introducing self weight

Figure 8.23: Cracking around the bottom LSP before and after introducing self weight

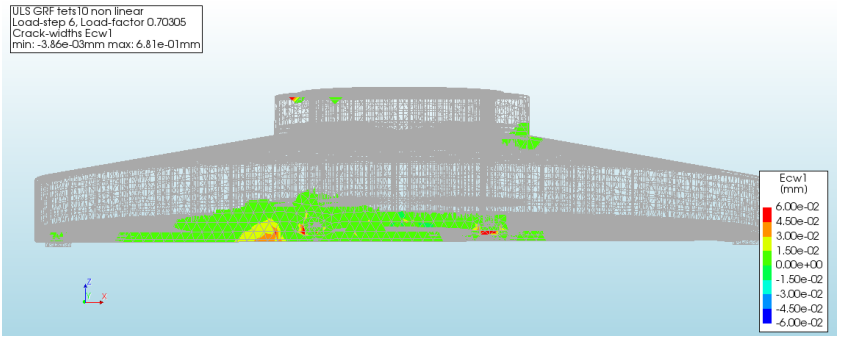

Figure 8.24: Crack width w_1 at the onset of the first significant cracks caused by moment loading (load factor 0.7031)

The crack widths in global x-direction, Figure 8.26, compared to the crack widths in the first principal direction to show that these correspond to each other. The crack distribution logically match the previously shown reinforcement strains.

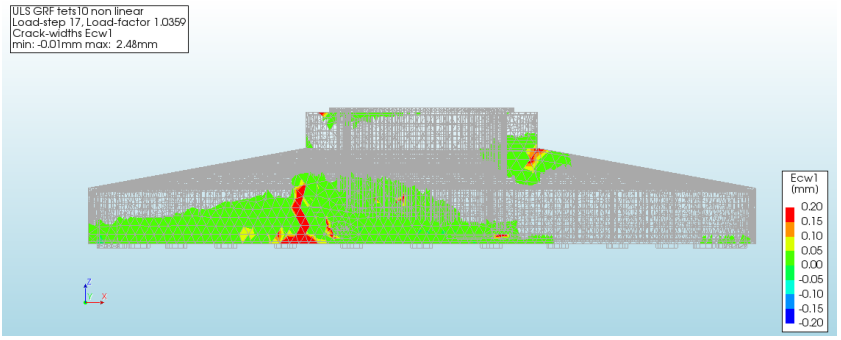

Figure 8.25: Side view of crack width w_1 at load step before failure (load factor 1.0359)

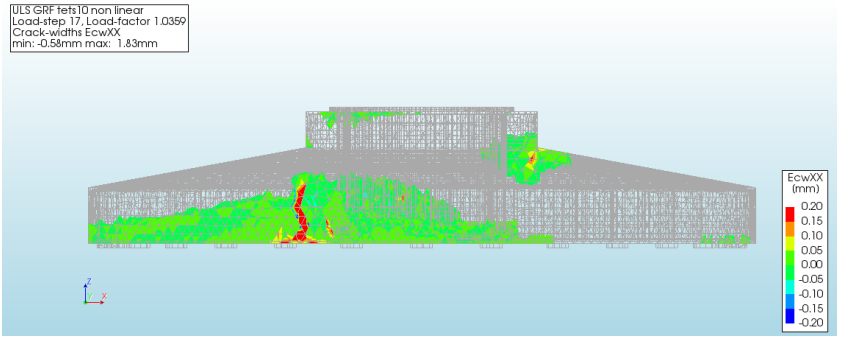

Figure 8.26: Side view of crack width w_{XX} at load step before failure (load factor 1.0359)

When Figure 8.27 is compared to Figure 8.28 this further illustrate the similarity of the 2 defined directions. In the top view of the structure, shown in Figure 8.29, cracking around the pedestal can be observed.

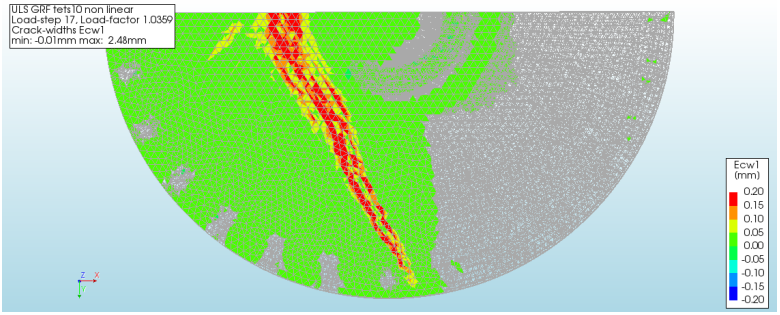

Figure 8.27: Bottom view of crack width w_1 at load step before failure (load factor 1.0359)

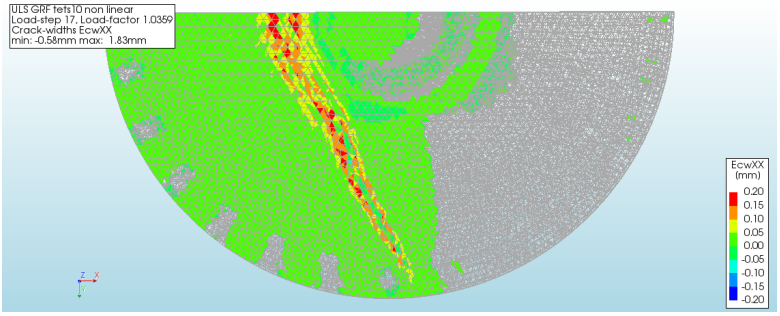

Figure 8.28: Bottom view of crack width w_{XX} at load step before failure (load factor 1.0359)

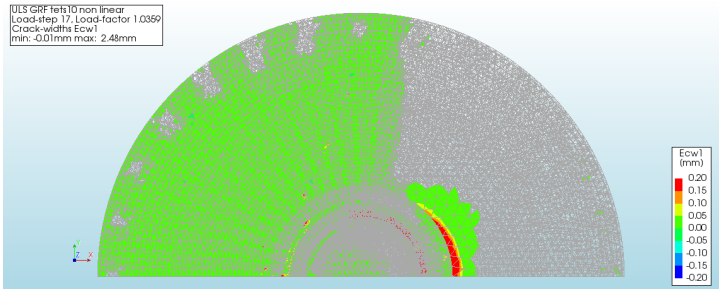

Figure 8.29: Bottom view of crack width w_1 at load step before failure (load factor 1.0359)

8.4.2. Crack progression

In Figure 8.30 the amount of cracks for every load step is shown. A steady increase can be observed for the total number of cracks while the number of active cracks drops at load step 8, corresponding to a load factor of 0.846, after which only a small increase is observed. This again suggests that after the onset of the first significant cracks the rest of the structure remains in tact and behaves more or less linearly.

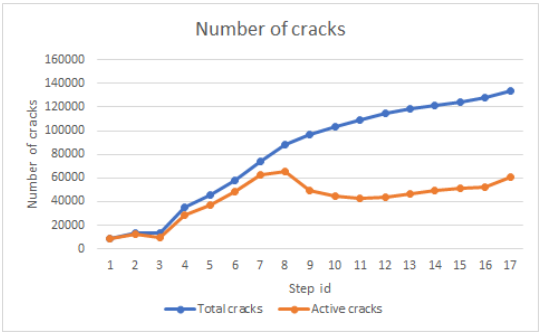

Figure 8.30: Number of cracks - load step diagram for all loading.

8.5. Pile loads

Although the foundation piles are incorporated in the model as to be able to behave multi-linearly, within the limits caused by the dominant failure mode this model they show almost only linear behaviour as shown in Figure 8.31. The initial analysis for the linear model showed that non-linear pile behaviour only becomes significant at a load factor of approximately 2.0, which is much higher than is expected to ever happen. Therefore no additional safety measures are applied for pile/soil behaviour at this moment.

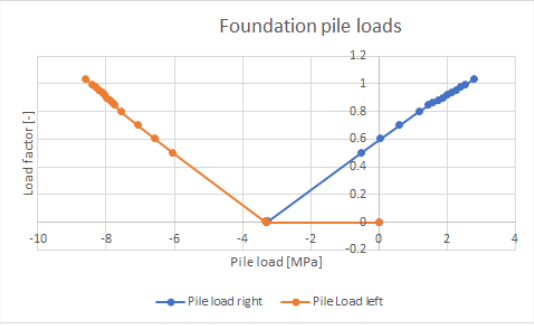

Figure 8.31: Load - pile stress diagram for all loading steps

9

Optimization of reinforcement design

This model was built to improve the understanding of the actual structural behaviour of a cylindrical foundation structure.This improved understanding can be used to improve and optimize the reinforcement design. The possibilities for optimization will be different for every project, but as the reference project was chosen to be representative this chapter will go over some improvements.

9.1. Reinforcement reduction

Although the overly high reinforcement ratio appears to lead to brittle failure, simply reducing it would not necessarily improve the load bearing capacity of the structure, although it can make the behaviour more elastic. This brittle failure behaviour makes it difficult to determine reinforcement reduction possibilities as it is only activated in a narrow band, calling on only a few types of reinforcement. As for now only minor strains are observed in the top radial and tangential bars which possibly provides the possibility for a slight reduction. The shear reinforcement is in general not subjected to high strains either, making a small reduction in amount of stirrups possible.

9.2. Effect of steel fibre reinforced concrete

The minor alterations in the constitutive model to represent the addition of steel fibres to the concrete resulted in interesting observations. The first one being that the load factor before failure had increased from 1.0359 to 1.3835 which is an increase of 33%. In Figure 9.1 it can be seen that for this case the reinforcement does yield, which can be an explanation for improved structural behaviour.

Figure 9.1 shows that, although it is slightly more prevalent, yielding still takes place at the same location, but this is as expected since this will always be the location with the highest strains in x-direction. In Figure 9.3 it can be seen that there is still a concrete compressive zone at the moment of failure.

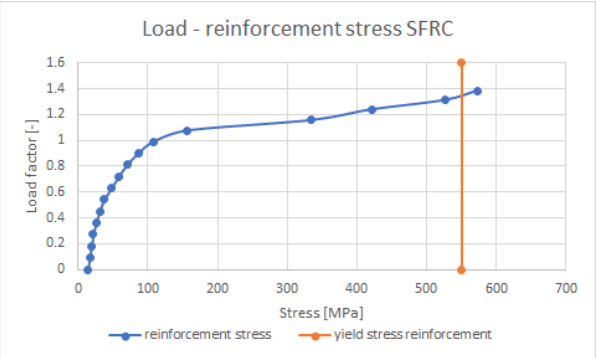

Figure 9.1: Load-stress diagram. $\sigma_{XX,reinf}$ at the bottom left of the structure where first concrete yielding is seen for an analysis with SFRC. Load factor corresponding to moment load introduction

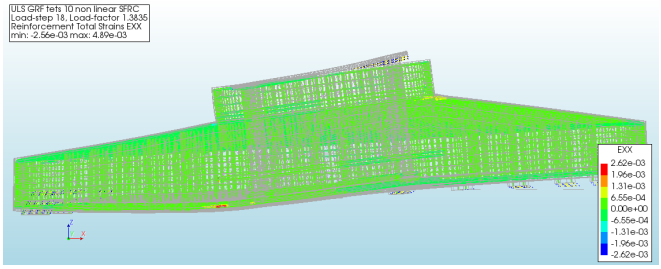

Figure 9.2: Side view of reinforcement strains $\epsilon_{XX,reinf}$ at load step before failure (load factor 1.3835) scaled to reinforcement yield strength for SFRC analysis

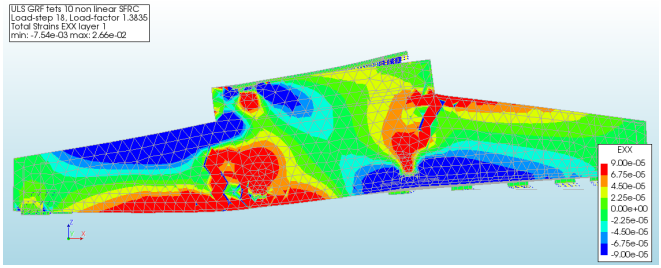

Figure 9.3: Side view of concrete strains ϵ_{XX} at load step before failure (load factor 1.3835) scaled symmetrically for SFRC analysis

In Figure 9.4 it can be clearly seen that the occurrence of reinforcement strains is limited closer to the centre cross section compared to Figure 8.16.

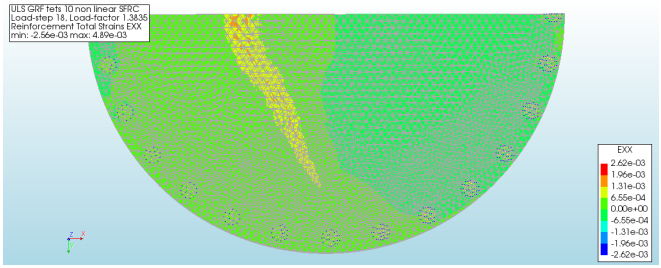

Figure 9.4: Side view of reinforcement strains $\epsilon_{XX,reinf}$ at load step before failure (load factor 1.3835) scaled to reinforcement yield strength for SFRC analysis

Apart from the onset of reinforcement yielding at the bottom of the structure horizontally, reinforcement bars placed vertically at the edge of the pedestal will yield as well. This type of failure can be compared to that in the underside of a bending beam or slab. But since there is already reinforcement present in vertical direction in this location this will propably not be a problem.

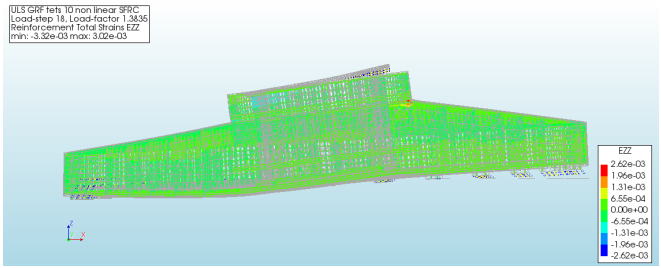

Figure 9.5: Side view of reinforcement strains $\epsilon_{ZZ,reinf}$ at load step before failure (load factor 1.3835) scaled to reinforcement yield strength for SFRC analysis

10

Conclusions & Recommendations

In this chapter conclusions are drawn based on the results of the analyses. Subsequently, the research questions are answered. Finally, recommendations for future model development will be given.

10.1. Conclusions

What considerations influence the development of a non-linear 3D model, improving on an existing linear 2D model, and what are their implications?
A 3D non-linear model of an onshore wind turbine foundation can be made incorporating multiple detailed components. These include the load introduction via a load spreading plate and an unbonded anchor cage, detailed modelling of the connection to the foundation piles and a complete 3D reinforcement reinforcement model.

2D and 3D linear results
When comparing the 2D and 3D linear analyses, the most notable differences can be attributed to the addition of the pedestal in the 3D model. This results in a locally increased stiffness in the structure. While this leads to increased maxima for stresses and distributed moments in the pedestal, the structure outside it is relieved. The differences look especially favourable for the m_{yy}. This distributed moment is directly related to the tangential reinforcement. Therefore, this difference suggests a possible reduction of tangential reinforcement.

Anchor cage
As the forces from the wind turbine are introduced via the unbonded, prestressed anchor bolts of the anchor cage, initially only compressive stresses are found in the centre of the structure. In the 2D model the load was applied to the centre cross section of the structure. However, as the modelling of the unbonded tendons requires non-linear interfaces, the introduction of the moment load was done with a combination of compressive and tensile stresses on the pedestal via the LSP, for the linear 3D model. In this aspect the 2D linear model more closely resembles reality than the 3D linear one. Before model failure, the compressive stresses in the centre of the structure exceed the compressive strength of concrete only in a small area under the top LSP, and above the bottom one. This causes some concrete crushing. The concrete structure should be able to absorb this local exceedance.

Constitutive model
For the non-linear analysis the size of the structure proved to be problematic, as the desired element size leads to an unmanageably large model with regard to the number of elements, and corresponding computational time. Smaller elements are desirable, as most concrete tensile constitutive models are element size dependent. As a solution for this the tensile stiffening principle was used. Tension-stiffening can be incorporated in the model through the use of concrete-reinforcement average strains. To do so stress-strain relations have to be entered manually. The simplest example of this is a linear post-cracking model based on the ultimate reinforcement strain. More complex alternatives are multi-linear ones based on experimental stress-strain relations. The progression of the cracks suggests that the applied concrete tensile model, based on steel-concrete average ultimate strain, functions as it should. However, the sudden failure makes it difficult to tell

whether it behaves fully correct. A model that should solve stability issues, the Allam model, does not increase the maximum load before analysis failure. It even slightly reduces the failure load factor. This is not entirely illogical, as the overall fracture energy is slightly reduced from the linear model. If non-convergence would not occur as soon as it does in the analysis, this would make the model slightly more conservative. This is especially applicable in the regions where there is no reinforcement, and the use of a steel-concrete average strength is not entirely justified.

Model failure
Convergence problems appear to occur when splitting cracks reach a critical value. Although this splitting is indeed likely to occur, and it is something to address carefully, it is not likely to cause abrupt failure of the structure. Possibly, the relatively abrupt way a linear stress-strain diagram becomes horizontal, contributes to the instability of the solution at analysis divergence.

Designing and modelling concrete structures is based on the premise that reinforcement mitigates the negative effects of high tensile strains and cracking in concrete. Therefore, the fact that there is little reinforcement in the centre of the structure, where the splitting happens, may contribute to the sudden instability of the model. This is illustrated by the fact that relatively high tensile stresses occur very locally in the outer tips of the splitting reinforcement. These local reinforcement tensile stresses lead to yielding at the moment the analysis stops. This can only happen because bonded reinforcement was applied. In reality, reinforcement would slip in such a situation.

Foundation piles
In a linear model it is sufficient to model the foundation piles with simple springs. Different details of the soil structure interaction can be included, such as pile inclination. Multiple different pile models were studied, but the difference in results were minor for a structure of this size. As stress concentrations can occur when single noded springs are used, which may be problematic in a non-linear analysis, the use of circular interfaces is preferred. As it is additionally complex to implement inclination for such interfaces and the effects were found to be minor pile inclination was omitted in the final non-linear model. The horizontal soil resistance was still included in the non-linear model, resulting in a more realistic model compared to the 2D linear one where the piles were fixed horizontally. While non-linearity is also included for the piles, taking into account the load-displacement behaviour as determined in geotechnical research of the building site, the piles will generally not exceed the limits wherein they still behave linearly.

Is it possible to obtain a better understanding of the distribution of stresses and strains in a wind turbine foundation using a 3D non-linear model compared to a linear 2D one, and does this lead to more detailed insight into the possible failure modes?
While this model is showing significance for obtaining more detailed insights of the structural behaviour of the structure, it is unable to determine an ultimate load resistance as numerical or computational issues occur, leading to analysis non-convergence, before the actual expected structural failure.

Stresses and strains
The model clearly shows the distribution of concrete stresses and strains in all directions, global and principal. It provides a better understanding of the effects of the redistribution of stresses compared to the linear 2D model. The redistribution leads to relatively high strains at the tension zone in the bottom compared to the tension zone in the top. The initial reinforcement stresses and strains throughout the entire structure can be seen, and the onset of reinforcement yielding can also be observed. In the 2D model, only linear strains were obtainable, and exclusively at predefined heights in the structure. Additionally the vertical reinforcement strains are calculated. The 2D model was entirely unable to calculate these, and a linear model can only provide an estimate with limited accuracy, based on the overall distributed shear forces in the cross section at mid-height.

Compared to the 2D model the horizontal reinforcement strains in the top of the structure are lower than expected. Actual reinforcement yielding only occurs in the radial and orthogonal reinforcement at the bottom of the structure along the x-axis in the central cross section, and at the ends of the splitting reinforcement at the maximum load step reached in this analysis.

No stresses close to yield strength occur in the top radial reinforcement bars at the moment of failure, suggesting possibility of reduction. However because the actual ultimate loading is not reached this can't be said without a doubt. There is also only little tension in the tangential reinforcement in both the bottom

and the top. Again, suggesting the possibility of a reduction of the amount of reinforcement. At the last step of the analysis the third principal stress exceeds compressive strength of concrete at the compressive side of the LSP's and in the structure just outside of the pedestal. Steel compressive yield stresses in z-direction are reached in the uppermost part of the vertical reinforcement under the LSP as well. This suggests that compression failure may occur in the pedestal if loading is increased to the desired value.

Splitting crack
Slightly below mid height in the main structure left from the pedestal a splitting crack, with an order of magnitude of millimetres, can be observed. It must be noted that the crack does not continue all the way to the bottom of the foundation. Additionally on the upper surface of the structure at the opposite side of the pedestal substantial crack spacings are present. The fact that splitting occurs in the structure is something that can be expected, but cannot actually be calculated using a 2D linear model. Currently splitting reinforcement is designed based on experience. Because splitting cracks are calculated in the non-linear model a more accurate estimation can be made of the required amount of splitting reinforcement and where it must be applied. As the load factor for which model failure occurred was increased by adding additional splitting reinforcement, this could be seen as a way of increasing structural capacity as well, if the model failure is not only due to convergence problems. With this increased capacity it may be possible to reduce the reinforcement in other locations in the structure without significantly compromising the moment resistance.

Structural failure
Besides the occurrence of splitting cracks being the likely cause of non-convergence, potential structural failure modes like plastic bending failure, pulling out of the anchor cage, brittle failure in the compression zone, or failure in tension of the pedestal edge were also identified. This shows that this model is capable of failure analysis and is a potential basis for further development of a non-linear model capable of determining the ultimate structural load resistance.

The convergence issues that occur before the expected moment of failure for the reference project, make it difficult to estimate whether significant reductions can be made to the amount of applied reinforcement. When the highest loading is reached the reinforcement stresses throughout the structure are still low, with some higher stresses observed locally. If the load would be increased these local stress concentrations might increase to significant yielding sections, but this can't be stated definitively. It is also impossible to be certain that stress concentrations will appear elsewhere with increased loading. However the model does provide information about the stress distribution which may enable more optimized design for other future projects. For example the concrete strains at the tensile zone in the top of the main structure are lower than would be expected from the linear analysis. As far as alterations of other design parameters go such as height or diameter of the construction can not solely be based on this model. The diameter, for example, is primarily determined by the soil properties, pile capacity and the necessary radius required to ensure moment resistance.

Serviceability limit state
Since a load factor of higher than 1 can be achieved for analysis in te serviceability limit state, estimations can be made about where reinforcement could be shed based on the criterion that only limited steel yielding may occur. When looking at the SLS it can be safely stated that the rotation of the tower base will stay well within the defined limits. And while yielding of the reinforcement is very limited, the crack widths may pose a problem at higher loading, although their limit is based on environmental influences which are less important when the cracking occurs internally.

As it is difficult to apply additional reinforcement, the use of SFRC is an attractive option. SFRC can increase the capacity with regard of the compressive resistance in the bottom of the foundation without the addition of complex bar reinforcement. It is clear that application of SFRC increases the load bearing capacity of the structure as a whole and this leads to other potential fail modes becoming apparent.

10.2. Recommendations

Based on the conclusions and other observations, some recommendations for further development or use of this model can be made.

To further validate this model it is advisable to run it for several projects to build up a database of failure modes and to study the results and determine whether they follow expectations based on engineering judgement. Furthermore, the model is initially set up to be parametrized. Yet, it will require validation from other projects to determine its functionality as such.

Reducing the element size will increase the computational time, which is already significant. But it is advisable to validate the tension stiffening principle for this specific structure by using a more complex constitutive concrete tensile model, like Hordijk post-cracking behaviour or even the full Eurocode concrete material model, which would require a reduced default element size. The effects of a slight increase, and decrease in default element size was checked. These effects appeared not to be significant. However a full element dependency study may be performed to determine whether reducing the element size improves the model stability.

Further research can also be done into other concrete material properties. Perhaps specifying residual tensile strength or the application of a more detailed shear reduction model will improve stability. Furthermore, a relatively simple model for the reinforcement was used. Bond-slip reinforcement should result in more realistic results.

The results showed no increased stability for a multi-linear tensile model. Such a model even lowered the maximum load factor before convergence problems occurred. However the slightly more reduced crack pattern seems realistic, and if the is improved, such a model may lead to an improvement to the quality of the results.

In this study the benefit of SFRC was only checked by modifying specific parameters of the concrete. A more detailed constitutive model of SFRC can be used to include more residual strength or more elastic behaviour for instance. Furthermore, SFRC can also be applied locally, as failure is most likely to occur in the bottom of the structure. As the analysis, and more importantly the alterations in material model, for SFRC were only superficial it is not possible to guarantee the observed improvements directly without further research. To further reduce the carbon footprint alternative reinforcement fibre materials can be studied. Recycling plastic waste or synthetic fibres may prove to be a good option.

Bibliography

[1] Eurocode 2: Design of concrete structures - part 1-1 : General rules and rules for buildings, 1992.

[2] fib model code for concrete structures 2010, 2010.

[3] A. A. Abbas, M. I. Khan, and S. Mourad. Evaluation of mechanical properties of steel fiber reinforced concretewith different strengths of concrete. *Construction and Building Materials*, 168, 2018.

[4] S. M. Allam, M. S. Shoukry, G. E. Rashad, and A. S. Hassan. Evaluation of tension-stiffening effect on the crack width calculation of flexural rc members. *Alexandria Engineering Journal*, 2013.

[5] J. A. O. Barros and J. Sena Cruz. Fracture energy of steel fiber-reinforced concrete. *Mechanics of Composite Materials and Structures*, January 2001.

[6] Y. Cao, Q. Yu, and H. J. H. Brouwers. Numerical investigation of fibers effects in sfrc under dynamic tension. *The 9th International Symposium on Cement and Concrete (ISCC 2017)*, 2017.

[7] *Diana 10.2 Users manual*. DIANA FEA BV, 2017.

[8] M. A. N. Hendriks, A. Boer, and B. Belletti. Guidelines for nonlinear finite element analysis of concrete structures. Rijkswaterstaat Technical Document RTD 1016-1:2016, Rijkswaterstaat, June 2017.

[9] D. A. Hordijk. *Local approach to fatigue of concrete*. PhD thesis, TU Delft, 1991.

[10] A. G. Kooiman. *Modelling Steel Fibre Reinforced Concrete for Structural Design*. PhD thesis, TU Delft, 2000.

[11] B. Massicotte, A. E. Elwi, and J. G. MacGregor. Tension-stiffening model for planar reinforced concrete members. *Journal of Structural Engineering*, 1990.

[12] A. Sokolov. *Tension stiffening model for reinforced concrete beams*. PhD thesis, Vilnius Gedimnas TU, 2010.

[13] P. S. Song and S. Hwang. Mechanical properties of high-strength steel fiber-reinforced concrete. *Construction and Building Materials*, 18, 2004.